

A STUDY ON A HIGH PRECISION MAGNETIC LEVITATION TRANSPORT
SYSTEM FOR CARRYING ORGANIC LIGHT-EMITTING DIODE DISPLAYS

A Dissertation

Submitted to the Faculty

of

Purdue University

by

Jaeyoung Kim

In Partial Fulfillment of the

Requirements for the Degree

of

Doctor of Philosophy

May 2019

Purdue University

West Lafayette, Indiana

THE PURDUE UNIVERSITY GRADUATE SCHOOL
STATEMENT OF DISSERTATION APPROVAL

Dr. Galen B. King, Chair

School of Mechanical Engineering

Dr. David J. Cappelleri

School of Mechanical Engineering

Dr. Peter H. Meckl

School of Mechanical Engineering

Dr. Stanislaw H. Zak

School of Electrical and Computer Engineering

Approved by:

Dr. Jay P. Gore

Head of the Departmental Graduate Program

To my parents, *Hyunsup Kim and Jinbum Shin*
Thank you for your endless support, love and care.
I would not have made it without you.

ACKNOWLEDGMENTS

I would like to give my sincere respect and deepest gratitude to my academic advisor, Professor Galen B. King for his full support, guidance, understanding, and encouragement throughout the research. His academic knowledge and kindness have always led me in the right direction of the works, and I have learned how to approach and solve problems in more logical ways. Moreover, I genuinely appreciate his detailed feedback for writing academic articles that could be a successful conclusion. I also would like to thank Professor David J. Cappelleri, Professor Peter H. Meckl, and Professor Stanislaw H. Zak for serving my academic committee and providing invaluable suggestions throughout the current and future directions of research. In addition to the faculty members, my gratitude goes to all the members of the Department of AI Machinery at Korea Institute of Machinery and Materials (KIMM). Especially Dr. Hyung-Suk Han for giving me an excellent opportunity to collaborate with a project entitled by a high precision magnetic levitation transport system. Dr. Chang-Hyun Kim and Dr. Chang-Wan Ha who have always offered their time for technical discussions, highly valued suggestions, and encouragements throughout researches. It was also fascinated to have the opportunity to work the majority of my researches in their facilities. I would like to give my special thanks to all my family members, my father Hyunsup Kim, my mother Jinbum Shin, my brother Jaeho Kim and my sister Hyunji Kim for their support and encouragement that help me to motivate and focus from the beginning of study in the U.S.

This work was supported by the National Research Council of Science & Technology within the project entitled “Development of Decentralized Levitation Control Technologies for Improved Reliability and Economic Feasibility”.

TABLE OF CONTENTS

	Page
LIST OF TABLES	vii
LIST OF FIGURES	viii
ABBREVIATIONS	xiii
ABSTRACT	xiv
1. INTRODUCTION	1
1.1 Motivations and Objectives	1
1.2 Literature Review	4
1.2.1 Magnetic Levitation Train	4
1.2.2 Magnetic Levitation Transport System	8
1.3 Dissertation Outline	11
1.4 List of Publications	11
2. SYSTEM DESIGN	12
2.1 Magnetic Levitation Transport System	12
2.2 Levitation Controller Design	15
2.2.1 Levitation Force and Voltage Equation	16
2.2.2 Dynamic Equation of Heave Motion	17
2.2.3 Current Controller Design	19
2.2.4 Airgap Controller Design	22
2.2.5 Levitation Controller Verification	23
3. SENSOR OFFSET ESTIMATION	29
3.1 Sensor Characterization	29
3.2 Measurement Error	33
3.3 Analysis of truncated temporal measurement	34
3.4 Fast Fourier Transform Analysis	36
3.5 Correlation Between Amplitude and Sensor Offset	38
3.6 Estimation of Parameters in Linear Equation Using Iteration Method	40
3.7 Simulation Results	43
4. ROLL AND PITCH CONTROLLERS DESIGN	48
4.1 Dynamic Equation of Roll Motion	48
4.2 Dynamic Equation of Pitch Motion	49
4.3 State Space Representation of Linear Time Invariant System	51
4.4 Optimal State-Feedback Controller-Observer Compensator	53

	Page
4.5 Simulation Results	56
4.5.1 Test 1: Ideal Case	58
4.5.2 Test 2: Existence of Sensor Installation Error	61
4.5.3 Test 3: Existence of Sensor Installation Error and External Load Disturbance	65
5. SECTION CONTROL ALGORITHM	70
6. EXPERIMENTAL VERIFICATION	73
6.1 Experimental Setup	73
6.2 Experimental Results	75
6.2.1 Levitation Control Performance at a Standstill	75
6.2.2 Levitation Control Performance at Low Speed Level	78
6.2.3 Levitation Control Performance at High Speed Level	81
6.2.4 Levitation Control Performance in the Deadzone	84
7. SUMMARY AND FUTURE DIRECTION	93
7.1 Summary and Conclusion	93
7.2 Future Work	95
REFERENCES	96
A. LINEARIZED EQUATION OF THE LEVITATION FORCE BY EACH LEVITATION ELECTROMAGNET	99
B. DERIVATION OF THE PITCHING MOTION OF THE CARRIER WITH AIRGAP APPROXIMATION	102
VITA	104
LIST OF PUBLICATIONS	105

LIST OF TABLES

Table	Page
3.1 Specifications of PU-05 and AEC-76. The measuring range of gap sensor (Iron) is from 0 - 2 mm and its output voltage is ± 5 V. The resolution of gap sensor has $0.5 \mu\text{m}$ - $0.8 \mu\text{m}$ and both gap sensor and converter can operate at room temperature. The sampling frequency of the converter is 20 kHz so that the data can be acquired with 0.00005 seconds of the sampling interval.	32
3.2 The results of the iteration method for the gap sensor at the right side. The first and the last alignment of gap sensors has no sensor offset. Throughout the iteration method, the maximum error is around $1.2976 \mu\text{m}$, which is less than the tolerance.	44
3.3 The results of the iteration method for the gap sensor at the left side. The first and the last alignment of gap sensors has no sensor offset. Throughout the iteration method, the maximum error is around $1.4663 \mu\text{m}$, which is less than the tolerance.	45
4.1 The results for pitch angle in Test 1 . The maximum and minimum attenuation of pitch angles are $0.7 * 10^{-3}$ deg and $0.61 * 10^{-3}$ deg, respectively.	59
4.2 The results for roll and pitch angle in Test 2 . The maximum and minimum attenuation of the roll angles are $18.2 * 10^{-3}$ deg and $13.8 * 10^{-3}$ deg, respectively. The maximum and minimum attenuation of the pitch angles are $10.3 * 10^{-3}$ deg and $30.1 * 10^{-3}$ deg, respectively.	62
4.3 The results for roll and pitch angle in Test 3 . The maximum and minimum attenuation of the roll angles are $1.9 * 10^{-3}$ deg and $10.9 * 10^{-3}$ deg, respectively. The maximum and minimum attenuation of the pitch angles are $20.2 * 10^{-3}$ deg and $0.033 * 10^{-3}$ deg, respectively.	66
6.1 The maximum peak to peak variation of the airgap measurements.	81

LIST OF FIGURES

Figure	Page
1.1 One of the manufacturing processes of OLED displays: evaporation process. Having an evaporation heating sources, the organic compounds are deposited on the glass-boards in the vacuum chamber. To avoid the dust, particles, and internal heat sources in this process, transport system using magnetic levitation technology should be developed to produce sensitive displays for high productivity and low defect rate.	2
1.2 Magnetic levitation train (Transrapid 09) by Germany [16].	6
1.3 Urban magnetic levitation train (Ecobee) and SUMA 550 by South Korea [4].	7
1.4 Magnetic levitation conveyor system for carrying LCD glass [22].	8
1.5 First generation of a passive magnetic levitation transport system [24]. . .	9
1.6 Second generation of a passive magnetic levitation transport system [26]. .	10
2.1 High precision magnetic levitation transport system. Major components (levitation electromagnets, gap sensors, linear motor, linear encoder and, etc) of system are not located in the moving platform so that it can reduce the load weight and the mechanical thermal expansion.	13
2.2 The major components of a high precision magnetic levitation transport system: the levitation electromagnets, propulsion linear motor, linear encoder, guidance electromagnets and gap sensors.	14
2.3 A configuration of the magnetic levitation transport system. The direction of levitation force exerted by each levitation electromagnets is up, and that of airgap is down. The carrier has six degrees of freedom.	16
2.4 Configuration of the carrier's heave motion at center of mass. The direction of levitation force at the right and left side are up and the direction of airgap at the right and left side is down. The direction of both gravitational force and a load disturbance force is down. The heave at CoM is expressed from the relationship between each airgap.	18
2.5 The tracking performance utilizing designed current controller at 300Hz. The blue line represents the reference current signal and the red line represents the applied current signal with the optimal control gains of the current controller, respectively.	21

Figure	Page	
2.6	The control strategy diagram for the entire levitation feedback loop. The red and blue dash lines are the current control loop and the airgap control loop, respectively. To reduce a mechanical resonance and a noise from gap sensors, a second order notch filter, and a first order low pass filter are designed. The section control algorithms are shown in section 5.	24
2.7	Frequency response of $G_L^c(s)$ and $G_{CL}^c(s)$. $G_L^c(s)$ is the closed-loop transfer function of airgap feedback loop ($\Delta\dot{c}_k \approx 0$) and $G_{CL}^c(s)$ is the closed-loop transfer function of the entire levitation feedback loop ($\Delta\dot{c}_k \neq 0$). The response of these two closed-loop transfer function are similar at low frequencies (less than 30 Hz).	25
2.8	The bode plot of the open-loop transfer function of the overall levitation system, $G_{CL}^o(s)$	26
2.9	The magnitude of the frequency response by impact test.	27
3.1	A simplified schematic structure of gap sensor.	29
3.2	Output characteristics of gap sensor. Since the carrier is covered by iron, accurate measurement can be obtained 1 mm of the desired gap.	30
3.3	Gap sensor (PU-05) and Converter (AEC-76). The unit of dimension is mm.	31
3.4	Schematic view of the sensor installation error. As the carrier is levitated from the railroad, the desired gap between the carrier and the gap sensor (S_n) is 1 mm. Due to sensor installation error, the carrier motion can fluctuate as it moves along the propulsion axis.	33
3.5	The raw measurement at 500 mm/s speed from the gap sensor. The levitating condition is from 0 to 0.4 sec where the carrier levitates at the desired gap. The moving condition is from 0.4 to 3 sec where the carrier moves. The gap sensors are deactivated, and the carrier moves to the next allocation after 3 sec.	35
3.6	The single-sided amplitude spectrum of truncation measurement with sensor offset. The peak occurs due to the fluctuation of the carrier, and other high frequencies are the measurement noise and levitation accuracy.	36
3.7	Homogeneity of the Fourier transform. The amplitude modulation is changed in the time domain as it produces an identical change in the frequency domain [34].	37

Figure	Page
3.8 The fitted curves for each condition: (a) condition 1: a random variable of one sensor offset and zeros of other sensor offsets. (b) condition 2: a random variable of one sensor offset and the minimum value of other sensor offsets. (c) condition 3: a random variable of one sensor offset and the maximum value of other sensor offsets. (d) condition 4: random variable of one sensor offset and static-arbitrary values of other sensor offsets.	39
3.9 The process diagram based on the iteration method. This process is to converge to the tolerance ($10\text{ }\mu\text{m}$) based on updating the parameters in the linear equation.	42
3.10 Measurements of all gap sensors before calibrating sensor offset.	47
3.11 Measurements of all gap sensors after calibrating sensor offset.	47
4.1 The configuration of the carrier's roll motion. The difference between the sum of the levitation forces with a small perturbation generates the roll motion of the carrier along the propulsion axis.	49
4.2 The configuration of the carrier's pitch motion. The carrier has a stable pose at the first stage. As the carrier moves to the next influential zone of the levitation electromagnet at the second stage, fluctuations inevitably occur. The carrier has a stable pose again as the moment of levitation forces at each side is balanced.	50
4.3 The control block diagram for roll and pitch feedback loop. Having a state space representation of roll and pitch motion, the outputs are obtained. The observer gain (L) helps to estimate the state variables and to approach the actual state variables. The optimal controller gain (K_o) helps to minimize undesired deviations of the roll and pitch motion.	55
4.4 Desire velocity profile of the magnetic levitation transport system. The slope indicates 500 mm/s velocity of the system.	57
4.5 Roll and pitch motion trajectories in Test 1 . The red line represents the roll and pitch angle with the levitation, roll and pitch controllers. The blue line represents the roll and pitch angle with the levitation controller only.	58
4.6 Airgap measurement from each sensor in Test 1 : (a) airgap measurement with K1 and (b) airgap measurement with K2 . There are 13 switching patterns between each gap sensor during the entire process.	59
4.7 Zoom-in view of airgap measurement in Test 1 : (a) airgap measurement with K1 and (b) airgap measurement with K2 . The fluctuations of the airgap measurement is a slightly attenuated with K2 around 2.2 seconds and 2.6 seconds.	60

Figure	Page
4.8 Roll and pitch motion trajectories in Test 2 . The red line is the roll and pitch angle with the levitation, roll and pitch controller and the blue line is the roll and pitch angle with the levitation controller only.	61
4.9 Airgap measurement from each sensor in Test 2 : (a) airgap measurement with K1 and (b) airgap measurement with K2	63
4.10 Zoom-in view of airgap measurement in Test 2 : (a) airgap measurement with K1 and (b) airgap measurement with K2	64
4.11 Roll and pitch motion trajectories from 2 to 3 sec in Test 3 . The red line indicates the roll and pitch angle with the levitation, roll and pitch controllers. The blue line indicates the roll and pitch angle with the levitation controller only.	65
4.12 Airgap measurement of each sensor from 2 to 3 sec in Test 3 : (a) airgap measurement with K1 and (b) airgap measurement with K2 . There are around 14 fluctuations of the airgap measurement with K1 that occur from 2.2 to 2.7 sec and these fluctuations are significantly attenuated with K2	67
4.13 The current signals with K2 in Test 3 . The initial current signal is around 5 A to levitate the carrier. Around 2 A of the current signals are used to stabilize the levitation control performance under sensor installation error. From 2 to 3 sec, around 3 A of the current signals are used to stabilize the levitation state under sensor installation error and external load disturbance.	68
5.1 Schematic diagram of the section control algorithm based on the position of the carrier.	71
5.2 Simulation result of sum of the levitation forces and sum of the moment using section control algorithms.	72
6.1 An experimental setup for a high precision magnetic levitation transport system.	74
6.2 Levitation control performance at a standstill before levitating the carrier (right) and after levitating the carrier (left).	76
6.3 (a) Total current flows into the levitation electromagnet at a standstill and (b) Airgap measurement at a standstill.	77
6.4 The levitation control performance using the levitation controller only at moving speed of 30 mm/s: (a) Position of the carrier in the propulsion axis and (b) Zoom-in plot of airgap measurement.	79

Figure	Page
6.5 The levitation control performance using the proposed control strategies at moving speed of 30 mm/s: (a) Position of the carrier in the propulsion axis and (b) Zoom-in plot of airgap measurement.	80
6.6 The levitation control performance using the levitation controller only at moving speed of 300 mm/s: (a) Position of the carrier in the propulsion axis and (b) Zoom-in plot of airgap measurement.	82
6.7 The levitation control performance using the proposed control strategies at moving speed of 300 mm/s: (a) Position of the carrier in the propulsion axis and (b) Zoom-in plot of airgap measurement.	83
6.8 Schematic view of the deadzone. Each module can be extended in series and, there is a later gap where the levitation electromagnets are disabled to install owing to the screen door. The range of the deadzone is about 1/3 of the length of the carrier.	84
6.9 Experimental environment setup for the deadzone. To achieve the similar environment of the deadzone, the two pairs of side levitation electromagnets are disconnected, and the carrier passes into this zone supported by the 10-levitation electromagnets only.	85
6.10 Experimental results using the PID controller only: (a) Position of the carrier at 30 mm/s of speed level. (b) The airgap measurement utilizing the conventional PID levitation controller only in the deadzone at 30 mm/s of speed level. The switching zones represent that the carrier moves to the next influential zone. The carrier moves to the first and following switching zones under the desired airgap. As it goes to the deadzone, the carrier fluctuates and attaches to the levitation electromagnets on attach point.	87
6.11 Experimental results using the proposed control strategies: (a) Position of the carrier at 30 mm/s of speed level. (b) Airgap measurement utilizing the proposed control strategies in the deadzone at 30 mm/s of speed level.	89
6.12 (a) Zoom in plot of the roll angle of the carrier in the deadzone at 30 mm/s of speed level. (b) Zoom in plot of the pitch angle of the carrier in the deadzone at 30 mm/s of speed level.	90
6.13 Zoom in view of the pitching moment in the deadzone.	91
6.14 Zoom in plot of the bias currents in the deadzone. The bias currents initially maintain about 0.8 A and 1.4 A based on the section control algorithms and these are increased to about 2 A owing to the absence of the levitation electromagnets in the deadzone.	92

ABBREVIATIONS

Maglev	Magnetic Levitation
OLED	Organic Light Emitting Diode
LCD	Liquid Crystal Displays
LED	Light Emitting Diode
FFT	Fast Fourier Transform
DFT	Discrete Fourier Transform
PM	Permanent Magnets
EM	Electromagnets
LQR	Linear Quadratic Regulator
PDA	Proportional Differential Acceleration
PI	Proportional Integral
PD	Proportional Derivative
PID	Proportional Integral Derivative
CoM	Center of Mass
SCM	Superconducting Magnet
EDS	Electrodynamic Suspension
LSM	Linear Synchronous Motor
LIM	Linear Induction Motor
RTI	Real Time Interface

ABSTRACT

Kim, Jaeyoung PhD, Purdue University, May 2019. A Study on a High Precision Magnetic Levitation Transport System for Carrying Organic Light-Emitting Diode Displays. Major Professor: Galen B. King, School of Mechanical Engineering.

High precision magnetic levitation control methodologies during the manufacture of Organic light-emitting diode (OLED) displays are designed, manipulated, and experimentally validated in this thesis. OLED displays have many advantages over conventional display technologies including thinner, lighter, lower power consumption, higher resolutions, and greater brightness. However, OLED displays require tighter environmental conditions of the manufacturing processes without the introduction of vibration and contamination. For this reason, magnetic levitation is used to transport the displays attached on the carrier during the manufacturing process. This thesis addresses several critical problems related to implement the levitation control performance of the carrier's motion during the manufacturing process.

Attractive magnetic levitation requires measurement of the airgap between the carrier and the levitation electromagnets. An algorithm for modeling the gap sensor installation errors was developed and subsequently used for controller development. A levitation controller only was initiated as the stationary point for optimal state feedback controller-observer compensator developed in this study. This optimal state feedback controller-observer compensator allows the carrier to be passed from support fixtures without the introduction of vibration. This controller was designed, and its levitation control performance confirmed with both simulation and experimental validation. To implement the levitation control performance of the carrier's motion, a second order notch filter and a first order low pass filter are designed to minimize the mechanical resonance and noise from the gap sensor, respectively. To reduce the sudden change of the levitation forces owing to the discrete allocation of the levitation

electromagnets, a section control algorithm is developed; the sum of the levitation forces is equal to the weight of the carrier and the sum of the moment along the propulsion axis is equal to zero.

Using the developed control strategies, the peak to peak variation of the carriers motion at a standstill was $50\ \mu\text{m}$. This same motion at low-speed $30\ \text{mm/s}$ was $250\ \mu\text{m}$. While at high speed $300\ \text{mm/s}$ was $430\ \mu\text{m}$. The relative improvement in the levitation control performance of optimal state feedback controller-observer compensator over the levitation controller only was a peak to peak attenuation of $50\ \mu\text{m}$ at low-speed and $270\ \mu\text{m}$ at high-speed. Most significantly while using optimal state feedback controller-observer compensator could be passed from support fixture to support fixture, i.e., through the deadzone, without mechanical contact or other manufacturing processes, inhibiting vibration.

Having comparative simulation and experimental validation, the proposed control strategies were validated to improve the levitation control performance of the carrier under uncertain disturbance and sensor installation error, and it is expected to manufacture OLED displays with high productivity and low defect rate.

1. INTRODUCTION

1.1 Motivations and Objectives

Magnetic levitation (Maglev) has been proposed as an innovative transport technology that is finding wide acceptance in many varied applications including, although not limited to, maglev trains, magnetic bearings, magnetic elevators, and magnetic suspensions, etc. [1 - 4]. Magnetic levitation systems are capable of rapid motion and the elimination or reduction of vibration owing to the virtual elimination of friction. This emerging technology has found application in the precision transport of displays during the manufacturing processes. Recently, a high precision magnetic levitation transport system has been developed in the process of manufacturing organic light-emitting diode (OLED) displays [5]. OLED displays have been introduced as a next-generation display technology for high-resolution consumer products. It has advantages over Liquid Crystal Displays (LCD) and Light Emitting Diode (LED) displays which include that it is thinner, lighter, brighter and lower power consumption. In spite of these advantages, it is difficult to manufacture using the existing wheel-based conveyor systems. This is because OLED displays being an organic thin film is sensitive to the manufacturing environment, and must be protected from excessive heat, vibration, dust, and exposed to air. Therefore, it is necessary to develop a transport system which can carry the displays without the introduction of vibration and contamination of the manufacturing environment as shown in Figure 1.1. To satisfy these specifications, a high precision magnetic levitation transport system is proposed for the transport of OLED displays during the manufacturing process. This maglev system is capable of moving along the constrained path (railroad) without any electrical components in the vacuum chamber, and this is a new paradigm of the transport of these sensitive material-based displays. In this system, the carrier

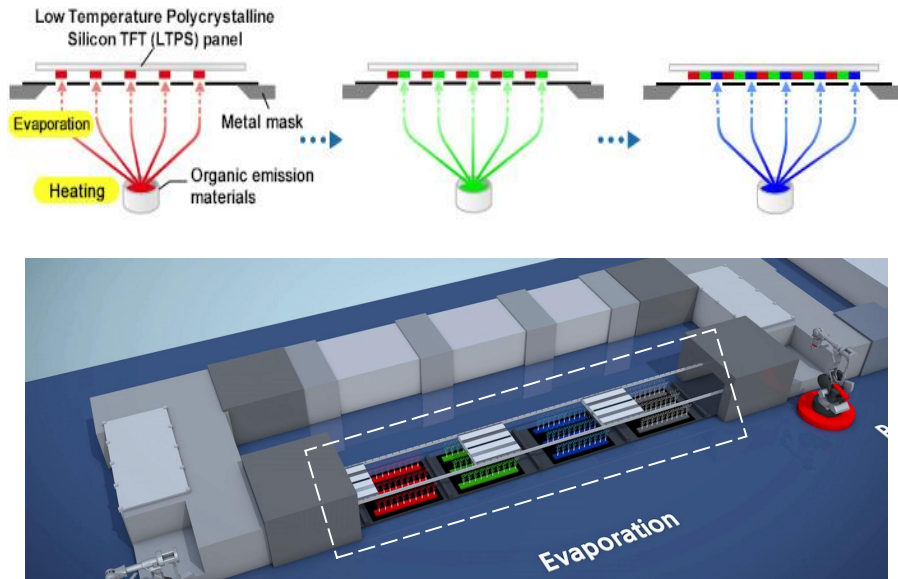


Figure 1.1. One of the manufacturing processes of OLED displays: evaporation process. Having an evaporation heating sources, the organic compounds are deposited on the glass-boards in the vacuum chamber. To avoid the dust, particles, and internal heat sources in this process, transport system using magnetic levitation technology should be developed to produce sensitive displays for high productivity and low defect rate.

is required to have a precise motion on the transport of OLED displays so that the system must guarantee levitation control performance for both robustness and stability. Therefore, several issues must be addressed to implement the levitation control performance as the carrier moves along the propulsion axis in this magnetic levitation system. The objectives of our research with this application are as follows:

- 1) Development of an algorithm to estimate airgap sensor offset.
- 2) Modeling and designing levitation, roll and pitch controllers.
- 3) Development of section control algorithms which is to minimize the sudden change of levitation forces as the carrier moves next to the influential zone of the levitation electromagnets.

- 4) Experimental verification of various scenarios such as a standstill, low-speed level, high-speed level, and deadzone environment.

1) In the magnetic levitation transport system, 20 gap-sensors are installed on the right and left sides to measure the vertical displacement of the carrier. Due to inevitable sensor installation errors, a fluctuated pitching motion of the carrier occurs at high speed, and this has a negative effect on the transport of OLED displays. Therefore, we have developed an algorithm to estimate this installation error and calibrate for the sensor offset using measurements from gap sensors. In our research, we collect raw measurement from gap sensors and truncated irrelevant measurements to cut off fluctuated pitching motion periods. Using Fast Fourier Transform (FFT) analysis and its properties, we then analyze the single-sided amplitude spectrum of the fluctuated pitching motion periods and found the correlation between its amplitude and sensor offset. Based on this correlation, we establish an initial linear equation between amplitude and sensor offset. Then, using an iterative method, we estimated the accurate parameters in a linear equation and obtained the sensor offsets. We then modeled the entire magnetic levitation transport system including levitation controllers and algorithmic procedure using MATLAB/Simulink to verify the levitation performance by applying random variables of sensor offset. After the levitation performance was verified, measurements of the calibrated sensor offset were compared to measurements with sensor offset.

2) The magnetic levitation system has been analyzed as a single-mass system in which only the vertical (heave) motion of the carrier was considered in the design of the levitation controller in previous research [5]. Because of external load disturbance and sensor installation errors, rotational movements of the carrier can occur and affect the levitation stability of the magnetic levitation transport system. The magnetic levitation transport is a six-degree of freedom system (DOF) but, the guidance electromagnets constrain the lateral movement and yaw motion of the carrier. Additionally, the translation movement in the propulsion axis is not considered in our

current research to enable us to concentrate on the levitation of the carrier. Therefore, we focus on developing a dynamic model for heave, roll, and pitch of the magnetic levitation transport system and have designed a controller for levitation, roll, and pitch. We determine the efficacy of this controller using an external load disturbance along with the sensor installation errors.

3) The section control algorithm based on the position of the carrier is developed. The levitation forces, exerted to the edges of the carrier, are reduced when the carrier moves to the next influential zone. To generate desired levitation forces profile and to minimize the fluctuations of the carrier's motion, two criteria are satisfied; the sum of the levitation forces generated by activated-levitation electromagnets should be equal to the weight of the carrier and the sum of the moment along the propulsion axis should be zero. The detailed derivation of the section control algorithms are presented in Section 5.

4) Based on theoretical analysis and simulation results, experimental works are presented to verify the levitation control performance of the carrier. Having the experimental setup, various scenarios such as levitation control performance at a standstill, levitation control performance at low-speed level, levitation control performance at high-speed level and levitation control performance at the deadzone (the levitation electromagnets are disabled) are presented.

1.2 Literature Review

1.2.1 Magnetic Levitation Train

The principle of magnetic levitation is to maintain certain airgap between two magnetized materials using repulsive or attractive forces. However, a collection of point charges (electric charge at a mathematical point without dimensions) is impossible to maintain in an equilibrium state between two magnetized materials by

Earnshaw's theorem. Therefore, sustainable control is necessary to maintain a stable airgap between two materials [6].

One of the representative applications using magnetic levitation technology is the magnetic levitation trains. This new generation transportation system was first invented as a conceptional model by Hermann Kemper of Germany in 1934 [7]. Then, magnetic levitation trains were rapidly developed in the periods from the 1960s to 1980s, commercialized magnetic levitation trains were tested in the periods of the 1990s, and public service was released in the periods of the 2000s [8-11]. Compared to wheel-based conventional automation, magnetic levitation train has many advantages to satisfy with customer demands such as low maintenance, compact, lightweight, elimination of dust, noise removal, etc. Thus, magnetic levitation train was released as one of the innovative transportation technologies for future public transportation. Despite these advanced merits, magnetic levitation trains were not easy to be commercialized owing to the difficulty of operating sustainable control and expensive costs of high-resolution sensors and high qualified controllers. Thanks to the development of highly qualified sensors and controllers with low cost in modern technologies, it could be more accessible to develop appliances using magnetic levitation technology. Having a long history of developing, testing and verifying the magnetic levitation technology, magnetic levitation trains have been developed worldwide [12].

In Germany, magnetic levitation train, Transrapid (TR) has been developed since 1969 and commercialized the TR02 in 1971 [13]. Moreover, the construction and operation of the Shanghai Maglev Line were developed, and it was commissioned in 2003 based on the control and propulsion system on the magnetic levitation transport technology of Transrapid [14]. The 9th generation train, the TR09 (as shown in Figure 1.2), could operate at a speed of 500 km/h (311 mph) and allow rapid acceleration and deceleration [15,16]. For Transrapid (TR), the levitation was accomplished using magnetic attraction force by controlled electromagnets on both sides along the



Figure 1.2. Magnetic levitation train (Transrapid 09) by Germany [16].

propulsion axis, and the propulsion was operated using linear synchronized motor (LSM).

In Japan, a high-speed maglev train was developed based on superconducting magnet (SCM) type of electrodynamic suspension (EDS) levitation and LSM propulsion technologies. Unlike electromagnetic suspension (EMS), EDS uses repulsive force between the magnetic field and the vehicle, and it is magnetically stable so that it is not necessary to control the airgap. Therefore, EDS is suitable for high-speed operation, and this high-speed magnetic levitation train achieved the fastest of 603 km/h in the operational test [17,18].

In South Korea, urban transit magnetic levitation train (UTM) has been developed since 1989 in Korea Institute of Machinery and Materials (KIMM). The first and second generation of UTM were developed with EMS and linear induction motor

(LIM) propulsion [19]. The public service version of UTM (110 km/h), Ecobee has commissioned a 6.1 km urban maglev demonstration line at Incheon International Airport by 2016 [20]. Compared to the specification of the previous version of UTMs, ECOBEE has improved the nominal airgap of 8 mm with a fluctuation of 3 mm at 110 km/h. A new generation of magnetic levitation train with a maximum speed of 550 km/h, SUMA550, is currently under development [21] as shown in Figure 1.3.



Figure 1.3. Urban magnetic levitation train (Ecobee) and SUMA 550 by South Korea [4].

1.2.2 Magnetic Levitation Transport System

The historical development of magnetic levitation transport systems for carrying displays and relevant research are presented in this section. C. Kim, et al. [22] designed a maglev conveyor system for carrying LCD glass which is shown in Figure 1.4. They used permanent magnets (PM) and electromagnets (EM) for lifting the vehicle. The operation system consists of eight EMs which are placed at each corner of the vehicle to levitate the vehicle and two linear induction motors (LIM) are installed on the upper frame to thrust the vehicle by the electromagnetic induction force. They also designed a position and levitation controller. The controller is designed as a lead-lag compensator with zero-power control to balance the attraction force and total weight. Using this system, K.Kim, et al. [23] extended the work towards the use of a multi-body dynamic model. They made a more realistic dynamic simulation for the irregularities of guide rail which was used to design an airgap control system. However, in this system, major parts (PM, EM, Linear Propulsion Motor, etc.) of the magnetic levitation conveyor system for carrying LCD glass are installed on the



Figure 1.4. Magnetic levitation conveyor system for carrying LCD glass [22].

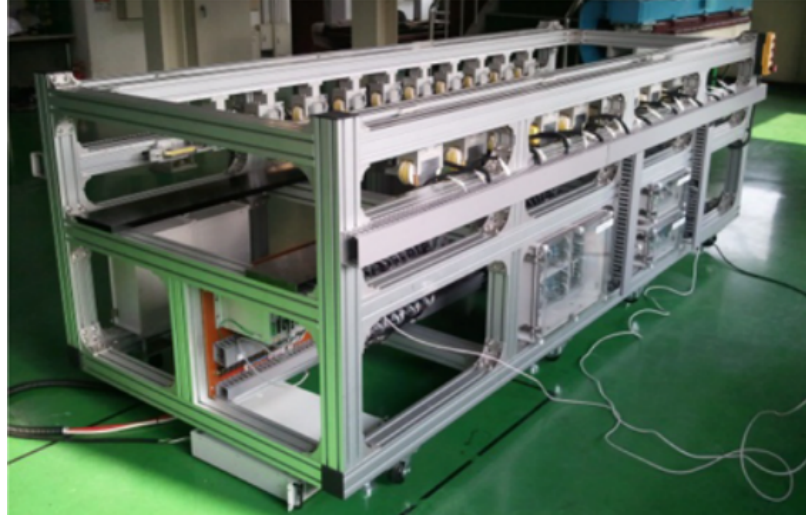


Figure 1.5. First generation of a passive magnetic levitation transport system [24].

vehicle so that the load weight was increased and this was a potential for heating sources. To compensate for these disadvantages, a first generation passive magnetic levitation transport system was designed as shown in Figure 1.5. In this system, the size and weight of the carrier are 1000 mm x 1000 mm and 150 kg, respectively. The structure of the system was designed to install the levitation electromagnets discontinuously. Major components were installed on the frame (not on the moving platform) to reduce the possibility of the thermal loading and the load weight of carrier compared to the magnetic levitation conveyor system for carrying LCD glass. In spite of these advantages, this passive magnetic levitation system still needed to be improved; the structure of the frame (made up of aluminum profile) caused an unstable vibration mode and sensor interference. Moreover, this system has a poor levitation control performance owing to the low-resolution sensor. To overcome these weaknesses, the second generation of passive magnetic levitation transport system was designed as shown in Figure 1.6. This passive magnetic levitation transport system used attraction forces to levitate the carrier which was the same as the previous generation, however, the size and weight of the carrier is increased to 2500 mm x 1000 mm and 350 kg, respectively. And, the structure of the frame is made up of



Figure 1.6. Second generation of a passive magnetic levitation transport system [26].

steel and aluminum so that the unstable vibration mode could be reduced. Using a passive magnetic levitation transport system, some control strategies have been tried including the following with varying degrees of success. The Taguchi method was used to determine the optimal control parameters of levitation controller design in the presence of noise and to achieve reliable performance [24]. J. W. Park, et al. [25] utilized a Linear Quadratic Regulator (LQR) approach to design a levitation controller based on a high fidelity model of the system. Throughout impact tests, the levitation control performance was verified to achieve a high level of accuracy and to reduce the risk of levitation failures. Y. Lee et al. [26] designed a levitation controller and developed the algorithms to accommodate a pitching motion of the carrier under the structural zones of levitation electromagnets and sensor installation errors. The levitation controller utilized a Proportional-Differential-Acceleration (PDA) controller based on the single mass system, and algorithms for reducing the pitching motion were approached using levitation forces and moment from levitation electromagnets.

1.3 Dissertation Outline

The thesis is organized as follows. The high precision magnetic levitation transport system for carrying OLED displays and the levitation controller design using cascade control strategy are described in Section 2. Section 3 presents the algorithms to estimate sensor offset using data signal processing and iterative method. Section 4 presents dynamic modeling with a small perturbation approach and controller design utilizing a LQR optimal state-feedback controller-observer compensator for roll and pitch motion. Section 5 presents a section control algorithm and its detailed derivation. Section 6 shows the experimental setup and verification under several speed levels and deadzone. Finally, the paper concludes with a summary of our work and proposed research in section 7.

1.4 List of Publications

Portions of this research have been submitted to and published in academic articles as follows:

1. Kim, J., King, G. B., Kim, C. H., & Ha, C. W. Deadzone Compensation of A High Accuracy Maglev Transportation for Carrying OLED Displays. Under review.
2. Kim, J., King, G. B., Ha, C. W., & Kim, C. H. An Experimental Implementation of Levitation Control for a High Accuracy Maglev Transport System. Under review.
3. Kim, J., King, G. B., Kim, C. H., & Ha, C. W. (2018). Modeling and designing levitation, roll and pitch controller for high accuracy maglev tray system. *Mechatronics*, 53, 181-191.
4. Kim, J., King, G. B., & Kim, C. H. (2018). Development of Algorithm to Estimate Sensor Offset in Maglev Tray System. *International Journal of Precision Engineering and Manufacturing*, 19(3), 349-358.

2. SYSTEM DESIGN

In this section, a high precision magnetic levitation transport system and its major parts are presented. A linearized dynamic analysis of heave motion using a small perturbation approach and a levitation controller design utilizing a cascade control strategy are also presented.

2.1 Magnetic Levitation Transport System

The high precision magnetic levitation transport system for carrying OLED displays is shown in Figure 2.1. In this system, the carrier is designed to carry 5th generation glass-boards. The size and weight of the carrier are 1400 mm x 1300 mm and 400 kg, respectively. The longitudinal length of the frame is approximately 4.0 m, and a carrier moving length is 2.6 m. The overall length of the system can be extended with additional modules. When active, the carrier is levitated to a gap of 1 mm under feedback control. Major components of the system are levitation electromagnets, guidance electromagnets, gap sensors, propulsion linear motor and linear encoder as shown in Figure 2.2. The guidance electromagnets are used to control the transitional movement in the lateral axis and its rotational movement (yaw). Gap sensors are used to measure the vertical displacement between carrier and levitation electromagnets, and a propulsion linear motor generates a force along its length to move the carrier. A linear encoder is used to determine the position of the carrier. All major components are installed on the upper frame (outside of carrier) to eliminate heating of the carrier and the OLED displays. Levitation electromagnets are installed on the upper frame discontinuously to levitate the carrier, and this causes a fluctuation of the carrier's motion as primary levitation forces switch from one set of levitation electromagnets to the next. To minimize the fluctuation of the carrier,

7 levitation electromagnets at the right and left sides are activated to support the carrier at any position for stability.

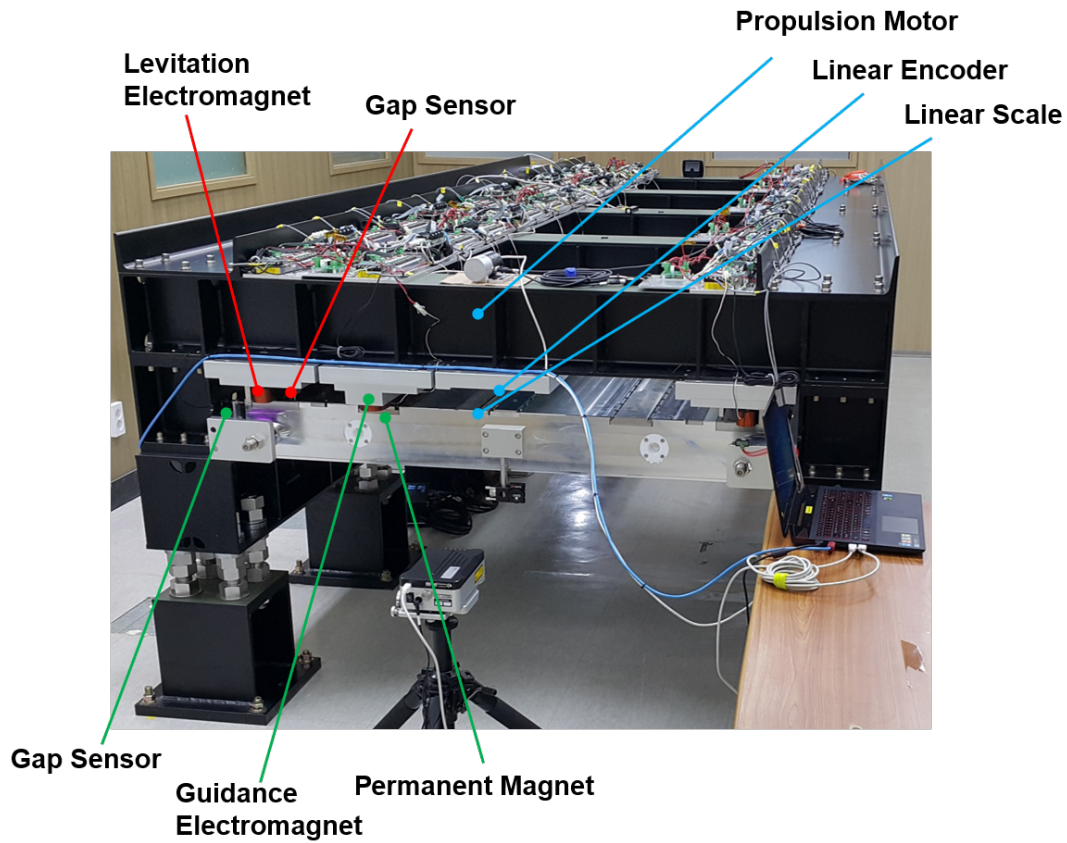


Figure 2.1. High precision magnetic levitation transport system. Major components (levitation electromagnets, gap sensors, linear motor, linear encoder and, etc) of system are not located in the moving platform so that it can reduce the load weight and the mechanical thermal expansion.

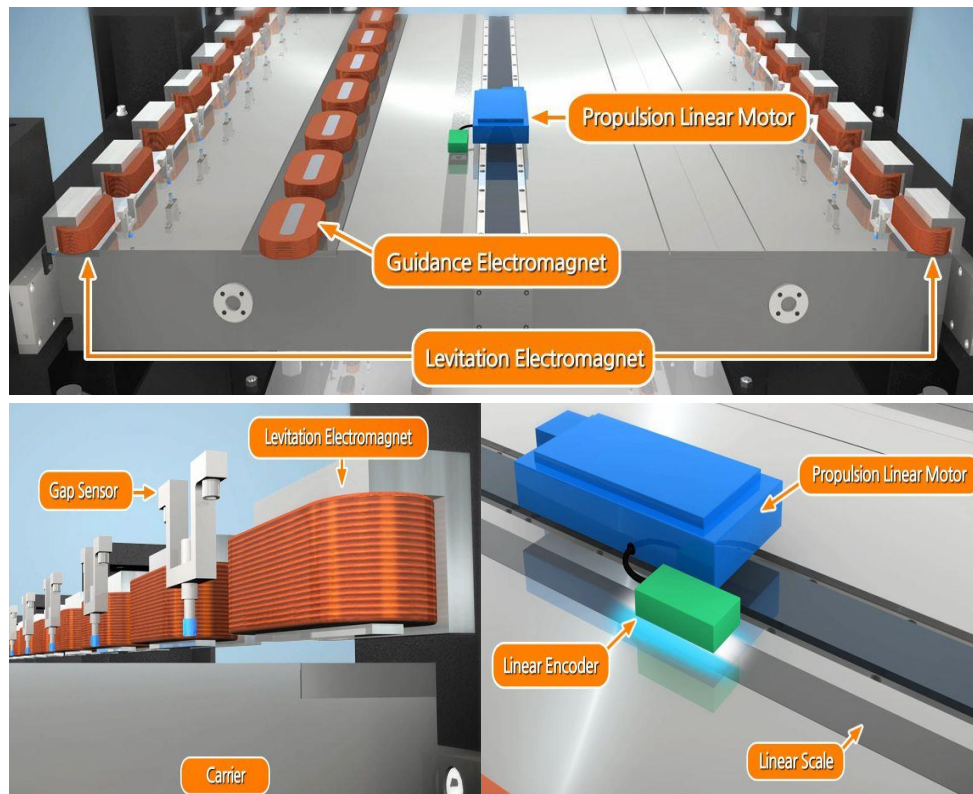


Figure 2.2. The major components of a high precision magnetic levitation transport system: the levitation electromagnets, propulsion linear motor, linear encoder, guidance electromagnets and gap sensors.

2.2 Levitation Controller Design

The purpose of the levitation controller design is to obtain the desired levitation force controlled by the applied current so that the carrier can be levitated steadily at the desired height. Therefore, the levitation controller design is one of the major issues in a magnetic levitation transportation system. In this section, the heave (vertical) motion of the carrier at the center of mass (CoM) is analyzed using each airgap exerted by the levitation electromagnets. The levitation controller is designed using a cascade control strategy, and it consists of the current controller (PI) and the airgap controller (PID). The objective of the current controller, which is located in the inner loop, is to obtain the desired levitation force and to minimize the inductive induced phase shift effect from the levitation electromagnets. The levitation force is directly proportional to the number of turns in the coil. As the number of turns in coils increases, a higher inductance is generated and a corresponding response delay between the voltage and the actual current occurs. Therefore, we design the current controller to minimize this delayed response. The input of the current controller is the difference between the reference current from the airgap controller and measurements of applied current from the current sensor. The output of the current controller is the applied voltage. The airgap controller, which is located at outer-loop, is then utilized to control the vertical displacement between the carrier and gap sensors. The input of the airgap controller is the difference between the desired gap and measurements from gap sensors and the output of the airgap controller is the reference current.

Shown in Figure 2.3 is the x , y and z axis of configuration. These axes are the propulsion, lateral and heave (vertical), respectively. In this Figure, $f_{n,l}$ and $f_{n,r}$ indicate that levitation force exerted by each levitation electromagnet on the left and right side. $c_{n,l}$ and $c_{n,r}$ indicate that airgap exerted by each levitation force on the left and right side. Similarity, b and l are breadth (width) and length of the carrier, respectively. The number of activate-levitation electromagnets at each side is n . The dynamic models of the carrier are established based on the following assumptions;

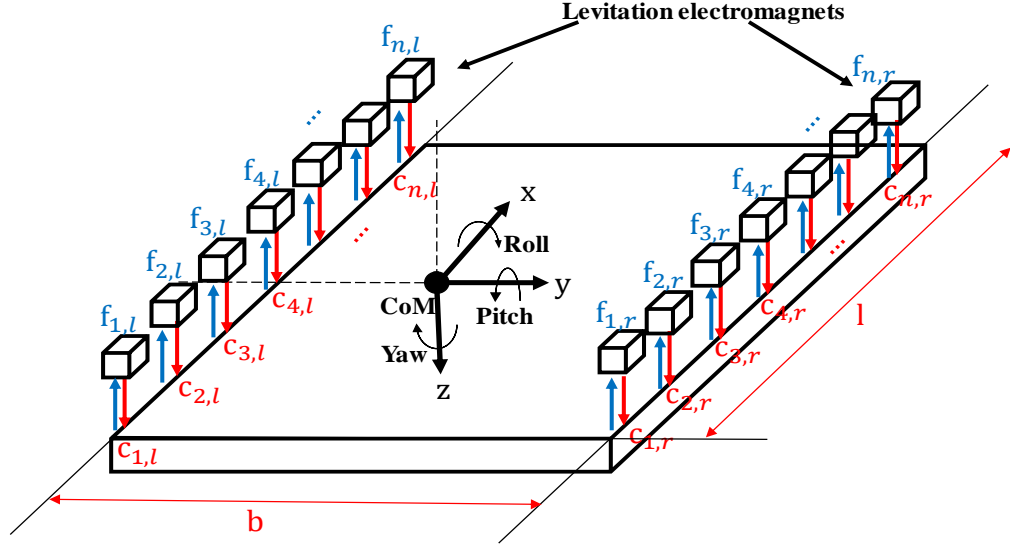


Figure 2.3. A configuration of the magnetic levitation transport system. The direction of levitation force exerted by each levitation electromagnets is up, and that of airgap is down. The carrier has six degrees of freedom.

the shape of the carrier is rectangular, it is flat, the mass of the carrier is equally distributed, lateral movement and yaw motion are constrained to the guidance electromagnets, angles of roll and pitch are relatively small, the effect of eddy current damping is relatively small and magnetic field of coils effect on each levitation electromagnet may be negligible.

2.2.1 Levitation Force and Voltage Equation

To control the vertical dynamics of magnetic levitation transport system, we analyze the levitation force and the voltage equation exerted by each electromagnet which are described by [27]

$$f_k(t) = f(i_k(t), c_k(t)) = \frac{\mu_0 N^2 A}{4} \left(\frac{i_k(t)}{c_k(t)} \right)^2, k = 1, 2, 3 \dots 2n \quad (2.1)$$

$$v_k(t) = R \cdot i_k(t) + \frac{d(L_k(t) \cdot i_k(t))}{dt}, k = 1, 2, 3 \dots 2n \quad (2.2)$$

where, $f_k(t)$ is the levitation force exerted by each electromagnet, N is number of coil turns, A is cross-sectional area of electromagnet, i_k is applied current which flows through each electromagnet ($i_k(t) = i_0 + \Delta i_k(t)$), μ_0 is the permeability of the vacuum, $c_k(t)$ is airgap exerted by each levitation electromagnet ($c_k(t) = c_0 + \Delta c_k(t)$), the applied voltage is $v_k(t)$ for each electromagnet ($v_k(t) = v_0 + \Delta v_k(t)$), small perturbation of variable is Δ , the total resistance is R , and $L_k(t)$ is inductance ($\frac{\mu_0 N^2 A}{2c_k(t)}$). Using a linear approximation with nominal equilibrium point (i_0, c_0), a small perturbation linear equation for the levitation force exerted and the voltage equation of each electromagnet can be re-written as

$$\begin{aligned}\Delta f_k(t) &= -\frac{\mu_0 N^2 A i_0}{2c_0^2} \Delta i_k(t) + \frac{\mu_0 N^2 A i_0^2}{2c_0^3} \Delta c_k(t) \\ &= -K_i \Delta i_k(t) + K_c \Delta c_k(t), k = 1, 2, 3 \dots 2n\end{aligned}\quad (2.3)$$

$$\Delta \dot{i}_k(t) = \frac{K_c}{K_i} \Delta \dot{c}_k(t) - \frac{R}{L_0} \Delta i_k(t) + \frac{1}{L_0} \Delta v_k(t), k = 1, 2, 3 \dots 2n \quad (2.4)$$

where, $K_i = \frac{\mu_0 N^2 A i_0}{2c_0^2}$, and $K_c = \frac{\mu_0 N^2 A i_0^2}{2c_0^3}$. Total resistance of the magnetic circuit consists of the core reluctance (R_c) and the airgap reluctance (R_g). The core reluctance is written as $R_c = L_c / \mu_0 \mu_r A$ where, L_c is core path length and μ_r is the relative permeability of ferromagnetic materials in the core of levitation electromagnet, respectively. The airgap reluctance is written as $R_g = c_k / \mu_0 A$. Therefore, total resistance can be written as $R = R_c + R_g = L_c / \mu_0 \mu_r A + c_k / \mu_0 A = 1 / \mu_0 A (L_c / \mu_r + c_k)$. Since the relative permeability is large, L_c / μ_r may be negligible and the airgap dominates total resistance [4,28].

2.2.2 Dynamic Equation of Heave Motion

The relationship between each airgap and the heave from the center of the mass (CoM) is developed in this section. The airgap relationship can be expressed as [27]

$$c_{cg}(t) = \frac{\sum_{k=1}^n c_{k,r}(t) + \sum_{k=1}^n c_{k,l}(t)}{2n} \quad (2.5)$$

where, $c_{cg}(t)$ represents the heave motion of carrier at center of mass (CoM). We then analyze the dynamics of heave motion as shown in Figure 2.4. The heave motion of carrier at center of mass (CoM) can be expressed as

$$m\ddot{c}_{cg}(t) = -\sum_{k=1}^n (f_{k,r}(t) + f_{k,l}(t)) + mg + f_d(t) \quad (2.6)$$

where, m is mass of the carrier, g is gravitational acceleration ($9.81m/s^2$), and $f_d(t)$ is a load disturbance force. This yields a linearized equation of the levitation force for a small perturbation and the dynamic heave motion without load disturbance force given by

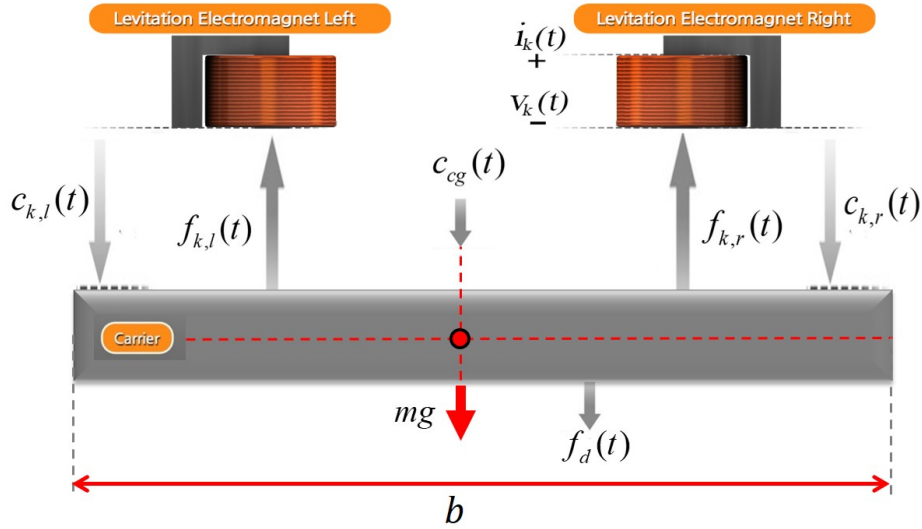


Figure 2.4. Configuration of the carrier's heave motion at center of mass. The direction of levitation force at the right and left side are up and the direction of airgap at the right and left side is down. The direction of both gravitational force and a load disturbance force is down. The heave at CoM is expressed from the relationship between each airgap.

$$\Delta \ddot{c}_{cg}(t) = -\frac{K_i}{m} \sum_{k=1}^n (\Delta i_{k,r}(t) + \Delta i_{k,l}(t)) + \frac{K_c}{m} \sum_{k=1}^n (\Delta c_{k,r}(t) + \Delta c_{k,l}(t)) \quad (2.7)$$

Using the airgap relationship from equation 2.5, dynamic equation of the heave motion can be simplified as

$$\Delta \ddot{c}_{cg}(t) = -\frac{K_i}{m} \sum_{k=1}^n (\Delta i_{k,r}(t) + \Delta i_{k,l}(t)) + \frac{2nK_c}{m} \Delta c_{cg}(t) \quad (2.8)$$

2.2.3 Current Controller Design

The objective of designing the current controller (inner-loop) is to control the applied current precisely so that the desired-levitation force can be obtained. Moreover, the current controller is designed to reduce the inductance related effects from levitation electromagnets. The input of the current controller is the difference between the reference current (generated by airgap controller) and applied current (measured by a current sensor). The output of the current controller is the applied voltage. In our system, maximum applied voltage level setup is 150 V to obtain a fast response for the current controller. From equation 2.4, the simplified voltage equation ($\Delta \dot{c}_k(t) = 0$) can be re-written as

$$\Delta \dot{i}_k(t) \simeq -\frac{R}{L_0} \Delta i_k(t) + \frac{1}{L_0} \Delta v_k(t), k = 1, 2, 3 \dots 2n \quad (2.9)$$

The simplified voltage equation in the time domain can be converted into the s-domain as

$$\begin{aligned} s \Delta I_k(s) &\simeq -\frac{R}{L_0} \Delta I_k(s) + \frac{1}{L_0} \Delta V_k(s) \\ &= -\frac{R}{L_0} \Delta I_k(s) + \frac{C_c}{L_0} (\Delta I_{ref,k}(s) - \Delta I_k(s)), k = 1, 2, 3 \dots 2n \end{aligned} \quad (2.10)$$

where, $\Delta V_k(s) = C_c(\Delta I_{ref,k}(s) - \Delta I_k(s))$ and C_c is the current controller. From this simplified voltage equation in the s-domain, the open-loop and closed-loop transfer functions of current system can be obtained as

$$G_c^o(s) = \frac{C_c}{L_0s + R} = \frac{k_{pc}s + k_{ic}}{s(L_0s + R)} \quad (2.11)$$

$$G_c^c(s) = \frac{\Delta I_k(s)}{\Delta I_{ref,k}(s)} = \frac{C_c}{L_0 + R + C_c} = \frac{k_{pc}s + k_{ic}}{L_0s^2 + (R + k_{pc})s + k_{ic}} \quad (2.12)$$

where, k_{pc} and k_{ic} are current control gains, $G_c^o(s)$ is the open-loop transfer function of inner-loop and $G_c^c(s)$ is the closed-loop transfer function of inner-loop. The current controllers are designed as a Proportional-Integral (PI) controller with gains chosen as the same value for all current controllers. The characteristic equation of closed-loop transfer function of current system is $L_0s^2 + (R + k_{pc})s + k_{ic} = 0$. To obtain desired gain of current controller, we use a pole-zero cancellation in the open-loop transfer function. This is accomplished by setting the zero of $G_c^o(s)$ ($\frac{-k_{ic}}{k_{pc}}$) to the pole of the system ($\frac{-R}{L_0}$), and thus these two components cancel and inductance effect from levitation electromagnets are removed. In analysis of system type and steady-state error, $G_c^o(s)$ is a type 1 system, which includes $\frac{1}{s}$ and steady state error to a step input is zero since the static error constant is infinity. Having the condition of $\frac{k_{ic}}{k_{pc}} = \frac{R}{L_0}$, $G_c^o(s)$ and $G_c^c(s)$ are re-written as

$$G_c^o(s) = \frac{k_{pc}}{L_0s} \quad (2.13)$$

$$G_c^c(s) = \frac{k_{pc}}{L_0s + k_{pc}} \quad (2.14)$$

This is a first order response of $G_c^c(s)$, where ω_c is defined as the frequency at which magnitude of the output attenuates to 0.707 of the peak. In $G_c^c(s)$, ω_c is $\frac{k_{pc}}{L_0}$ which allows the response of current system to increase with the value of k_{pc} . Choosing

$\omega_c = 2\pi \times 300$, the relationship between gains of current controllers and cut-off frequency is written as

$$\begin{aligned} k_{pc} &= L_0 \omega_c \\ k_{ic} &= \frac{R}{L_0} k_{pc} = R \omega_c \end{aligned} \quad (2.15)$$

According to the equations above, the current control gains are related to L_0 and R . Therefore, accurate system characterization of the levitation electromagnets is a critical factor in the performance of the current controller. Having determined the optimal control gains of the current controller, Figure 2.5 shows that the applied current signal has good performance to the track of the desired current signal (0.5 A amplitude) at 300 Hz which represents the control bandwidth of the current control loop.

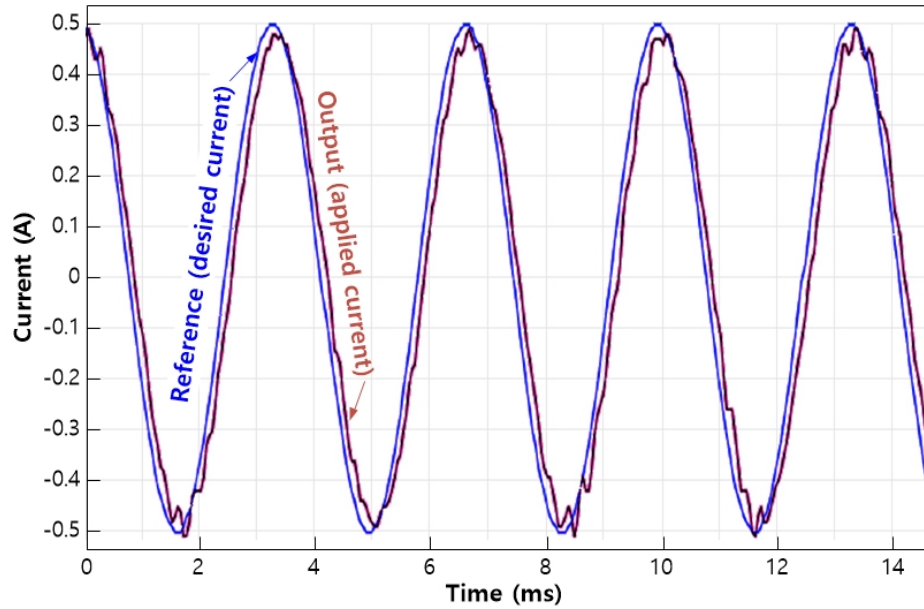


Figure 2.5. The tracking performance utilizing designed current controller at 300Hz. The blue line represents the reference current signal and the red line represents the applied current signal with the optimal control gains of the current controller, respectively.

2.2.4 Airgap Controller Design

In the following section, the airgap controller (outer-loop) is designed to obtain the desired airgap of 1 mm between the carrier and the levitation electromagnets. The input of airgap controller is the difference between the reference airgap and measurements from each gap sensor. The output of the airgap controller is the reference current that flows into each current controller. With this approach and equation 2.8, a linearized equation of the heave motion can be re-written in the s-domain as

$$s^2 \Delta C_{cg}(s) \simeq \frac{-14K_i C_L}{m} \Delta C_{ref} + \left(\frac{14K_i C_L}{m} + \frac{14K_c}{m} \right) \Delta C_{cg}(s) \quad (2.16)$$

where, C_L is the airgap controller, $\Delta C_{ref} = 0$ and $\Delta I_k(s) \simeq \Delta I_{ref,k}(s) = C_L(\Delta C_{ref} - \Delta C_k(s))$. From above equation, we obtain the open-loop and closed-loop transfer functions of airgap feedback loop as

$$G_L^o(s) = \frac{-K_i C_L}{\frac{m}{14}s^2 - K_c} = \frac{-(K_i k_{dL}s^2 + K_i k_{pL}s + K_i k_{iL})}{s(\frac{m}{14}s^2 - K_c)} \quad (2.17)$$

$$\begin{aligned} G_L^c(s) &= \frac{\Delta C_{cg}(s)}{\Delta C_{ref}} = \frac{-14K_i C_L}{ms^2 - 14K_i C_L - 14K_c} \\ &= \frac{-K_i k_{dL}s^2 - K_i k_{pL}s - K_i k_{iL}}{\frac{m}{14}s^3 - K_i k_{dL}s^2 - (K_i k_{pL} + K_c)s - K_i k_{iL}} \end{aligned} \quad (2.18)$$

where, k_{pL} , k_{dL} and k_{iL} are the airgap control gains, $G_L^o(s)$ is the open-loop transfer function of outer-loop and $G_L^c(s)$ is the closed-loop transfer function of outer-loop.

The form of the airgap controller is a Proportional-Integral-Derivative (PID) controller to maintain the desired airgap. The system type and steady-state error of $G_L^o(s)$ is type 1, which includes $\frac{1}{s}$ so that steady state error at step input is zero. The characteristic equation of the closed-loop transfer function of the airgap feedback loop is written as

$$\frac{m}{14}s^3 - K_i k_{dL}s^2 - (K_i k_{pL} + K_c)s - K_i k_{iL} = 0 \quad (2.19)$$

The characteristic equation of the closed-loop transfer function of airgap feedback loop is third-order system and it compares to the desired characteristic equation, $(s + p_1)(s^2 + 2\zeta\omega_n s + \omega_n^2) = 0$ to obtain appropriate airgap controller gains. The airgap controller gains are formulated as

$$\begin{aligned} k_{pL} &= \frac{-(K_c + \frac{m}{14}(\omega_n^2 + 2\zeta\omega_n p_1))}{K_i} \\ k_{iL} &= \frac{-\frac{m}{14}p_1\omega_n^2}{K_i} \\ k_{dL} &= \frac{-\frac{m}{14}(p_1 + 2\zeta\omega_n)}{K_i} \end{aligned} \quad (2.20)$$

where, ζ is damping ratio of system ($\zeta = 0.707$), ω_n is natural frequency of system ($\omega_n = 2\pi \times 30$), and p_1 is a selected-3rd pole in the desired characteristic equation ($p_1 = 5\omega_n$).

2.2.5 Levitation Controller Verification

The control block diagram for the entire feedback loop is shown in Figure 2.6. We analyze the integrated inner- and outer-loop feedback of the system to verify the stability of our designed controllers. Assuming response of the current feedback loop is sufficiently faster than that of airgap feedback loop. To examine this assumption and verify the cascade controller design, we first formulate the closed-loop transfer function of the integrated inner- and outer-loop feedback without any assumptions. The closed-loop transfer function of the integrated inner-loop and outer-loop feedback in consideration of $\Delta\dot{c}_k$ can be expressed as

$$\begin{aligned} G_{CL}^c(s) &= \frac{-K_i C_c C_L}{\frac{m}{14}L_0 s^3 + \frac{m}{14}(R + C_c)s^2 - (K_i C_c C_L + K_c R + K_c C_c)} = \\ &= \frac{-K_i k_{pc} k_{dL} s^3 - (K_i k_{pc} k_{pL} + K_i k_{ic} k_{dL})s^2 - (K_i k_{pc} k_{iL} + K_i k_{ic} k_{pL})s - K_i k_{ic} k_{iL}}{\frac{m}{14}L_0 s^5 + (\frac{m}{14}R + \frac{m}{14}k_{pc})s^4 + (\frac{m}{14}k_{ic} - K_i k_{pc} k_{dL})s^3 - (K_i k_{pc} k_{pL} + K_i k_{ic} k_{dL} + K_c R + K_c k_{pc})s^2 - (K_i k_{pc} k_{iL} + K_i k_{ic} k_{pL} + K_c k_{ic})s - K_i k_{ic} k_{iL}} \end{aligned} \quad (2.21)$$

where, $G_{CL}^c(s)$ is the closed-loop transfer function of the integrated inner-loop and outer-loop feedback with $\Delta\dot{c}_k \neq 0$.

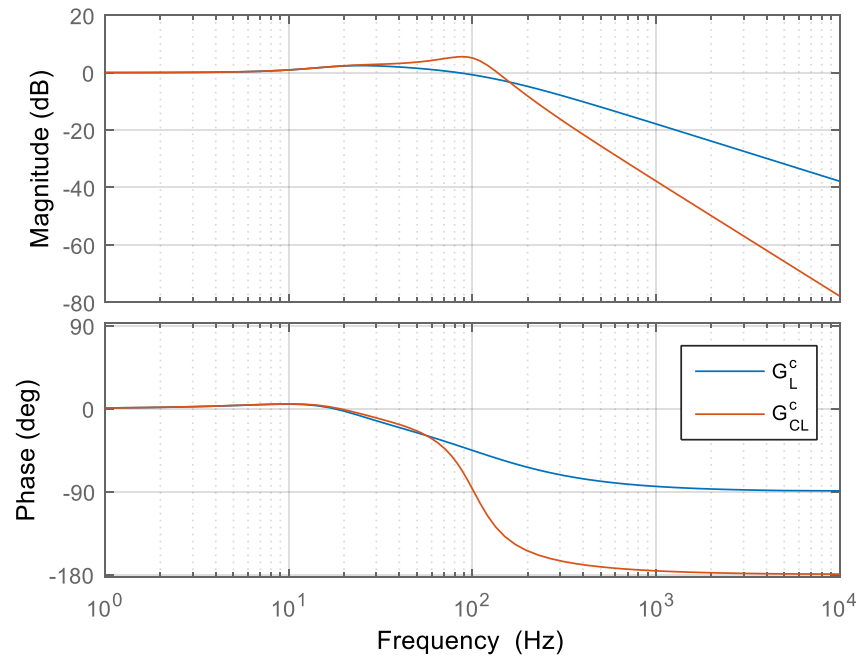


Figure 2.7. Frequency response of $G_L^c(s)$ and $G_{CL}^c(s)$. $G_L^c(s)$ is the closed-loop transfer function of airgap feedback loop ($\Delta\dot{c}_k \approx 0$) and $G_{CL}^c(s)$ is the closed-loop transfer function of the entire levitation feedback loop ($\Delta\dot{c}_k \neq 0$). The response of these two closed-loop transfer function are similar at low frequencies (less than 30 Hz).

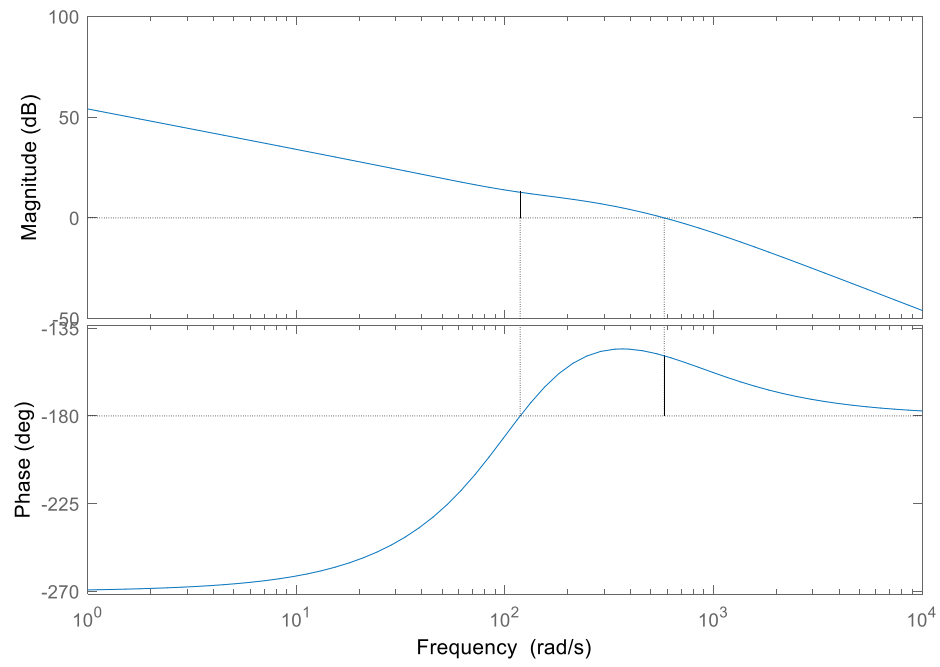


Figure 2.8. The bode plot of the open-loop transfer function of the overall levitation system, $G_{CL}^o(s)$.

In addition to designing the levitation controller, there are practical problems that should be solved to implement the levitation control performance of the carrier. A large oscillation occurs when the carrier is activated to levitate, which phenomenon is called as resonance, and airgap measurement from gap sensors has noise in the high frequency ranges. These systematic issues can be a negative impact on the levitation control performance. To minimize a mechanical resonance of the carrier, a natural frequency of the carrier is obtained by impact test. As shown in Figure 2.9, the frequency of the carrier where it is excited to the vibration mode is about 180 Hz; the notch filter attenuates it. A high order term of notch filter can be designed to reduce excitation frequency. However, a phase shift can occur so that it causes a negative impact on the stability of the levitation control system; magnetic levitation transport system is required to guarantee the stability at desired airgap for a long term. Therefore, a second order notch filter is the most suitable filter design to reduce the excitation mode of the carrier in our case. To minimize the noise in the

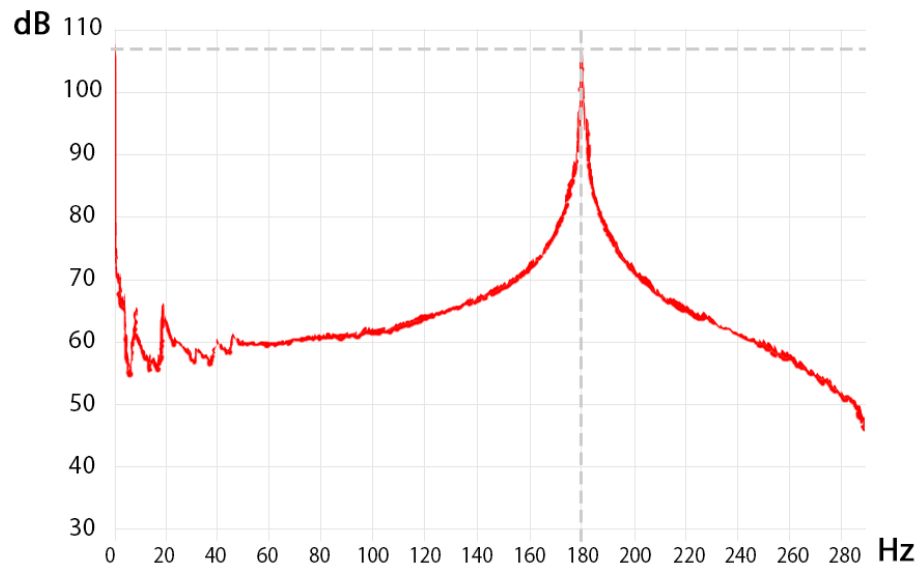


Figure 2.9. The magnitude of the frequency response by impact test.

high frequency ranges from the gap sensors, a first order low pass filter is used. Using Fast Fourier Transform (FFT), the peak of the airgap measurement in the frequency domain at around 30 Hz can be found. That is, levitation control loop performs under 30 Hz which is in the low-frequency range. Therefore, a low pass filter is designed to reduce noise in the high-frequency ranges. A high order low pass filter is not suitable because a time delay effect is increased; the levitation control performance is worsened. The configurations of the notch filter and low pass filter are shown in the levitation control block diagram.

3. SENSOR OFFSET ESTIMATION

3.1 Sensor Characterization

The gap sensor, which is a non-contact measuring system, is used to measure the vertical displacement between the carrier and the sensor. In the magnetic levitation transport system, 20 gap sensors are installed on the right and left sides of the upper frame, and these sensors are located right next to the levitation electromagnets. Therefore, it provides airgap measurements to the levitation control loop.

The operation of the gap sensor is shown in Figure 3.1. It includes a converter operated by DC power supply then, a high-frequency current in the sensor coil is generated by the converter. The magnetic field around the sensor coil produced by high-frequency current induces small current (eddy-current) in the conductive material (target). The eddy-current acts on changing the impedance of sensor coil as the

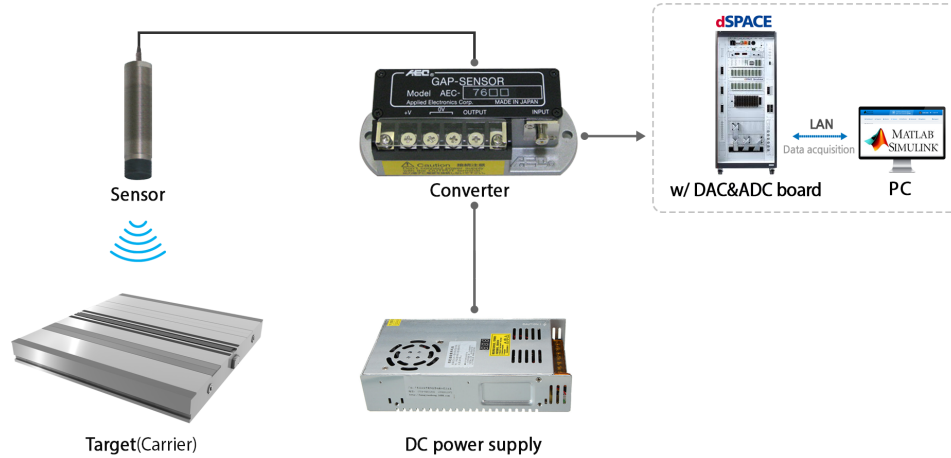


Figure 3.1. A simplified schematic structure of gap sensor.

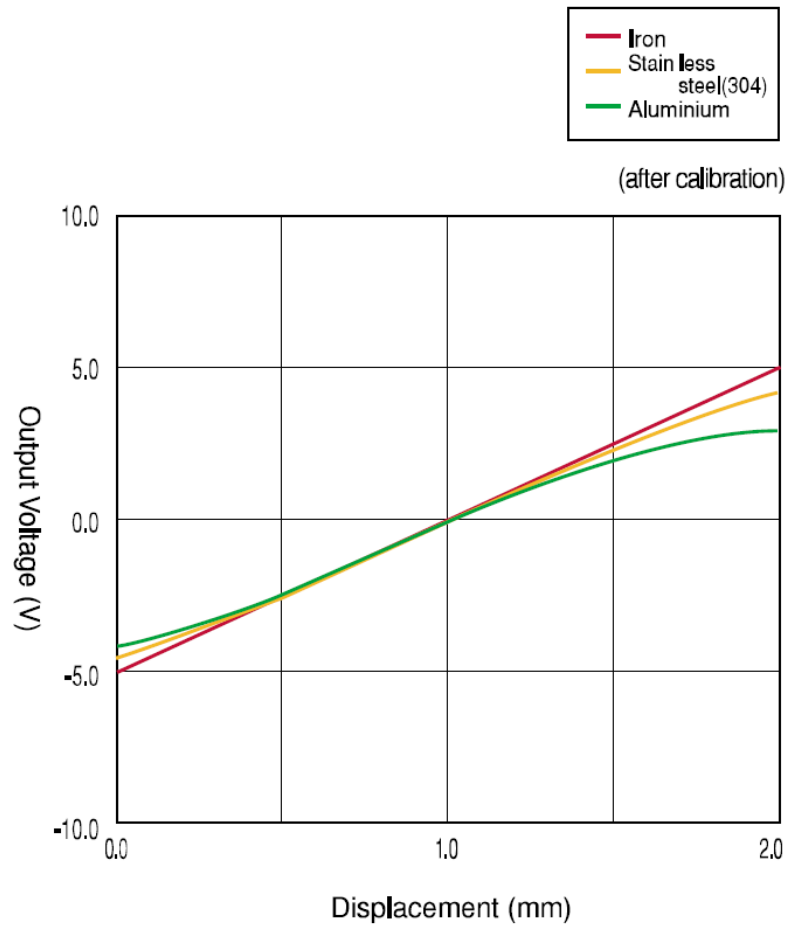


Figure 3.2. Output characteristics of gap sensor. Since the carrier is covered by iron, accurate measurement can be obtained 1 mm of the desired gap.

distance between sensor and target changes. The output is produced as an analog voltage which is proportional to change in the displacement between the sensor and the target as shown in Figure 3.2. An analog output voltage is converted into the displacement by the Analog-to-Digital Converters (ADC) of dSPACE. In our system, we use PU-05 as the gap sensor and AEC-76 as the converter (manufactured by AEC) as shown in Table 3.1 and Figure 3.3. There is no measurable linearity error in the output characteristic, and thus accurate measurement is obtained under 1 mm levitation state.

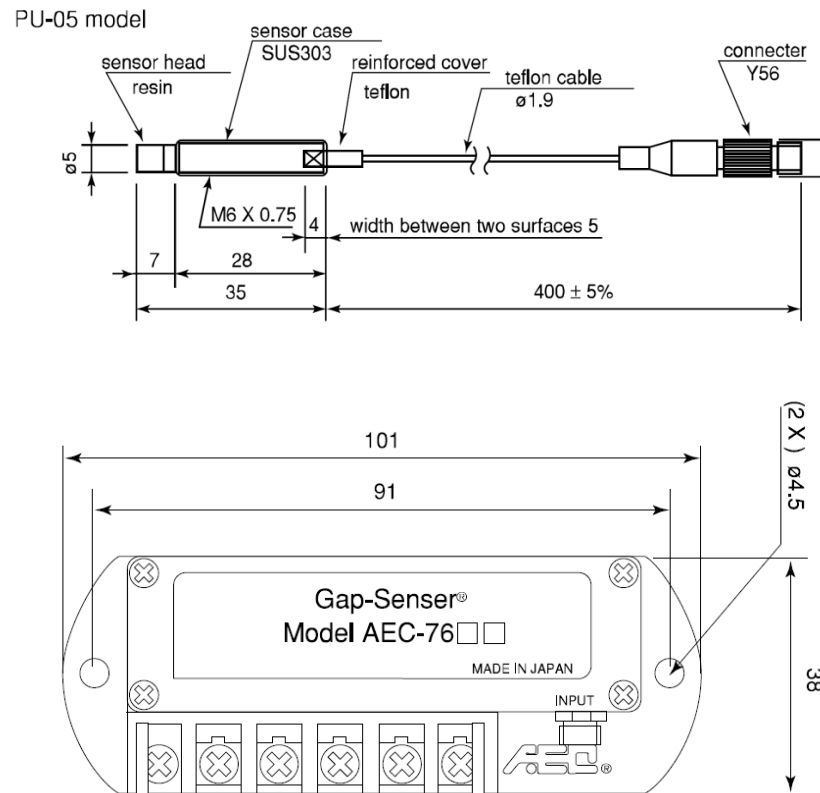


Figure 3.3. Gap sensor (PU-05) and Converter (AEC-76). The unit of dimension is mm.

Table 3.1. Specifications of PU-05 and AEC-76. The measuring range of gap sensor (Iron) is from 0 - 2 mm and its output voltage is ± 5 V. The resolution of gap sensor has $0.5 \mu\text{m}$ - $0.8 \mu\text{m}$ and both gap sensor and converter can operate at room temperature. The sampling frequency of the converter is 20 kHz so that the data can be acquired with 0.00005 seconds of the sampling interval.

-	PU-05	AEC-76
Measuring range(Iron)	0 - 2 mm (0:0.05 mm)	N/A
Output voltage	± 5 V (0.02 mm/V)	N/A
Resolution	$0.5 \mu\text{m}$ - $0.8 \mu\text{m}$	N/A
Temperature range	-20° to 180°	-10° to 70°
Frequency	N/A	DC to 20 kHz
Power supply	N/A	± 11 V to 26 V

3.2 Measurement Error

Measurement error from the gap sensor is one of the main causes of the carrier motion instability. This leads to a negative effect on the transport of OLED displays. The majority of the measurement errors are caused by vertical misalignment and sensor head adjustment. When the gap sensors are installed on the upper body frame, misalignment of the sensor installation in the vertical axis can occur. This measurement error impacts the accuracy of the measurements. Moreover, the sensor head may be adjusted by users so that the vertical position of each sensor head can be varied. Besides, measurement errors can also occur owing to the resolution of the sensor, levitation accuracy and tilt angle of each sensor. These causes, however, are negligible in comparison. Therefore, misalignment in the vertical axis and sensor head misadjustment are considered as the major sources of sensor installation error [29].

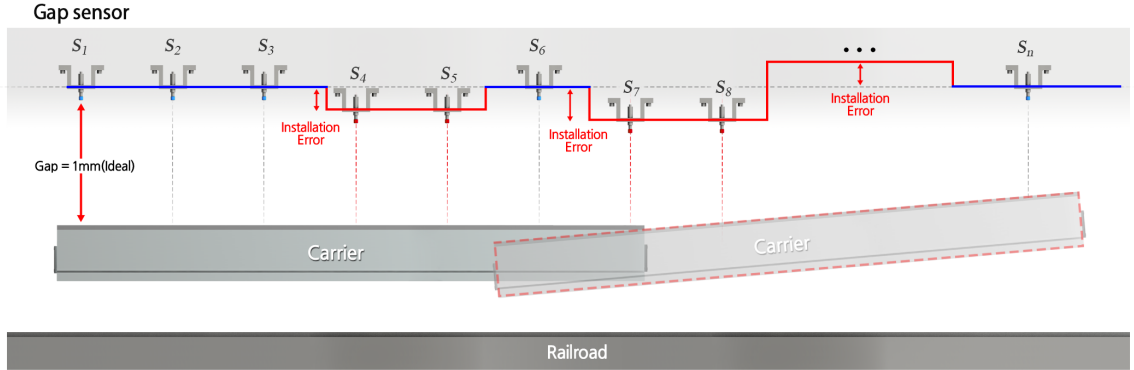


Figure 3.4. Schematic view of the sensor installation error. As the carrier is levitated from the railroad, the desired gap between the carrier and the gap sensor (S_n) is 1 mm. Due to sensor installation error, the carrier motion can fluctuate as it moves along the propulsion axis.

When the speed of the carrier is slow, the levitation controller has enough time to settle, so that gap fluctuation is small. However, the levitation controller has a short time to perform so that the measurement of the gap has more variations as the speed of carrier increases. In consideration of the fact that sensor installation error affects the motion of carrier, it is necessary to estimate this error and to calibrate sensor offset in the magnetic levitation transport system. Sensor installation error is an unknown variable, and it depends on the alignment shown in Figure 3.4. As vertical displacement between the carrier and each sensor is measured at a non-levitation state, it is noticed that the measurements from the first and last alignment of gap sensors are around 2 mm within $10\ \mu\text{m}$ so this alignment of these sensors is assumed as the reference alignment (non-installation error). Even if it were possible to measure all the sensor installation errors separately at the non-levitation state, it would be a long sequence time and this process would be inefficient. Therefore, we develop an algorithm to estimate installation error for all gap sensors simultaneously.

3.3 Analysis of truncated temporal measurement

Among the raw measurements at the various speeds of the carrier, the airgap measurement at the highest speed of the carrier (500 mm/s) is chosen because it is easy to observe and analyze the fluctuation of the carrier's motion at this speed throughout data signal processing. The raw measurement from one of the gap sensors is shown in Figure 3.5. The initial state of the airgap measurement from 0 to 0.4 sec is identified as the levitating condition in which the carrier levitates at the desired airgap. After the carrier is levitated at a standstill, it begins to move, and the gap sensors are activated until 3 sec. Then, the carrier moves to the next stage, and the current gap sensors are deactivated. Since we need to find fluctuations caused by sensor installation error in the moving period, we truncate the moving condition of the raw measurement. After this truncation process, we analyze the single-sided amplitude spectrum using a Fast Fourier Transformation (FFT) analysis.

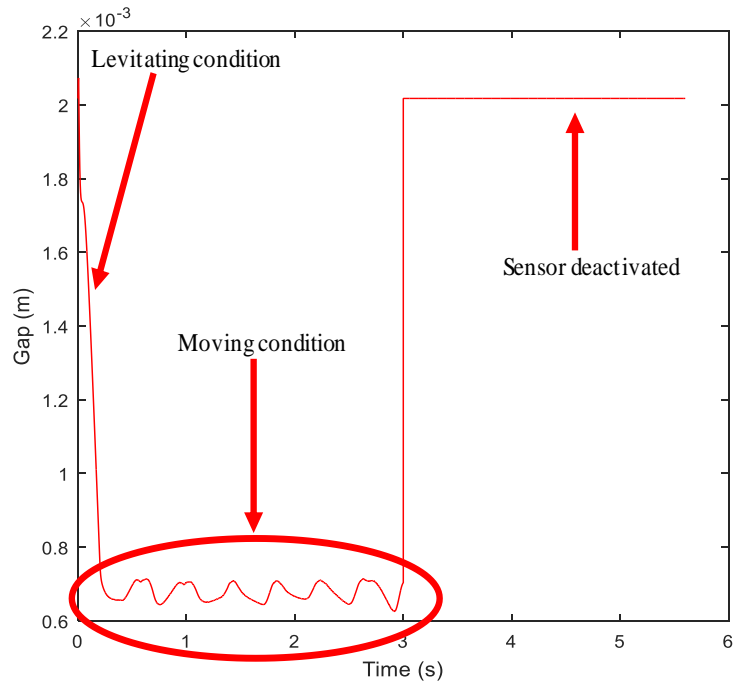


Figure 3.5. The raw measurement at 500 mm/s speed from the gap sensor. The levitating condition is from 0 to 0.4 sec where the carrier levitates at the desired gap. The moving condition is from 0.4 to 3 sec where the carrier moves. The gap sensors are deactivated, and the carrier moves to the next allocation after 3 sec.

3.4 Fast Fourier Transform Analysis

Fourier transform converts a signal from time domain to frequency domain and frequency domain to time domain. The Fourier transform can be computed using the Discrete Fourier Transform (DFT) and its inverse. Fast Fourier transform (FFT) has been widely used in data signal processing [30-32]. In our research, truncation measurements from the gap sensor are used to compute FFT algorithms with MATLAB. After performing FFT, we plot the single-sided amplitude spectrum to estimate the peak of the truncation measurement over the frequencies. As shown in Figure 3.6, the peak frequency occurs at 2.4414 Hz which represents about 6 fluctuations generated in less than 3 seconds. Other high frequencies indicate the measurement noise from the sensor itself and levitation accuracy of the carrier.

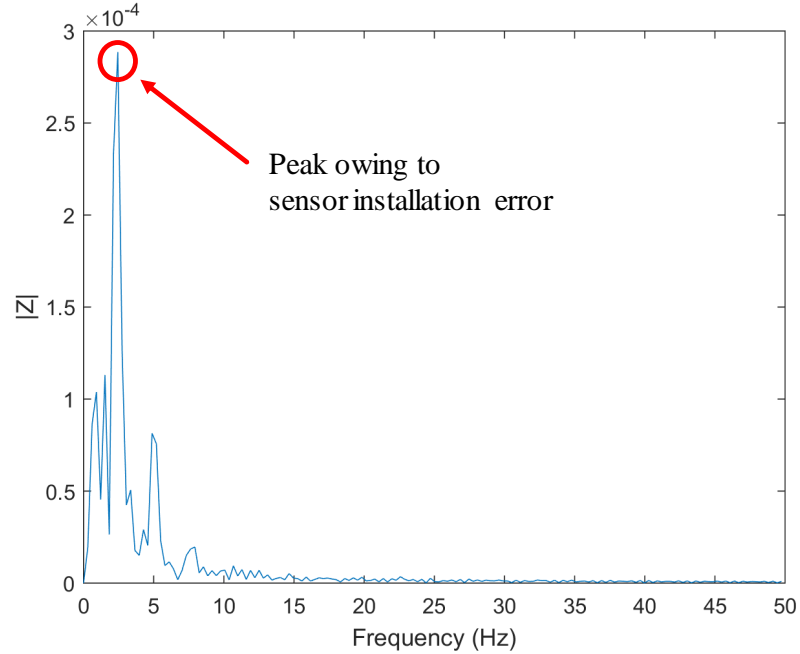


Figure 3.6. The single-sided amplitude spectrum of truncation measurement with sensor offset. The peak occurs due to the fluctuation of the carrier, and other high frequencies are the measurement noise and levitation accuracy.

Amplitude spectrum using FFT is related to the number of measurements in the time domain [33]. Therefore, we truncate the same number of measurements from each sensor and compare its peak in the frequency domain as a change in sensor offsets. The Fourier transform relates signals in the time domain and in the frequency domain. The Fourier transform possesses the property of homogeneity [34]. Homogeneity is that change of amplitude spectrum in the time domain produces an identical change of amplitude in the frequency domain as shown in Figure 3.7.

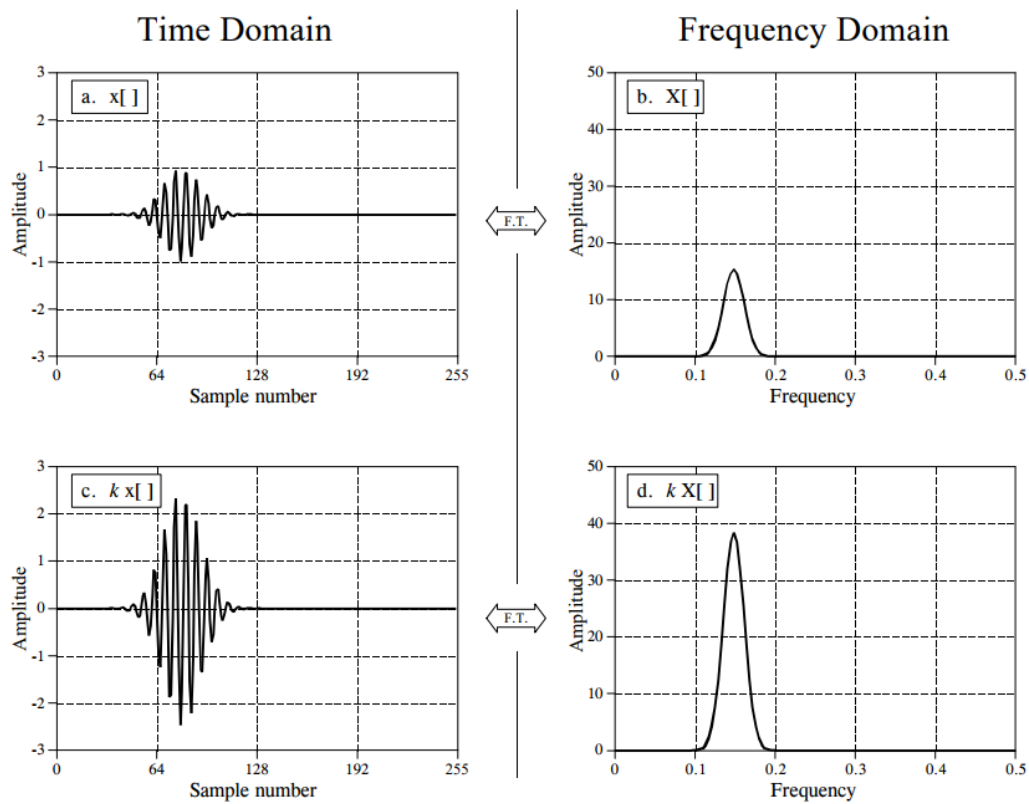


Figure 3.7. Homogeneity of the Fourier transform. The amplitude modulation is changed in the time domain as it produces an identical change in the frequency domain [34].

In our system, amplitude modulation of truncation measurements increases as an increment of the sensor installation error in the time domain and the increase is also shown in the frequency domain following homogeneity of the Fourier transform. Therefore, we apply random variables of sensor offset in the range of $-50 \mu\text{m}$ to $50 \mu\text{m}$ [26] and analyze truncated measurements with it. After finding amplitude modulation of measurement using FFT and analyzing the homogeneity of the Fourier transform, a correlation between the sensor offset and the amplitude modulation is observed. Then we develop an algorithm to estimate the parameters in a linear equation.

3.5 Correlation Between Amplitude and Sensor Offset

To estimate the correlation between amplitude modulation and the sensor offset, we collect amplitudes of truncated measurement sets to change in the sensor offsets. We then set up and simulate four conditions to estimate the minimum and maximum values of parameters in the equation as follows:

Condition 1: A random variable of one sensor offset in the range of $-50 \mu\text{m}$ to $50 \mu\text{m}$ and zeros of other sensor offsets.

Condition 2: A random variable of one sensor offset in range of $-50 \mu\text{m}$ to $50 \mu\text{m}$ and $-50 \mu\text{m}$ of other sensor offsets.

Condition 3: A random variable of one sensor offset in range of $-50 \mu\text{m}$ to $50 \mu\text{m}$ and $50 \mu\text{m}$ of other sensor offsets.

Condition 4: A random variable of one sensor offset and static-arbitrary values of other sensor offsets: both are in the range of $-50 \mu\text{m}$ to $50 \mu\text{m}$.

These four conditions are tested to estimate the mathematical relationship between the amplitude modulation and the sensor offset. The fitted curves are produced as shown in Figure 3.8.

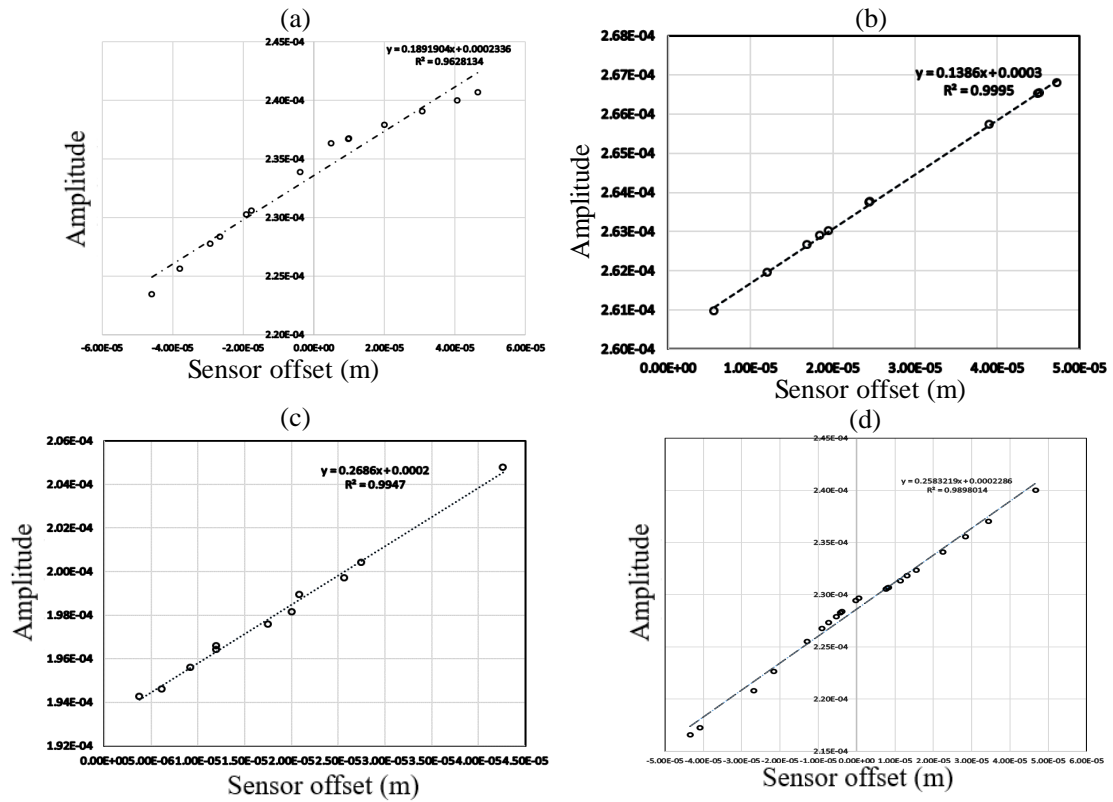


Figure 3.8. The fitted curves for each condition: (a) condition 1: a random variable of one sensor offset and zeros of other sensor offsets. (b) condition 2: a random variable of one sensor offset and the minimum value of other sensor offsets. (c) condition 3: a random variable of one sensor offset and the maximum value of other sensor offsets. (d) condition 4: random variable of one sensor offset and static-arbitrary values of other sensor offsets.

As seen in Figure 3.8, the fitted curves of all conditions show a linear model with above 96 percent for R^2 (coefficient of determination). Therefore, we establish a linear equation of the amplitude modulation and the sensor offset as

$$y = ax + b \quad (3.1)$$

where, a and b are unknown parameters in a linear equation, respectively, y is the amplitude modulation of fluctuation in the frequency domain, and x is the sensor offset. Based on the parameters from the fitted curves in conditions 2 and 3, we estimate parameter bounds as

$$\min(a) \leq a \leq \max(a) \quad \text{and} \quad \min(b) \leq b \leq \max(b) \quad (3.2)$$

where, minimum and maximum values of a and b are 0.1386, 0.2686 and 0.0002, 0.0003, respectively.

3.6 Estimation of Parameters in Linear Equation Using Iteration Method

The iteration method is a mathematical process that produces a sequence of estimates to approximate the solution, and it is called convergent if a sequence converges to the approximation. One of the useful iterative methods is the Jacobi method which is an algorithm to find the solutions using a diagonally dominant system of linear equations [35]. However, the Jacobi method is only valid for the specification that parameters set up in linear systems. Therefore, we develop a novel algorithm based on the iteration method to estimate parameters in a linear equation. The procedure used in the iteration method to estimate sensor offset is described as follows:

Step 1. Set up an initial linear equation using minimum parameters $\min(a) = \hat{a}_0$ and $\min(b) = \hat{b}_0$ then calculate sensor offset (\hat{x}_k) using the amplitude modulation of fluctuation (y).

Step 2. After calibrating the sensor offset from the truncated measurement, we find the peak to peak values (which is the difference between the maximum and minimum amplitude modulation of fluctuation). If the peak to peak value is less than tolerance as $10 \mu\text{m}$, we assume that calculated sensor offset (\hat{x}_k) from step 1 is the true value.

Step 3. If the peak to peak value is equal or greater than tolerance as $10 \mu\text{m}$, we apply the combination of estimated parameters \hat{a}_i and \hat{b}_j into the linear equation, where, \hat{a}_i and \hat{b}_j are computed to increase with rate of $0.0002 (\delta a)$ and $0.000002 (\delta b)$ which are around 1 percent of each parameter. The combinations of \hat{a}_i and \hat{b}_j are used to converge to the tolerance through the process of trial and error.

Step 4. After trial and error from step 3, we obtain the new sensor offset which is less than the tolerance ($10 \mu\text{m}$).

Step 5. After estimating the true value of the sensor offset, the iteration process stops. The process diagram is shown in Figure 3.9.

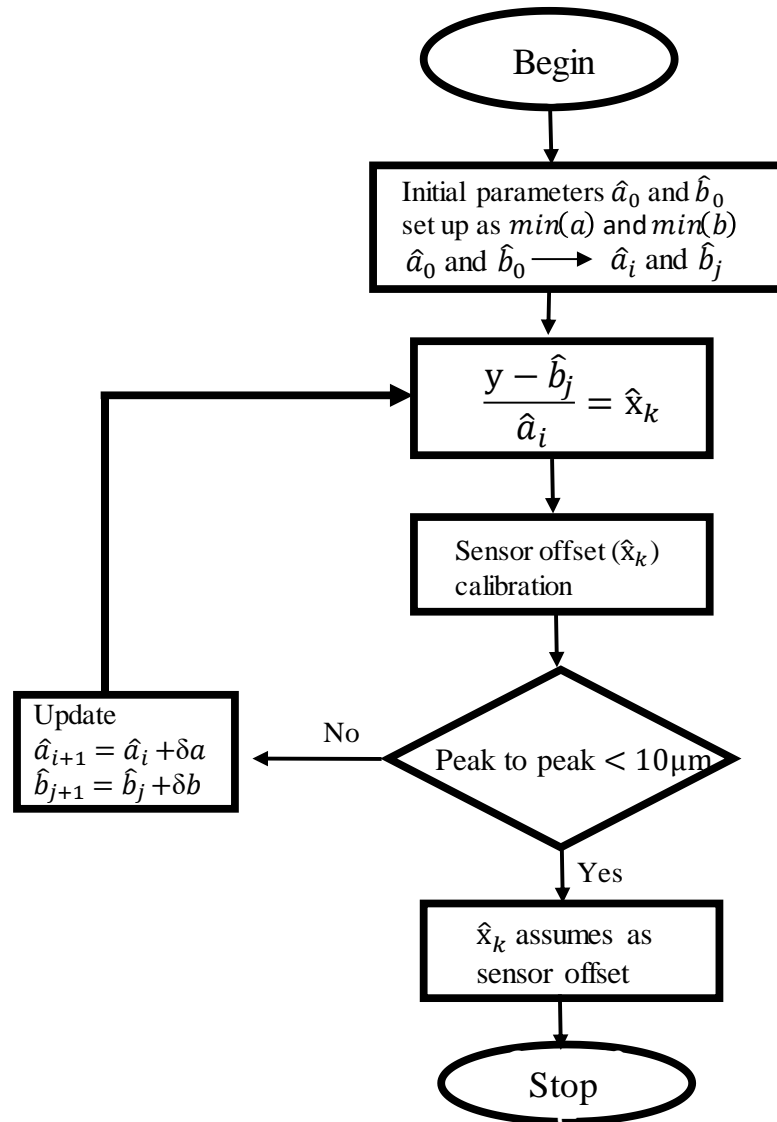


Figure 3.9. The process diagram based on the iteration method. This process is to converge to the tolerance ($10\ \mu\text{m}$) based on updating the parameters in the linear equation.

3.7 Simulation Results

After estimating sensor offsets for all gap sensors using the iteration method, the error, which is defined as the difference between peak to peak fluctuation after calibration and peak to peak fluctuation when the sensor offsets are zero, is computed to verify the iteration process. As shown in Table 3.2 and Table 3.3, we obtain the maximum error among sensors around $1.5 \mu\text{m}$. Therefore, the iteration method to estimate parameters in a linear equation is satisfied to minimize the error which is less than the tolerance ($10 \mu\text{m}$).

Table 3.2. The results of the iteration method for the gap sensor at the right side. The first and the last alignment of gap sensors has no sensor offset. Throughout the iteration method, the maximum error is around 1.2976 μm , which is less than the tolerance.

R: Right	Computed Sensor offset (μm)	Error (μm)
Sensor1R	0.0000	0.0000
Sensor2R	32.4550	0.0002
Sensor3R	14.8137	0.0023
Sensor4R	9.4475	0.0002
Sensor5R	9.1737	0.0019
Sensor6R	-31.2847	0.0038
Sensor7R	-5.2137	1.1574
Sensor8R	-38.7866	0.0010
Sensor9R	-21.7968	0.0039
Sensor10R	0.8536	1.2976
Sensor11R	-25.4230	0.0027
Sensor12R	45.2900	0.0014
Sensor13R	45.6690	0.0069
Sensor14R	13.9250	0.0043
Sensor15R	-47.8750	0.0021
Sensor16R	-8.8887	1.0080
Sensor17R	24.2610	0.0077
Sensor18R	6.5457	0.5487
Sensor19R	45.7850	0.0021
Sensor20R	0.0000	0.0000

Table 3.3. The results of the iteration method for the gap sensor at the left side. The first and the last alignment of gap sensors has no sensor offset. Throughout the iteration method, the maximum error is around $1.4663 \mu\text{m}$, which is less than the tolerance.

L: Left	Computed Sensor offset (μm)	Error (μm)
Sensor1L	0.0000	0.0000
Sensor2L	47.9730	0.0018
Sensor3L	0.3355	1.4501
Sensor4L	46.6950	0.0047
Sensor5L	-37.8960	0.0089
Sensor6L	19.6050	0.0064
Sensor7L	-9.6423	1.0830
Sensor8L	-3.0579	1.4663
Sensor9L	1.1361	1.1724
Sensor10L	-41.1750	0.0017
Sensor11L	-15.8570	0.0024
Sensor12L	-3.1851	1.4628
Sensor13L	19.0750	0.0031
Sensor14L	39.7600	0.0002
Sensor15L	24.4870	0.0011
Sensor16L	-32.3210	0.0050
Sensor17L	37.7250	0.0095
Sensor18L	33.9820	0.0027
Sensor19L	-9.1330	1.0024
Sensor20L	0.0000	0.0000

Once the iteration method is verified, we obtain airgap measurement after calibrating sensor offsets and compare it with the airgap measurement before calibrating sensor offset as shown in Figure 3.10 and Figure 3.11. The fluctuation periods of the measurements under moving conditions are around 0.4 to 5.6 sec. Compared to the fluctuations before calibrating sensor offsets, the fluctuations after calibrating sensor offsets are significantly reduced, and this will affect the pitching motion of the carrier.

From the methodology of computing the sensor offset from measurement, there is still an estimation error. Based on the results of the iteration method as seen in Table 3.2 and Table 3.3, the estimation error becomes larger as sensor offset approaches to zero. Since pitching motion of the carrier has fewer fluctuations with decreasing sensor offset, it is not accurate to find the amplitude modulation of the fluctuation with a small sensor offset in the frequency domain; it deviates from our mathematical model (a linear equation) and the iteration method. Therefore, sensor offset calibration can be implemented using accurate parameters with a smaller increment of parameter range in the mathematical model.

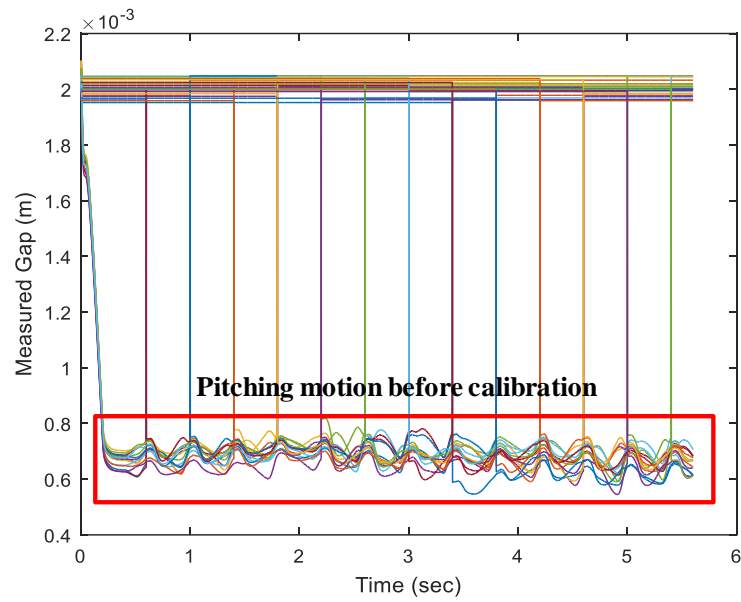


Figure 3.10. Measurements of all gap sensors before calibrating sensor offset.

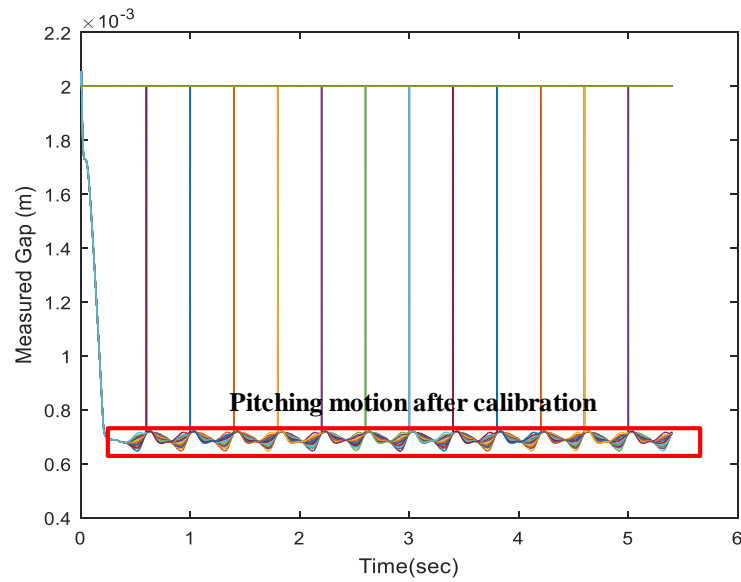


Figure 3.11. Measurements of all gap sensors after calibrating sensor offset.

4. ROLL AND PITCH CONTROLLERS DESIGN

The roll and pitch controllers aim to minimize the undesired level orientation of the carrier from load disturbances and sensor installation error. To implement the levitation control performance of the carrier, dynamic equations of roll and pitch motion are established, and controllers are designed using the optimal state-feedback controller-observer compensator. To verify the levitation control performance of the carrier, three different conditions are tested under the existence of sensor installation error and the external load disturbance [36].

4.1 Dynamic Equation of Roll Motion

In a similar approach used in section 2.2.2 for the relationship between each airgap and the center of mass (CoM), the relationship between each airgap and roll motion can be expressed as

$$\phi(t) = \frac{(\sum_{k=1}^n \Delta c_{k,r}(t) - \sum_{k=1}^n \Delta c_{k,l}(t))}{bn} \quad (4.1)$$

where, $\phi(t)$ and b are the roll motion and breadth (width) of the carrier, respectively.

According to the configuration of the carrier's roll motion as shown in Figure 4.1, the dynamic equation of roll motion is derived based on the difference between the sum of the levitation forces at each side on the carrier as

$$I_{xx}\ddot{\phi}(t) = \frac{b}{2} \cdot (\sum_{k=1}^n \Delta f_{k,l}(t) - \sum_{k=1}^n \Delta f_{k,r}(t)) + M_{\phi,d}(t) \quad (4.2)$$

where, I_{xx} is mass moment of inertia about propulsion-axis ($I_{xx} = \frac{1}{12}mb^2$) and $M_{\phi,d}(t)$ is the disturbance moment of the roll motion. Using the linearized equation of the

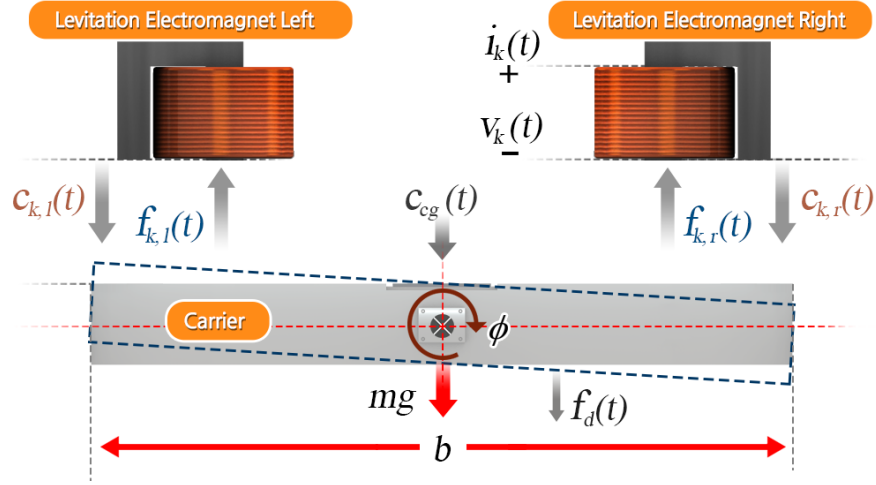


Figure 4.1. The configuration of the carrier's roll motion. The difference between the sum of the levitation forces with a small perturbation generates the roll motion of the carrier along the propulsion axis.

levitation force with a small perturbation approach, the dynamic roll motion without disturbance moment is re-written as

$$I_{xx}\ddot{\phi}(t) = \frac{b}{2}[K_c \cdot (\sum_{k=1}^n \Delta c_{k,l}(t) - \sum_{k=1}^n \Delta c_{k,r}(t)) - K_i \cdot (\sum_{k=1}^n \Delta i_{k,l}(t) - \sum_{k=1}^n \Delta i_{k,r}(t))] \quad (4.3)$$

4.2 Dynamic Equation of Pitch Motion

To determine the pitch motion of the carrier and establish its dynamic equation, it is necessary to consider the influential zone of the levitation electromagnets. Since the levitation electromagnets are discontinuously installed on the upper frame, pitching motion of the carrier occurs as it moves along the propulsion axis; specifically, this pitching motion fluctuates rapidly as the carrier moves from one's influential zone to the next of the levitation electromagnet. The analysis of the carrier's motion along the propulsion-axis is as shown in Figure 4.2. In the first stage of the magnetic levitation transport system, it is assumed to be stable since the turning effect of the levitation

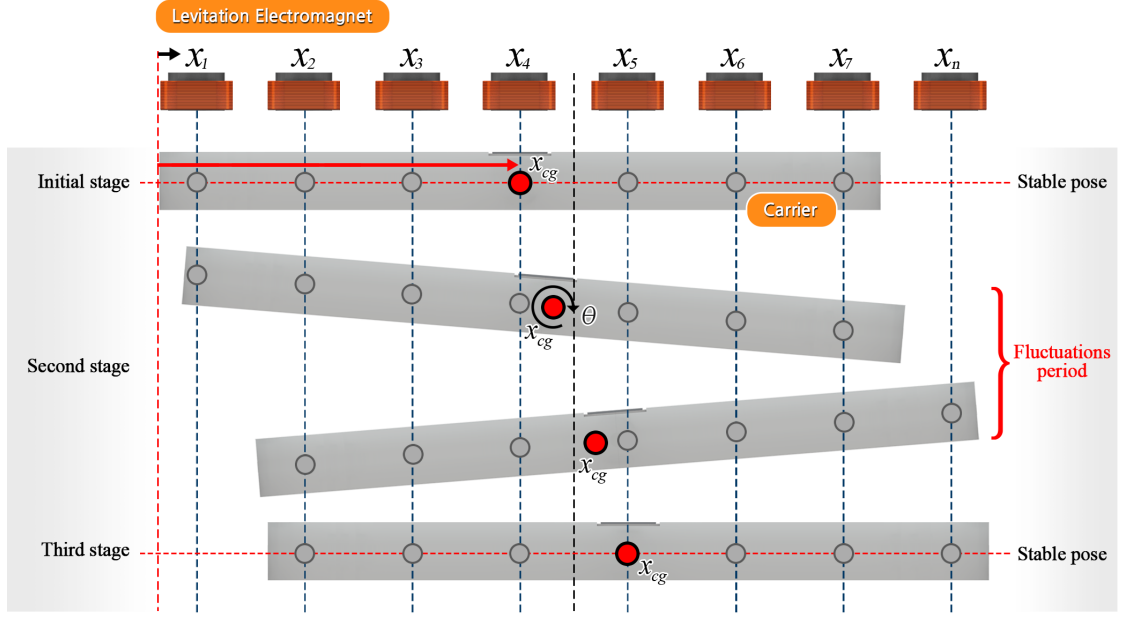


Figure 4.2. The configuration of the carrier's pitch motion. The carrier has a stable pose at the first stage. As the carrier moves to the next influential zone of the levitation electromagnet at the second stage, fluctuations inevitably occur. The carrier has a stable pose again as the moment of levitation forces at each side is balanced.

forces on one side at the center of mass balances the turning effect of the forces on the other side at the center of mass. As the carrier moves to the next influential zone of the levitation electromagnet, the zones where the levitation forces exert on the carrier change. That is, the moment of levitation forces on each side at the CoM becomes unbalanced so that a pitching motion can occur on the second stage. Once the carrier moves completely to the next zone on the third stage, the moment of levitation forces at each side is balanced again. The motion of the carrier repeats this process until it stops at the last influential zone of the levitation electromagnet.

Based on the analysis of pitch motion of the carrier, dynamic equation of pitch motion

can be derived in terms of levitation forces and influential zone of the levitation electromagnets as

$$I_{yy}\ddot{\theta} = \sum_{k=1}^n (x_k(t) - x_{cg}(t)) \cdot \Delta f_{k,r,l}(t) + M_{\theta,d}(t) \quad (4.4)$$

where, $\theta(t)$ is the pitch motion, I_{yy} is the mass moment of inertia about lateral-axis ($I_{yy} = \frac{1}{12}ml^2$), l is the length of the carrier, $x_k(t)$ is the influential zone of activated-levitation electromagnets, $x_{cg}(t)$ is the location of the carrier at CoM along the propulsion axis, and $M_{\theta,d}(t)$ is the disturbance moment of pitch motion. $(x_k(t) - x_{cg}(t))$ is defined as $\Delta x_k(t)$ for convenience. Using a linearized levitation force equation, dynamic equation of pitching motion is re-written without a disturbance moment as follows

$$I_{yy}\ddot{\theta}(t) = K_c \cdot \sum_{k=1}^n \Delta x_k(t) \cdot \Delta c_{k,r,l}(t) - K_i \cdot \sum_{k=1}^n \Delta x_k(t) \cdot \Delta i_{k,r,l}(t) \quad (4.5)$$

In a similar way to the relationship between each airgap and roll motion from equation 4.1, the proposed mathematical approximation between the pitch angle and airgaps with the zones of activate-levitation electromagnets is formulated as

$$\tan(\theta(t)) \simeq \theta(t) = \frac{c_{k,l}(t) - c_{cg}(t)}{x_{k,l}(t) - x_{cg}(t)} = \frac{c_{k,r}(t) - c_{cg}(t)}{x_{k,r}(t) - x_{cg}(t)} \simeq \frac{(kl/n) \sin(\theta(t))}{(kl/n) \cos(\theta(t))} \simeq \frac{(kl/n)\theta(t)}{(kl/n)} \quad (4.6)$$

4.3 State Space Representation of Linear Time Invariant System

The levitation controller was designed utilizing the cascade control strategy, and its robustness and stability were verified based on the analysis of frequency response and the Nyquist criterion of the system in section 2. Hence, to minimize the roll and pitch motion of the carrier and to improve the levitation control performance, a state space model for a linear time-invariant (LTI) system is developed. Applying the airgap relationships from equation 4.1 and 4.6 into dynamic equations to the

roll and pitch motions, the following state space representation is developed. The dynamic equations of the roll and pitch motion using the airgap relationship ($n = 7$) are re-written as

$$I_{xx}\ddot{\phi}(t) = \frac{b}{2}[-7K_cb\phi - K_i(\sum_{k=1}^7 \Delta i_{k,l} - \sum_{k=1}^7 \Delta i_{k,r})] \quad (4.7)$$

$$I_{yy}\ddot{\theta}(t) = \frac{20}{7}K_cl^2\theta - \frac{1}{7}K_il \cdot \sum_{k=1}^7 k \cdot \Delta i_{k,r,l} \quad (4.8)$$

Having equations 4.7 and 4.8, state space representation for the roll and pitch is expressed as

$$\begin{aligned} \dot{x}(t) &= Ax(t) + Bu(t) \\ y(t) &= Cx(t) + Du(t) \\ x(0) &= x_0 \end{aligned} \quad (4.9)$$

where,

$$\begin{aligned} A &= \begin{pmatrix} 0 & 1 & 0 & 0 \\ \frac{-7K_cb^2}{2I_{xx}} & 0 & 0 & 0 \\ 0 & 0 & 0 & 1 \\ 0 & 0 & \frac{20K_cl^2}{7I_{yy}} & 0 \end{pmatrix} B = \begin{pmatrix} 0 & 0 \\ -\frac{K_ib}{2I_{xx}} & 0 \\ 0 & 0 \\ 0 & -\frac{K_il}{7I_{yy}} \end{pmatrix} \\ C &= \begin{pmatrix} 1 & 0 & 0 & 0 \\ 0 & 0 & 1 & 0 \end{pmatrix} D = \begin{pmatrix} 0 & 0 \\ 0 & 0 \end{pmatrix}. \end{aligned} \quad (4.10)$$

$$x = \begin{pmatrix} \phi(t) \\ \dot{\phi}(t) \\ \theta(t) \\ \dot{\theta}(t) \end{pmatrix} u = \begin{pmatrix} \sum_{k=1}^7 \Delta i_{k,l} - \sum_{k=1}^7 \Delta i_{k,r} \\ \sum_{k=1}^7 k \cdot \Delta i_{k,r,l} \end{pmatrix} y = \begin{pmatrix} \phi(t) \\ \theta(t) \end{pmatrix}.$$

Having a full rank of $[B \ AB \dots A^{n-1}B]$ and $[C \ CA \dots CA^{n-1}]^T$, the system is controllable and observable.

4.4 Optimal State-Feedback Controller-Observer Compensator

An optimal state feedback controller using a linear quadratic regulator (LQR) approach to find a control law for the system to meet optimal criteria can be achieved [37]; the appropriate Lyapunov function ($V = x^T Px$) is used to minimize the equation as follows

$$f(u) = \frac{dV}{dt} + x^T Qx + u^T Ru \quad (4.11)$$

$$\frac{\delta}{\delta u} f(u) = 0^T, u = u^* \quad (4.12)$$

where Q and R are symmetric positive semi-definite (P.S.D) and positive definite (P.D), respectively. The optimal control law is generalized as

$$u^* = -R^{-1}B^T Px = -K_o x \quad (4.13)$$

where K_o is optimal controller gain. Applying K_o into $f(u)$, Algebraic Riccati Equation (ARE) can be derived find appropriate P as

$$A^T P + PA + Q - PBR^{-1}B^T P = 0 \quad (4.14)$$

The synthesis of K_o and $f(u)$ then minimizes the performance index, $J = \int_0^\infty (x^T Qx + u^T Ru)dt$. To select R and Q matrices in our case, $Q = C' * C$ and $R = 0.00001I_2$ to minimize the risk of a large control effort and output error. To check the stability of the system, eigenvalues of $(A - BK_o)$ are negative real parts so that state feedback system with a synthesis of the optimal controller is asymptotically stable.

In the magnetic levitation transport system, there are no sensors to measure the rotational motion so the roll and pitching motions of the carrier cannot be measured. Therefore, an observer design is proposed to estimate roll and pitch motion, and it

provides the state estimate to control the rotational movement of the system. The observer dynamic is written as

$$\begin{aligned}\dot{\tilde{x}}(t) &= A\tilde{x}(t) + Bu + L(y(t) - \tilde{y}(t)) \\ y &= Cx(t) \\ \tilde{x}(0) &= \tilde{x}_0\end{aligned}\tag{4.15}$$

where, \tilde{x}, \tilde{y} and L are state estimate, output estimate and observer gain matrix, respectively. The observer gain matrix L is selected such that the error, $e = x - \tilde{x}$, is asymptotically stable. The error equation, $\dot{e} = (A - LC)e$, is the difference between estimate state and actual state variables with any arbitrary initial error to zero. In our case, the observer poles are chosen to be a factor of 3 times faster than the optimal controller poles. Based on the observer poles, the observer gain matrix L can be obtained.

Having an optimal controller and observer design, a combined optimal state-feedback controller-observer compensator is designed, and the control block diagram for roll and pitch motion is shown in Figure 4.3.

By applying a control law $u = -K_o\tilde{x}(t) + v(t)$ into the closed-loop system, state space representation can be written as

$$\begin{aligned}\begin{bmatrix} \dot{x} \\ \dot{\tilde{x}} \end{bmatrix} &= \begin{bmatrix} A & -BK_o \\ LC & A - LC - BK_o \end{bmatrix} \begin{bmatrix} x(t) \\ \tilde{x}(t) \end{bmatrix} + \begin{bmatrix} B \\ B \end{bmatrix} v(t) \\ y &= \begin{bmatrix} C & 0 \end{bmatrix} \begin{bmatrix} x(t) \\ \tilde{x}(t) \end{bmatrix}\end{aligned}\tag{4.16}$$

where, $v(t)$ is external input and is denoted as $v(t) = [\phi_{ref} \ \theta_{ref}]^T = 0$. Having the transformation matrix Q_t , the closed-loop system can be re-expressed as

$$\begin{aligned} \begin{bmatrix} \dot{x}(t) \\ \dot{e}(t) \end{bmatrix} &= \begin{bmatrix} A - BK_o & -BK_o \\ O & A - LC \end{bmatrix} \begin{bmatrix} x(t) \\ e(t) \end{bmatrix} + \begin{bmatrix} B \\ O \end{bmatrix} v(t) \\ y &= \begin{bmatrix} C & 0 \end{bmatrix} \begin{bmatrix} x(t) \\ e(t) \end{bmatrix} \end{aligned} \quad (4.17)$$

where, $e = \tilde{x}(t) - x(t)$. The poles of the closed-loop system include individual eigenvalues of $A - BK_o$ and $A - LC$ so that the control law does not affect the observer (separation principle). Therefore, the closed-loop transfer function of the combined controller-observer is the same as that of the actual control law. Based on the stability test with the optimal control law, the system with a combined optimal state feedback controller-observer compensator is asymptotically stable. For security rea-

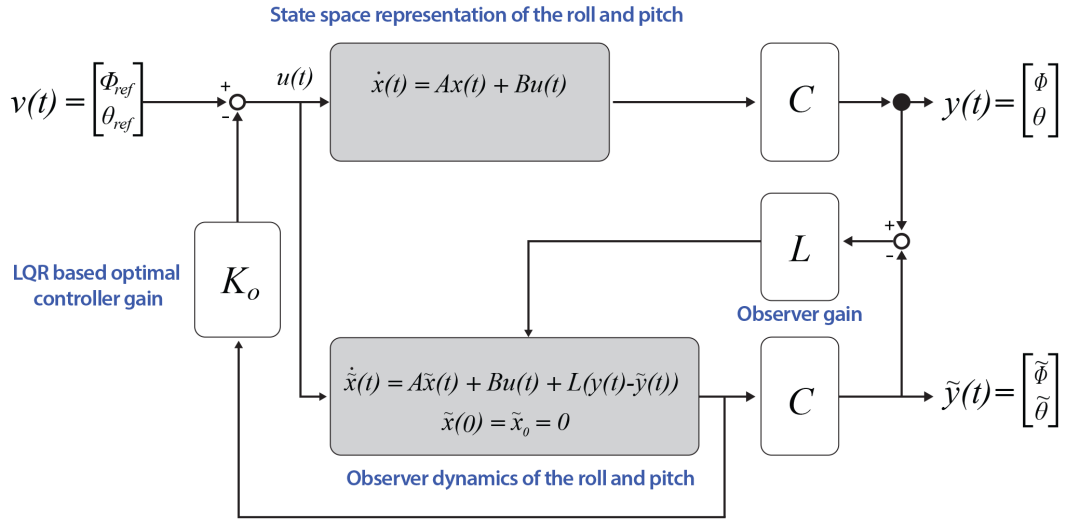


Figure 4.3. The control block diagram for roll and pitch feedback loop. Having a state space representation of roll and pitch motion, the outputs are obtained. The observer gain (L) helps to estimate the state variables and to approach the actual state variables. The optimal controller gain (K_o) helps to minimize undesired deviations of the roll and pitch motion.

sons (Non-Disclosure Agreement), please be understood that control variables and parameters such as the number of coil turns, the cross-sectional area of the levitation electromagnet, the mass of the carrier, total resistance, etc. are veiled.

4.5 Simulation Results

In this section, the simulation results using the proposed control strategies are presented. Three tests are set up to verify the robustness and stability of the levitation control performance using MATLAB/SIMULINK. Moreover, the performance of our proposed controllers is compared to that of the levitation controller only. For simplicity, each controller is defined as

K1: The levitation controller which consists of current (PI) and airgap controllers (PID). This controller was designed using a cascade control strategy based on the dynamic analysis of a single mass system.

K2: In addition to the levitation controller, combined optimal controller (LQR)-observer compensator is added to the control strategy. These controllers are designed based on the dynamic analysis of the 3-dimensional system.

To illustrate the effectiveness of the roll and pitch control strategy, the following tests are performed based on the desired maximum velocity (500 mm/s) as shown in Figure 4.4.

Test 1: The first test is the ideal case which has no installation error in the gap sensors so that the airgap measurement can be obtained precisely. Moreover, a load disturbance is neglected as well.

Test 2: To test roll and pitch controllers performance in a more realistic situation, random variation of sensor installation with an error range of $-50 \mu m$ to $50 \mu m$ is added.

Test 3: To verify robustness of levitation control performance in our system, external load disturbance, $M_d = 3000Nm$ (from 2 to 3 sec) is added at the center of mass of the carrier with sensor installation error.

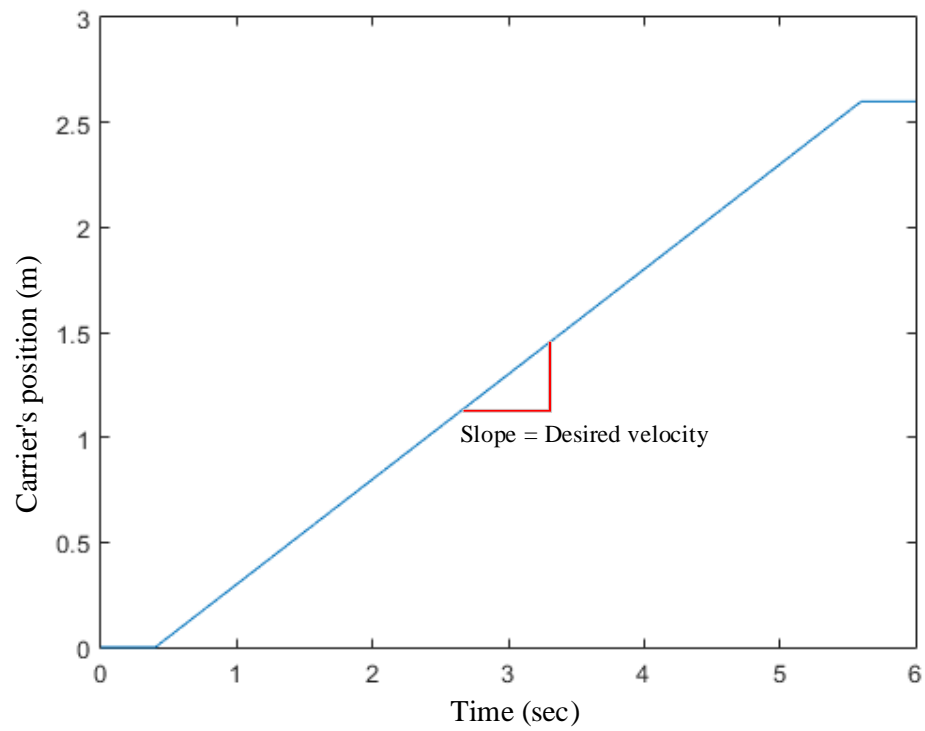


Figure 4.4. Desire velocity profile of the magnetic levitation transport system. The slope indicates 500 mm/s velocity of the system.

4.5.1 Test 1: Ideal Case

For **Test 1**, the roll and pitch motion trajectories are shown in Figure 4.5. As seen in Figure 4.5, there is no observed roll motion in the ideal condition so that it is enough to use **K1** for the control roll angle. Pitch motion trajectories are obtained when the carrier moves to the next influential zone of the levitation electromagnet.

As seen in the comparison between pitch angle with **K1** and **K2** in Table 4.1, it becomes slightly attenuated as the carrier moves along the propulsion axis.

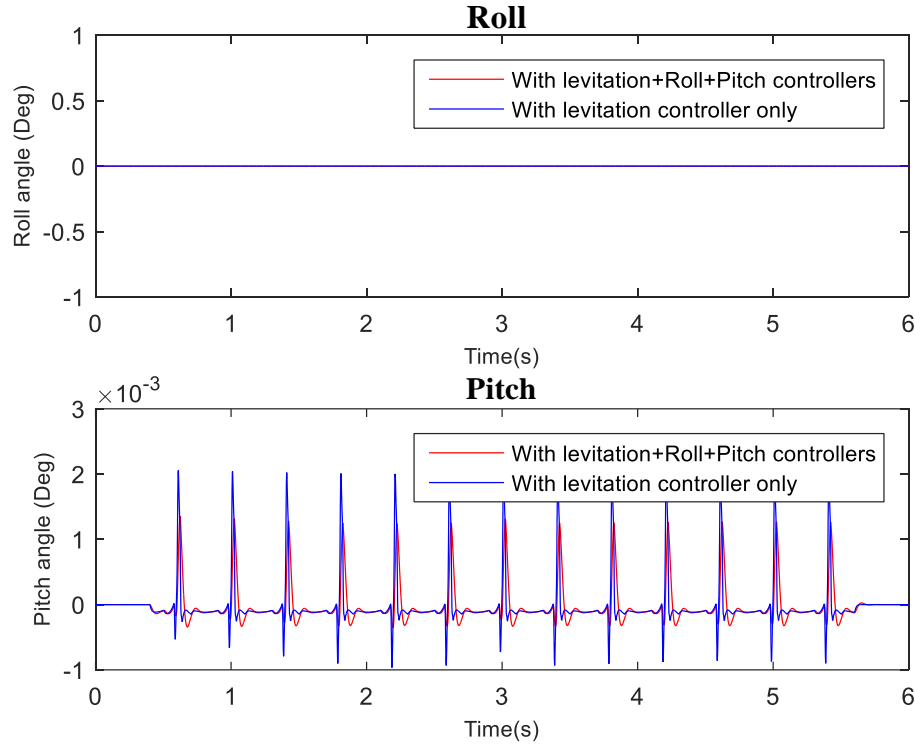


Figure 4.5. Roll and pitch motion trajectories in **Test 1**. The red line represents the roll and pitch angle with the levitation, roll and pitch controllers. The blue line represents the roll and pitch angle with the levitation controller only.

Table 4.1. The results for pitch angle in **Test 1**. The maximum and minimum attenuation of pitch angles are $0.7 * 10^{-3}$ deg and $0.61 * 10^{-3}$ deg, respectively.

-	Max ($*10^{-3}$ deg)	Min ($*10^{-3}$ deg)	Avg ($*10^{-3}$ deg)
Pitch with K1	2.100	-0.960	-0.023
Pitch with K2	1.400	-0.350	-0.019
Attenuation	0.700	0.610	0.004

The airgap measurements of each gap sensor are shown in Figure 4.6. As seen from Figure 4.6, each line represents the airgap measurement from each gap sensor. In non-levitation and stop state, the vertical displacement between the carrier and sen-

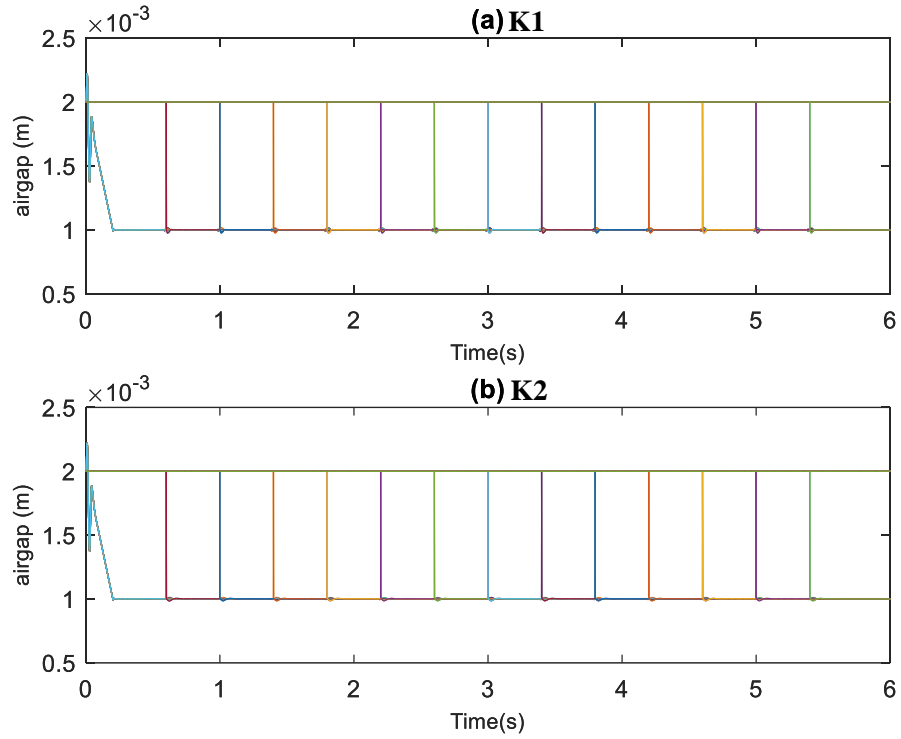


Figure 4.6. Airgap measurement from each sensor in **Test 1**: (a) airgap measurement with **K1** and (b) airgap measurement with **K2**. There are 13 switching patterns between each gap sensor during the entire process.

sor is 2 mm, and levitation displacement is designed as 1 mm while in operation. In the range of 0 to 0.4 sec, the carrier starts to levitate. During the initial period of the carrier translation from 0.4 to 5.6 sec at desired velocity (500 mm/s), 7 gap sensors on the right and left sides are activated at the same time. When the carrier moves to the next influential zone of sensors, the first zone of sensors are deactivated. Therefore, there are 13 switching patterns between adjacent sensors during the entire process. As seen from Figure 4.7, **K2** clearly shows that fluctuating airgaps are attenuated compared to **K1**.

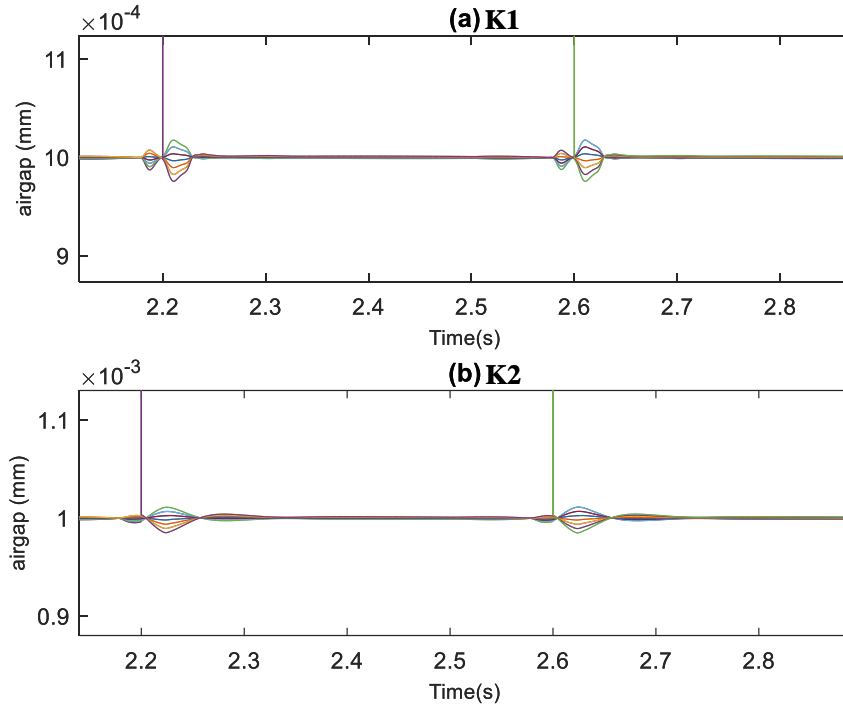


Figure 4.7. Zoom-in view of airgap measurement in **Test 1**: (a) airgap measurement with **K1** and (b) airgap measurement with **K2**. The fluctuations of the airgap measurement is a slightly attenuated with **K2** around 2.2 seconds and 2.6 seconds.

4.5.2 Test 2: Existence of Sensor Installation Error

In **Test 2**, both roll and pitch motion are tested, and an unbalanced carrier can be generated owing to a sensor installation error in the range of $-50\ \mu\text{m}$ to $50\ \mu\text{m}$. Other external load disturbances are not considered in this section.

As seen in Figure 4.8, red lines represent the measurement of roll and pitch angles with the proposed levitation, roll and pitch controllers based on the dynamic analysis of the 3-dimensional system and blue lines represent the measurement of roll and pitch angles with the levitation controller only based on the dynamic analysis of the single mass system. It is noticed that the fluctuations of both roll and pitch with **K2** are reduced compared to those with **K1**. The numerical results for roll and pitch

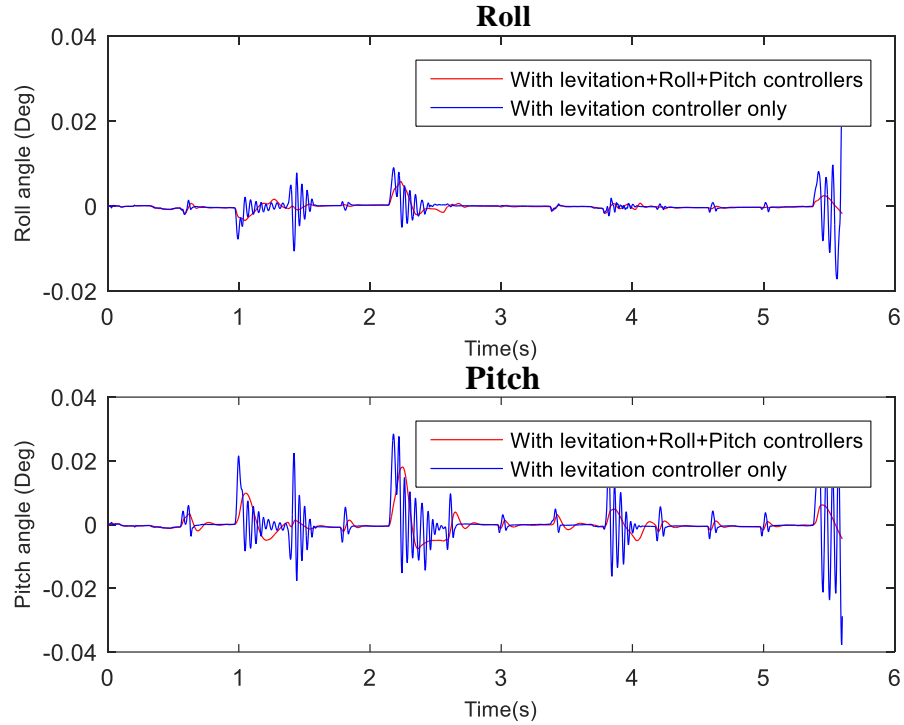


Figure 4.8. Roll and pitch motion trajectories in **Test 2**. The red line is the roll and pitch angle with the levitation, roll and pitch controller and the blue line is the roll and pitch angle with the levitation controller only.

Table 4.2. The results for roll and pitch angle in **Test 2**. The maximum and minimum attenuation of the roll angles are $18.2 * 10^{-3}$ deg and $13.8 * 10^{-3}$ deg, respectively. The maximum and minimum attenuation of the pitch angles are $10.3 * 10^{-3}$ deg and $30.1 * 10^{-3}$ deg, respectively.

-	Max (* 10^{-3} deg)	Min (* 10^{-3} deg)	Avg (* 10^{-3} deg)
Roll with K1	24.000	-17.200	-0.087
Roll with K2	5.800	-3.400	-0.083
Attenuation for roll	18.200	13.800	0.004
Pitch with K1	28.400	-37.700	0.059
Pitch with K2	18.100	-7.600	0.023
Attenuation for pitch	10.300	30.100	0.036

angle are seen in Table 4.2. As seen in Figure 4.9 and Figure 4.10, maximum and minimum fluctuation of airgap measurement with **K1** are about 1.6×10^{-3} m and 0.6×10^{-3} m, respectively. Using the proposed control strategies (**K2**), maximum and minimum fluctuation of airgap measurement are attenuated to about 1.2×10^{-3} m and 0.8×10^{-3} m, respectively.

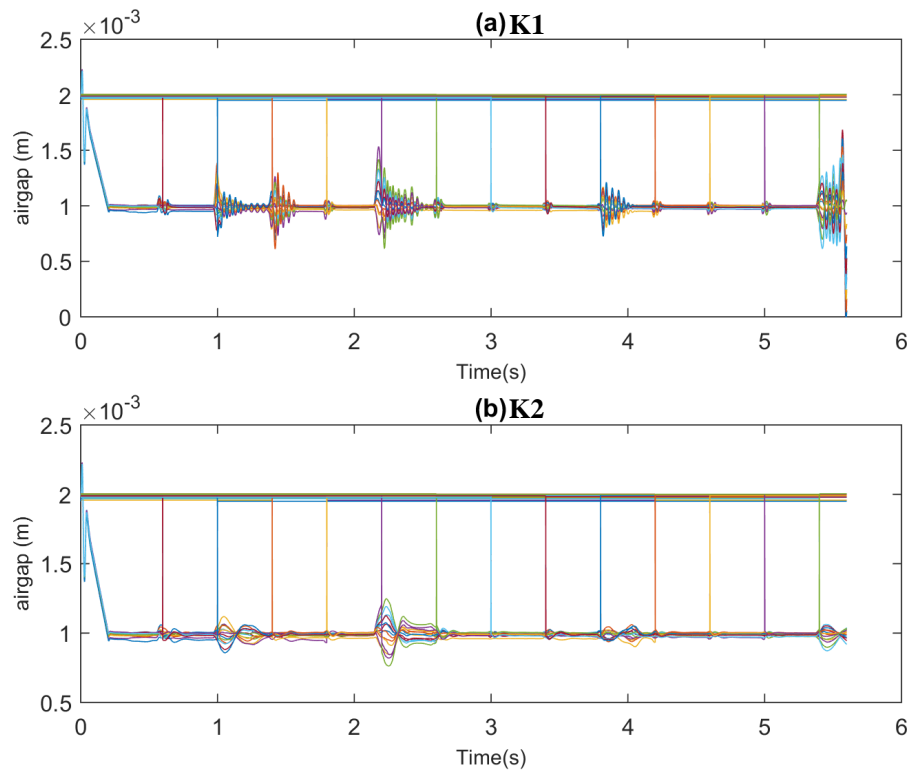


Figure 4.9. Airgap measurement from each sensor in **Test 2**: (a) airgap measurement with **K1** and (b) airgap measurement with **K2**.

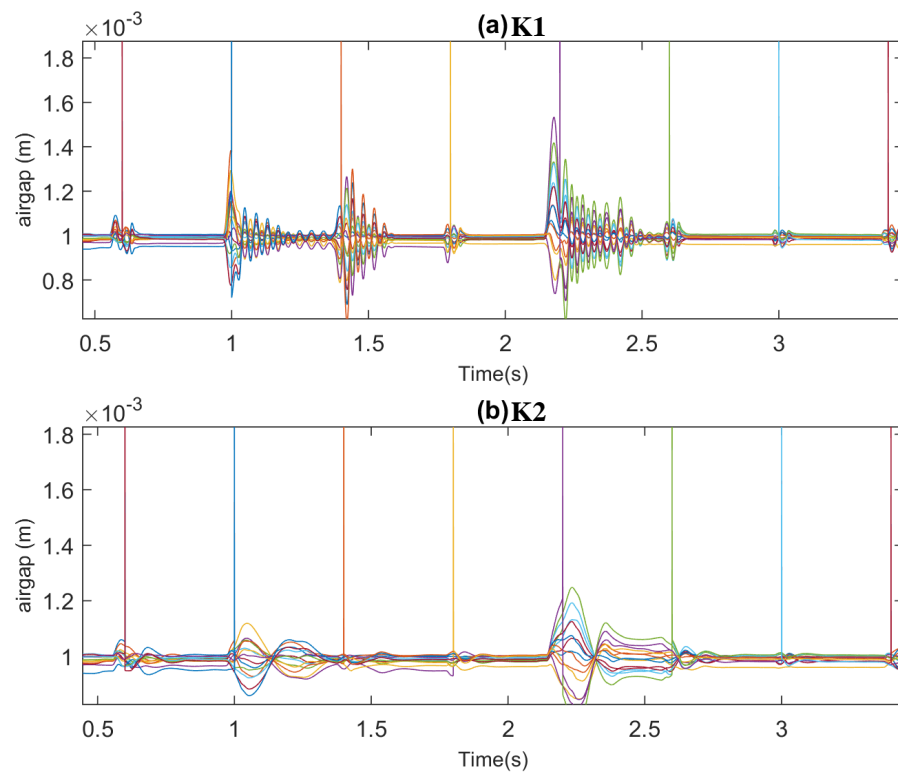


Figure 4.10. Zoom-in view of airgap measurement in **Test 2**: (a) airgap measurement with **K1** and (b) airgap measurement with **K2**.

4.5.3 Test 3: Existence of Sensor Installation Error and External Load Disturbance

The results of **Test 3** are presented to show the stability and robustness of levitation performance under external load disturbance and sensor installation error with a period of 1 sec (from 2 to 3 sec).

As seen in Figure 4.11, roll and pitch angle trajectories with **K1** rapidly fluctuate so that the magnetic levitation transport system has a poor levitation control performance. Using the controller **K2** shows the fluctuations of the roll and pitching

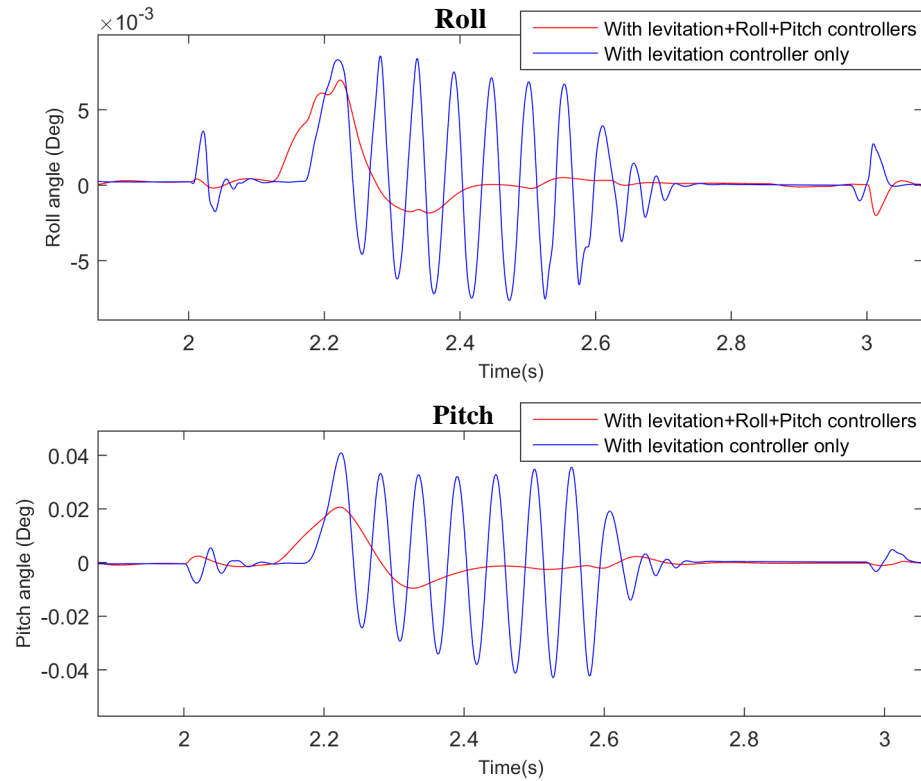


Figure 4.11. Roll and pitch motion trajectories from 2 to 3 sec in **Test 3**. The red line indicates the roll and pitch angle with the levitation, roll and pitch controllers. The blue line indicates the roll and pitch angle with the levitation controller only.

Table 4.3. The results for roll and pitch angle in **Test 3**. The maximum and minimum attenuation of the roll angles are 1.9×10^{-3} deg and 10.9×10^{-3} deg, respectively. The maximum and minimum attenuation of the pitch angles are 20.2×10^{-3} deg and 0.033×10^{-3} deg, respectively.

-	Max ($\times 10^{-3}$ deg)	Min ($\times 10^{-3}$ deg)	Avg ($\times 10^{-3}$ deg)
Roll with K1	8.900	-14.300	-0.171
Roll with K2	7.000	-3.400	-0.058
Attenuation for roll	1.900	10.900	0.113
Pitch with K1	40.900	-0.043	0.095
Pitch with K2	20.700	-0.010	0.073
Attenuation for pitch	20.200	0.033	0.022

motions are significantly reduced, and the rotational movement of the carrier can be stabilized. The numerical result of roll and pitch angles in **Test 3** is described in Table 4.3.

As seen from Figure 4.12, about 14 fluctuations of airgap measurement with **K1** occur from 2.2 to 2.7 sec. The maximum and minimum airgap measurement are about 1.5×10^{-3} m and approximately 0.5×10^{-3} m, respectively. Compared to these with **K1**, the fluctuations of airgap measurement with **K2** are significantly attenuated, and its maximum and minimum values are reduced as about 1.3×10^{-3} m and about 0.6×10^{-3} m, respectively.

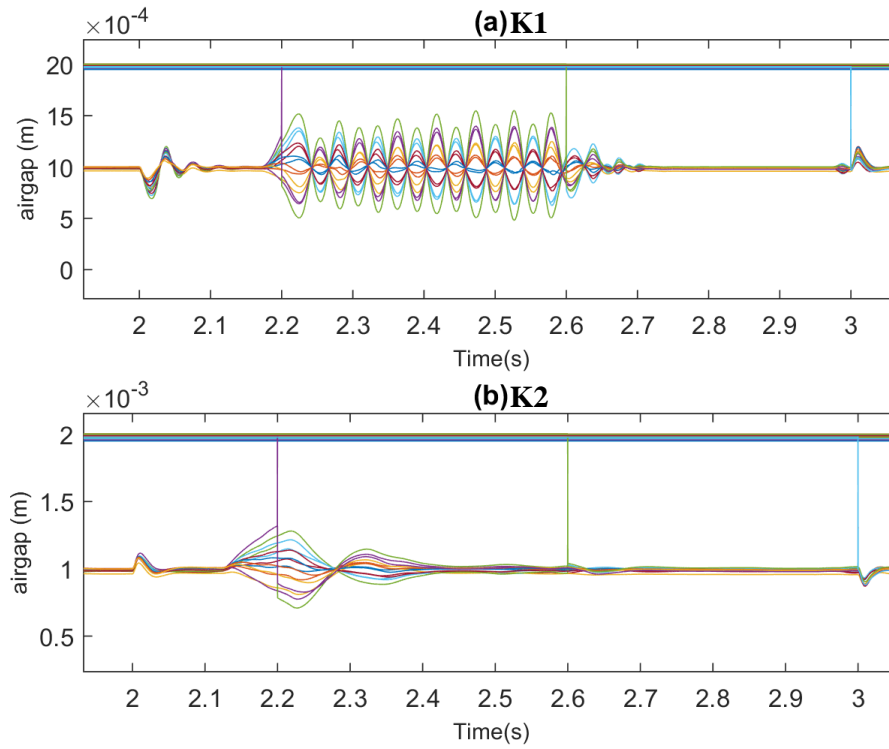


Figure 4.12. Airgap measurement of each sensor from 2 to 3 sec in **Test 3**: (a) airgap measurement with **K1** and (b) airgap measurement with **K2**. There are around 14 fluctuations of the airgap measurement with **K1** that occur from 2.2 to 2.7 sec and these fluctuations are significantly attenuated with **K2**.

Figure 4.13 shows the current signals applied to the magnetic levitation transport system with **K2** in **Test 3**. The magnitude of the initial current signal is around 5 A because a large amount of energy is necessary to levitate the carrier. Around 2 A of each current signal is used to stabilize the levitation control performance under sensor installation error. From 2 to 3 sec, the magnitude of the current signal increases up to 3 A for stabilizing the levitation state under sensor installation error and external load disturbance. It is shown that the amount of energy for stabilizing the levitation state owing to various conditions is less than that of maximum energy (5 A).

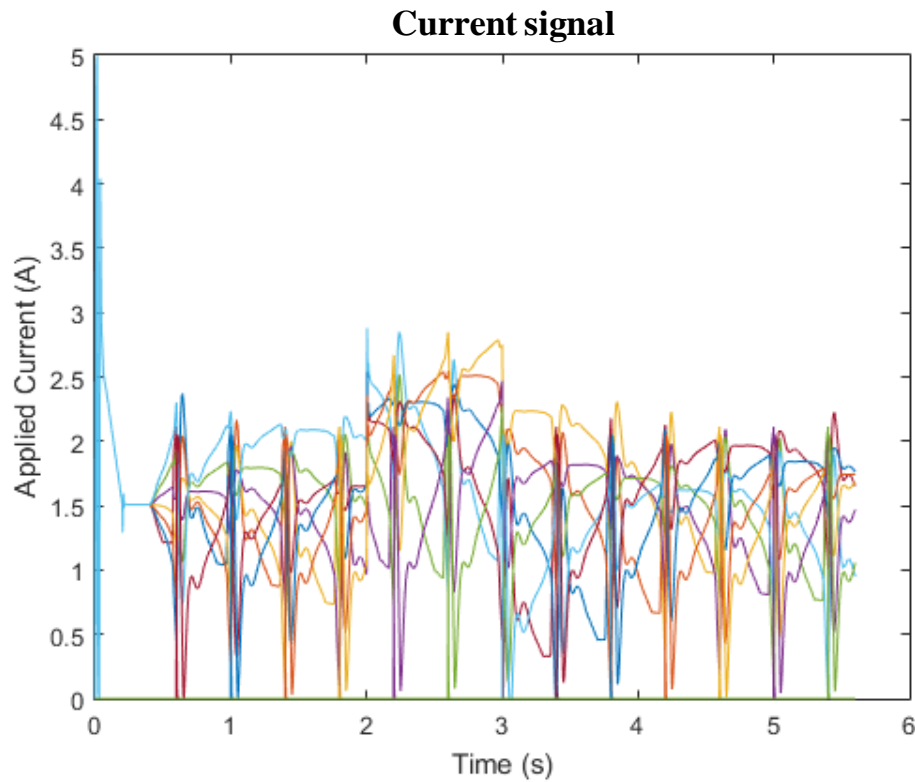


Figure 4.13. The current signals with **K2** in **Test 3**. The initial current signal is around 5 A to levitate the carrier. Around 2 A of the current signals are used to stabilize the levitation control performance under sensor installation error. From 2 to 3 sec, around 3 A of the current signals are used to stabilize the levitation state under sensor installation error and external load disturbance.

From the results of **Test 3**, the combined levitation, roll and pitch controllers proved the excellent control performance under a large load disturbance and randomly distributed sensor installation error. All three tests demonstrate that our proposed controllers can significantly attenuate roll and pitch motion of the carrier for both stability and robustness of the levitation control performance under harsh conditions.

5. SECTION CONTROL ALGORITHM

In our magnetic levitation transport system, the number of activated levitation electromagnets is determined by the position of the carrier. Owing to the fluctuation of the carrier as it moves to the next influential zone, levitation forces should be smoothly generated or dissipated in the range of the lateral gap between each levitation electromagnet. Therefore, a section control algorithm is proposed to minimize the sudden change of the levitation forces as the carrier moves to the next influential zone [38,39]. To establish the mathematical strategies of the section control algorithm, some specifications should be satisfied as follows:

- 1) The levitation forces are generated based on the position of the carrier.
- 2) The levitation forces, which exert on the edge of the carrier, are decreasing as the carrier moves along the propulsion axis.
- 3) The sum of the levitation forces exerted by activated levitation electromagnets is equal to the weight of the carrier.
- 4) The sum of the moment along the propulsion axis is equal to zero.

Based on the above specifications, the levitation forces exerted by activated levitation electromagnets are described in Figure 5.1. The section control algorithm is derived based on the number of activated levitation electromagnets (N_a), the number of the levitation electromagnets in the switching zone (N_s) and the number of effective levitation electromagnets (N_e). These variables are defined as

$$N_a = \frac{L}{D} \tag{5.1}$$

$$N_s = 2S, \quad 1 \leq S \leq \frac{N_a}{2} \tag{5.2}$$

$$N_e = N_a - \frac{N_s}{2} \quad (5.3)$$

where D ($= 200$ mm) is the length of each levitation electromagnet and S is an integer value, respectively. In our system, the carrier has a good levitation control performance to support the carrier when $S=1$. Satisfying equation (5.1), (5.2), and (5.3), the levitation force for each levitation electromagnets ($f_{k,r,l}$) is as follows.

$$f_{k,r,l} = \begin{cases} \frac{mg}{2N_e} & \text{if } |\Delta x_k| \leq r \\ \frac{mg}{2N_e} \left(\frac{N_a D/2 - |\Delta x_k|}{N_s D/2} \right) & \text{if } r < |\Delta x_k| \leq \frac{N_a D}{2} \\ 0 & \text{else} \end{cases} \quad (5.4)$$

where Δx_k is the difference between influential zone of the levitation electromagnet (x_k) and the position of the carrier at the CoM (x_{cg}) and $r = (N_a - N_s)D/2$.

With the specific values for $N_a = 7$, $N_s = 2$ and $N_e = 6$ in our case, the levitation forces exert about $mg/12$ when $|\Delta x_k|$ is less than or equal to 500 mm.

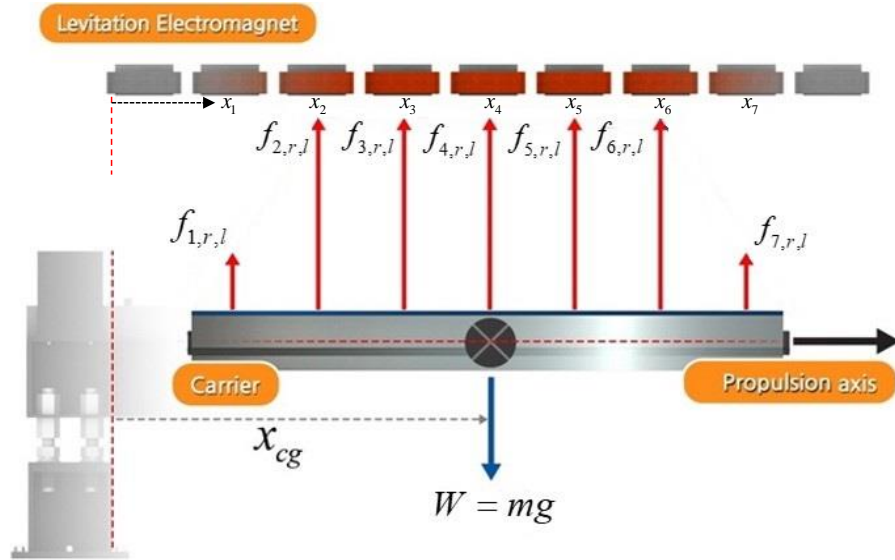


Figure 5.1. Schematic diagram of the section control algorithm based on the position of the carrier.

For the range of $500 \text{ mm} < |\Delta x_k| \leq 700 \text{ mm}$, the levitation forces can generate between 0 to $mg/24$ with slope of $mg/2.4$. Therefore, it is satisfied with the given criteria such that sum of the levitation forces are same as the weight of carrier ($2 \sum_{k=1}^n f_{k,r,l} = mg$) and it is balanced at center of mass; sum of moment is zero ($2 \sum_{k=1}^n \Delta x_k f_{k,r,l} = 0$).

According to the simulation result as shown in Figure 5.2, the difference between the weight of the carrier and the sum of the levitation forces exerted by activated levitation electromagnets is close to zero. Moreover, the sum of the moments is close to zero along the propulsion axis. Therefore, the section control algorithm is verified to minimize the fluctuations of the carrier as it moves to the next influential zone.

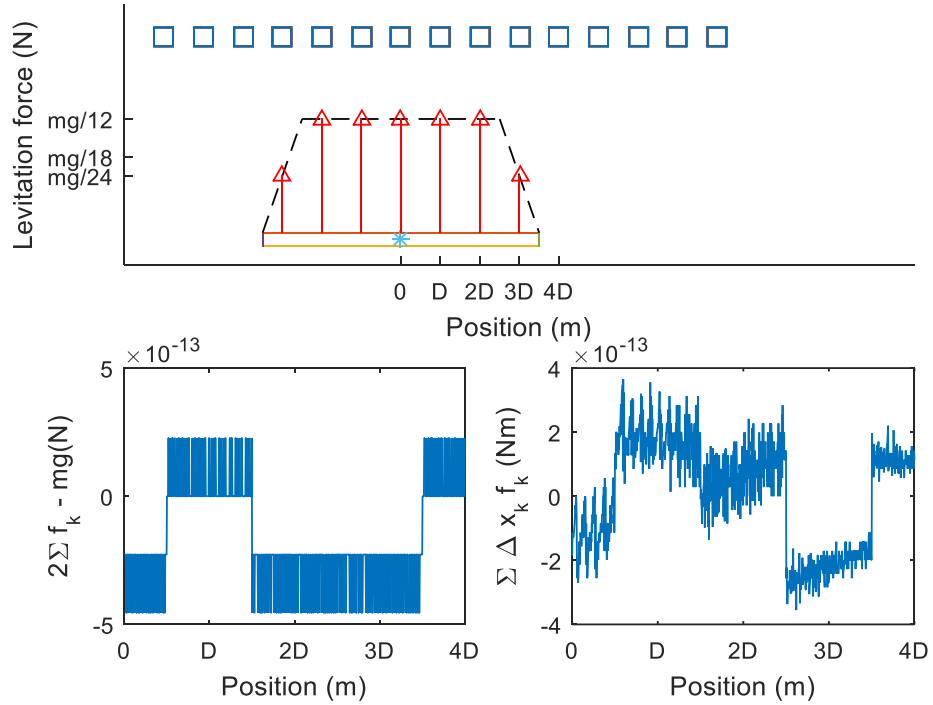


Figure 5.2. Simulation result of sum of the levitation forces and sum of the moment using section control algorithms.

6. EXPERIMENTAL VERIFICATION

6.1 Experimental Setup

The manipulation of a high precision magnetic levitation transport system is verified in the following experimental setup. As shown in Figure 6.1, the Real-Time Interface (RTI) in dSPACE is used to control the airgap of the carrier. The dSPACE controller board is suitable for a high precision control as it has a flexible implementation using the MATLAB/Simulink blocks. Moreover, data acquisition and monitoring in real-time can be done. For the current controller, it utilizes Junus (JSP-180-10 of Copley Controls) units which modulate the applied current based on a reference current (command) from the DS1104 R&D controller board (Simulator Full-Size of dSPACE). The applied voltage for the levitation electromagnets (150 V) is supplied through the Junus units. Each levitation electromagnet is connected to each current amplifier which uses the same control gains from the PI controller for all Junus units. The reference commands, which are desired applied currents from dSPACE, are output through isolated differential amplifiers. These outputs from the isolated differential amplifiers flow into each current amplifier. Therefore, applied current for each levitation electromagnet is assumed to be the same value for all, and thus one DS1104 controller board is used to control the airgap. In our system, there are a power line (high voltage level), a control signal line (low and precise voltage level) and a communication line (digital signal level). Isolated differential amplifier boards are developed to separate the ground for power line and control signal line so that it is expected to minimize the noise from the control signal line and a common mode noise from the induction of magnetic field. The isolated differential amplifier boards are connected between dSPACE and the Junus units.

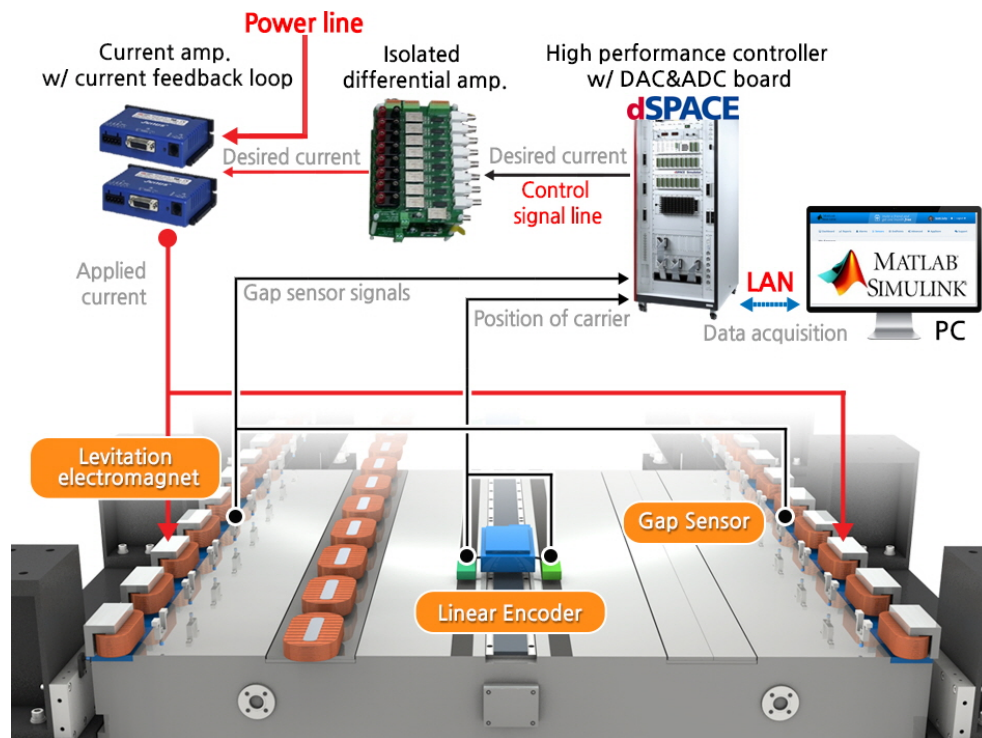


Figure 6.1. An experimental setup for a high precision magnetic levitation transport system.

6.2 Experimental Results

Based on the experimental setup, the levitation control performances of a high precision magnetic levitation transport system are experimentally verified under several scenarios as follows:

- S1)* The levitation control performance is verified at a standstill. The applied currents can be monitored to levitate the carrier, and the airgap measurements are acquired at the desired value.
- S2)* The levitation control performance is verified at the speed of 30 mm/s. The position of the carrier and the airgap measurement at low speed of movement are verified, respectively.
- S3)* The levitation control performance is verified at the speed of 300 mm/s. The position of the carrier and the airgap measurement at high speed of movement are verified, respectively.
- S4)* The levitation control performance is verified in the range of the deadzone. In practical application, the deadzone, where the levitation electromagnets are not able to be installed, exists between each module so that the motion of the carrier inevitably fluctuates as the carrier moves to the next module. Therefore, the levitation control performance should be guaranteed for the stability and robustness in this harsh condition.

6.2.1 Levitation Control Performance at a Standstill

For the verification of the levitation control performance at a standstill in *S1)*, the actual levitation control performance of the carrier at a standstill is shown in Figure 6.2. The carrier is smoothly levitated at the desired airgap once the applied current flows into the levitation electromagnets. The total current flows into the levitation electromagnet at a standstill as shown in Figure 6.3(a). About 3.1 A is required

to initially levitate the carrier, and it reduced to about 2.45 A at steady-state to maintain the carrier at desired airgap. For airgap measurement at a standstill in Figure 6.3(b), it is found that the desired airgap can be achieved with less than 50 μm peak to peak variation.

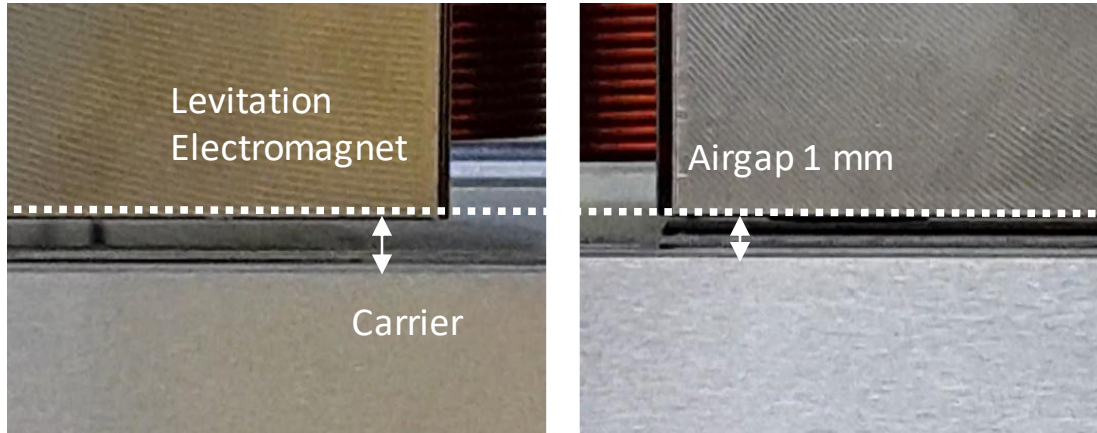


Figure 6.2. Levitation control performance at a standstill before levitating the carrier (right) and after levitating the carrier (left).

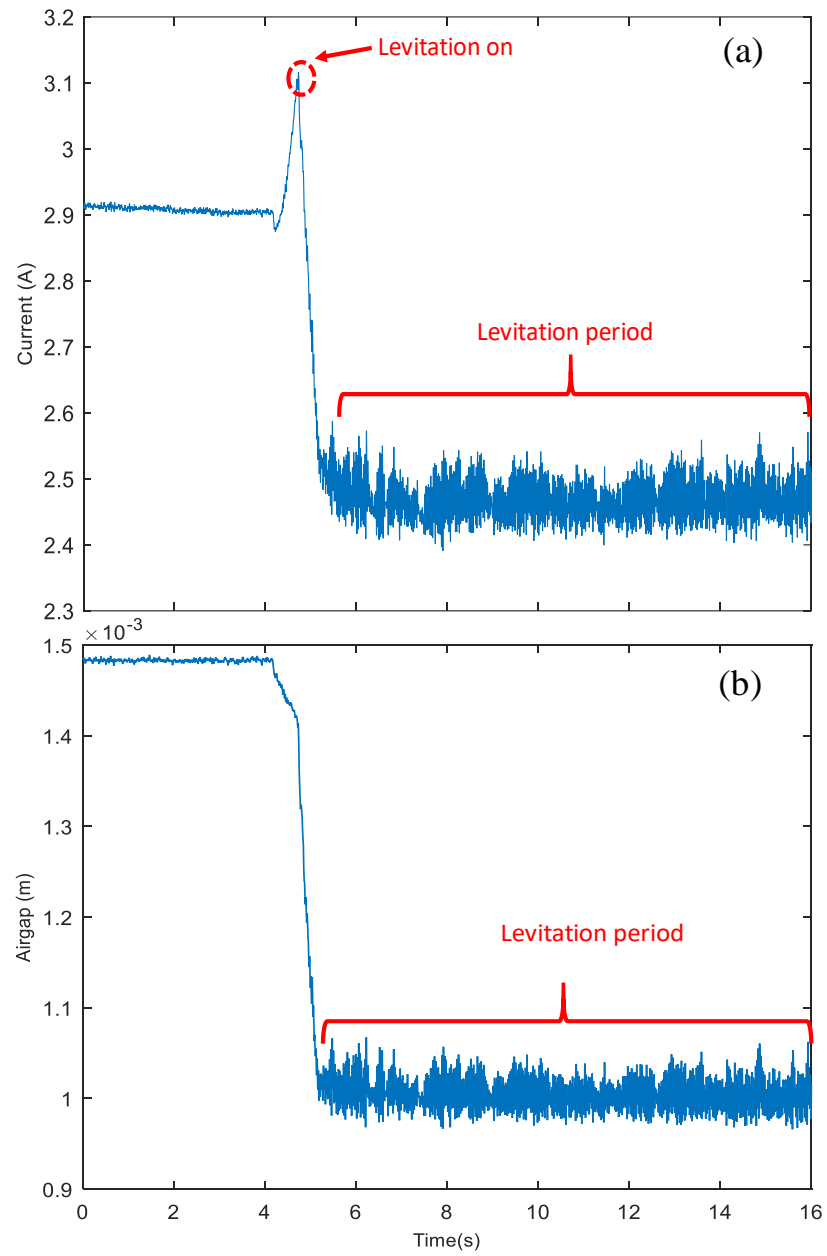


Figure 6.3. (a) Total current flows into the levitation electromagnet at a standstill and (b) Airgap measurement at a standstill.

6.2.2 Levitation Control Performance at Low Speed Level

In *S2*), there is a comparison between the levitation control performance using the levitation controller only and the levitation control performance using the proposed control strategies at low-speed level (30 mm/s).

Using the levitation controller only, the position of the carrier is shown in Figure 6.4(a). The carrier initially levitates and moves along the propulsion axis during the time period from 30 to 70 secs. The moved length is about 1.2 m so that the linear motor can generate the desired velocity and the position of the carrier is acquired by the encoder precisely. From a zoom-in view of airgap measurement as shown in Figure 6.4(b), each line represents the airgap measurement from each gap sensor. There are three switching zones at 35 to 55 secs where the carrier moves to the next influential zone. The fluctuations of the carrier's motion occur at these zones, and the peak to peak variation of airgap measurement at low speed of the movement is about 300 μm .

Using the proposed control strategies, the carrier moves in the range of 1.15 m from 10 to 50 secs as shown in Figure 6.5(a). As seen in Figure 6.5(b), there are three switching zones from 28 to 48 secs in the airgap measurements, and the peak to peak variation of airgap measurement is about 250 μm .

As a result, both cases maintain good stability and robustness of the levitation control performance, and the fluctuations of the proposed control strategies at the low-speed level are slightly attenuated compared to those of the levitation controller only because it has enough time to control the motion of the carrier for both cases.

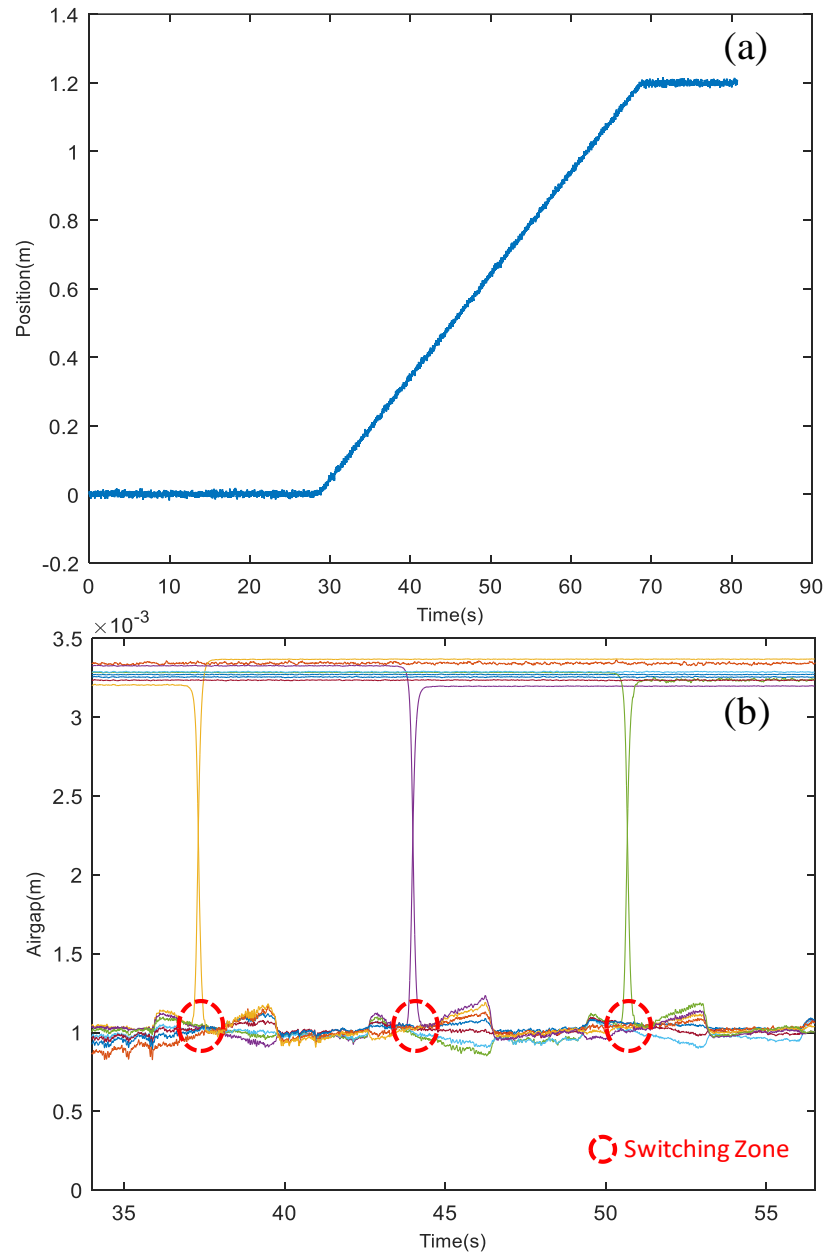


Figure 6.4. The levitation control performance using the levitation controller only at moving speed of 30 mm/s: (a) Position of the carrier in the propulsion axis and (b) Zoom-in plot of airgap measurement.

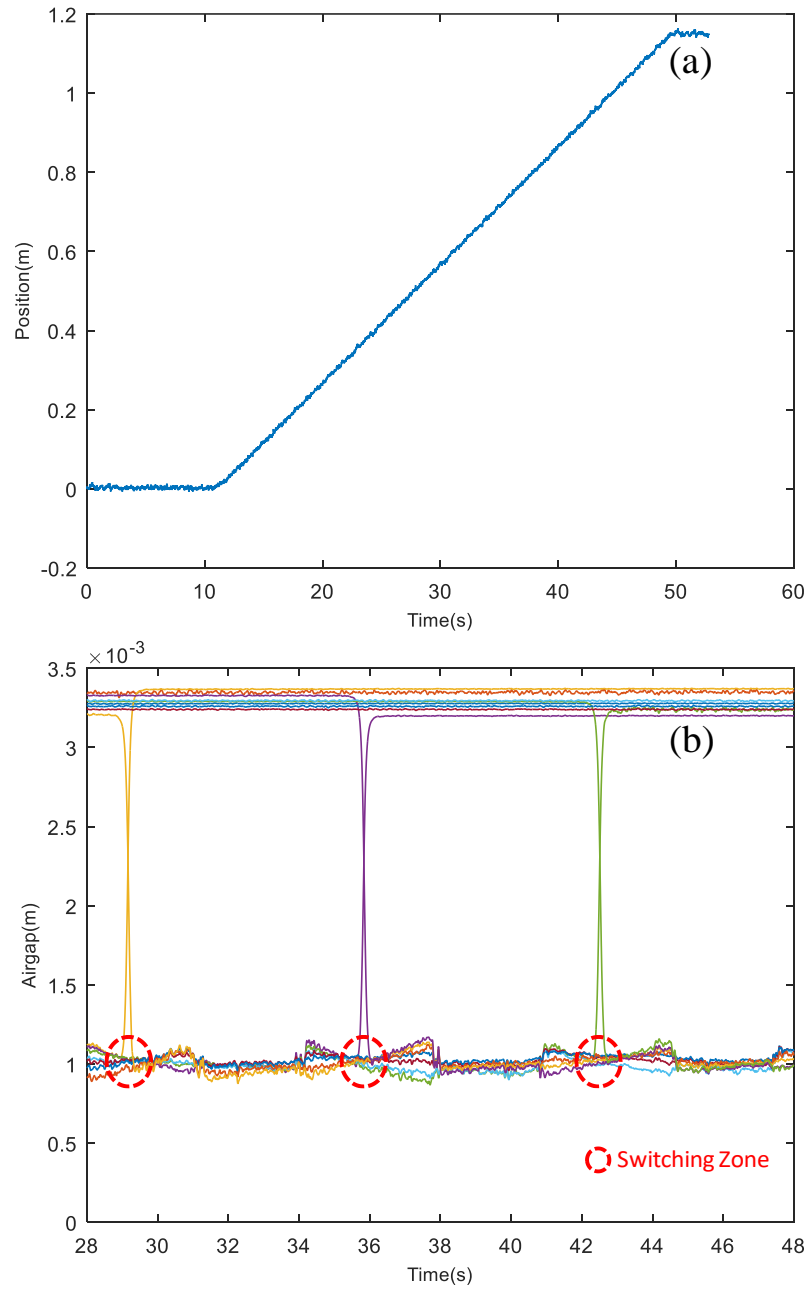


Figure 6.5. The levitation control performance using the proposed control strategies at moving speed of 30 mm/s: (a) Position of the carrier in the propulsion axis and (b) Zoom-in plot of airgap measurement.

6.2.3 Levitation Control Performance at High Speed Level

In $S3$), the levitation control performance of the carrier's motion using the levitation controller only and the position of the carrier are shown in Figure 6.6. As seen in Figure 6.6(a), the carrier is initially levitated, and it moves from 0 to 1.2 m from 15 to 20 secs with a rate of 300 mm/s. From the zoom-in view of the airgap measurement in Figure 6.6(b), there are three switching zones from 16.5 to 18.5 secs. During switch zones, the fluctuations of the carrier's motion are increased compared to those of 30 mm/s since there is a delayed response of utilizing the levitation controller. The peak to peak variation rises to about 700 μm .

For the levitation control performance of the carrier's motion using the proposed control strategies, the carrier moves from 0 to 1.2 m from 5 to 10 secs with 300 mm/s along the propulsion axis as shown in Figure 6.7(a). The airgap measurement includes three switching zones from 7.5 to 10.5 secs as shown in Figure 6.7(b); the fluctuations during the switching zones are obtained around 430 μm with the proposed control strategies. Compared to the fluctuations of the carrier's motion using the levitation controller only, it is attenuated to around 270 μm , and the levitation control performance of the carrier's motion becomes more robust and stable. The maximum peak to peak variation of the airgap measurements for the levitation control performance is summarized in Table 6.1.

Table 6.1. The maximum peak to peak variation of the airgap measurements.

-	The levitation controller only (μm)	The proposed control strategies (μm)
At a standstill	50 μm	50 μm
At 30 mm/s of speed	300 μm	250 μm
At 300 mm/s of speed	700 μm	430 μm

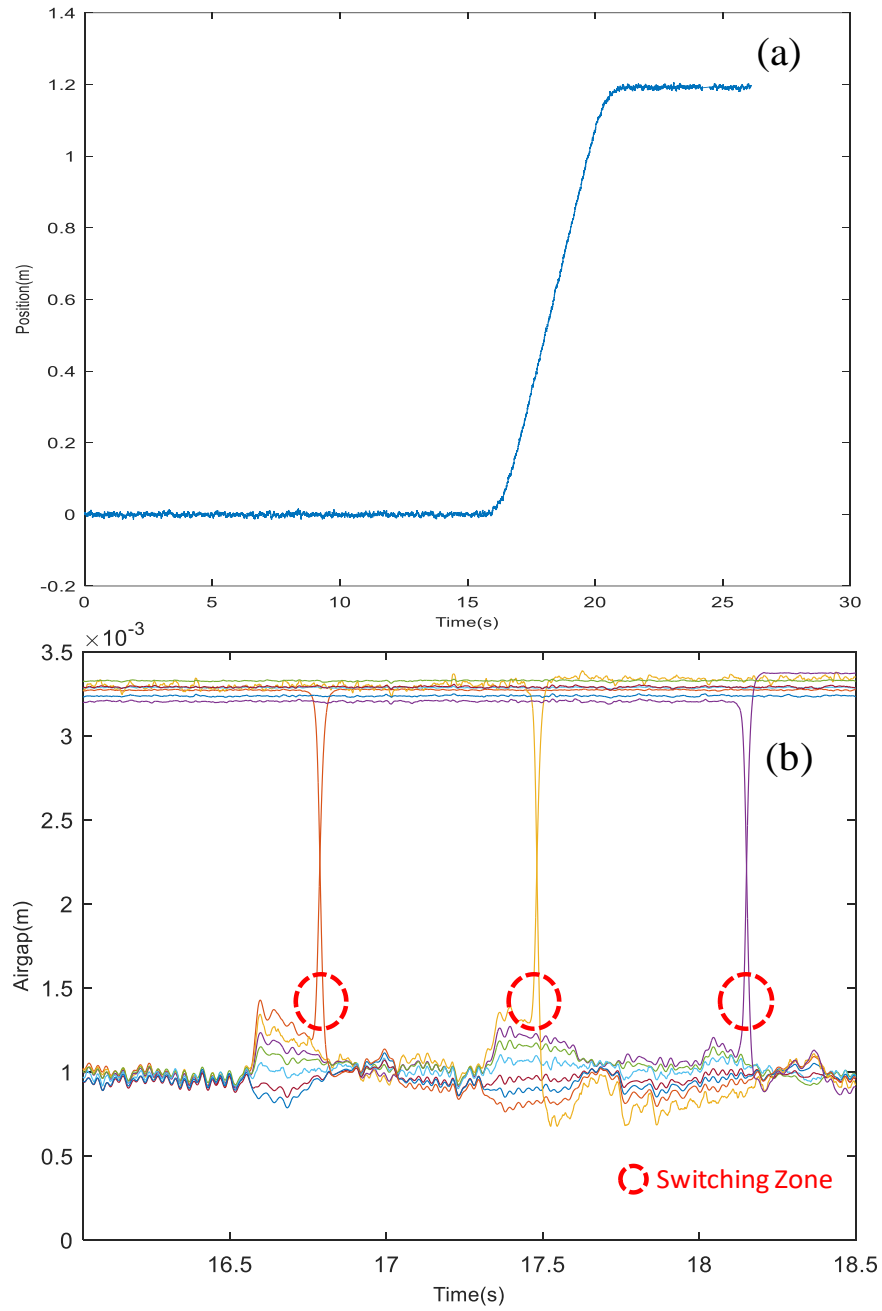


Figure 6.6. The levitation control performance using the levitation controller only at moving speed of 300 mm/s: (a) Position of the carrier in the propulsion axis and (b) Zoom-in plot of airgap measurement.

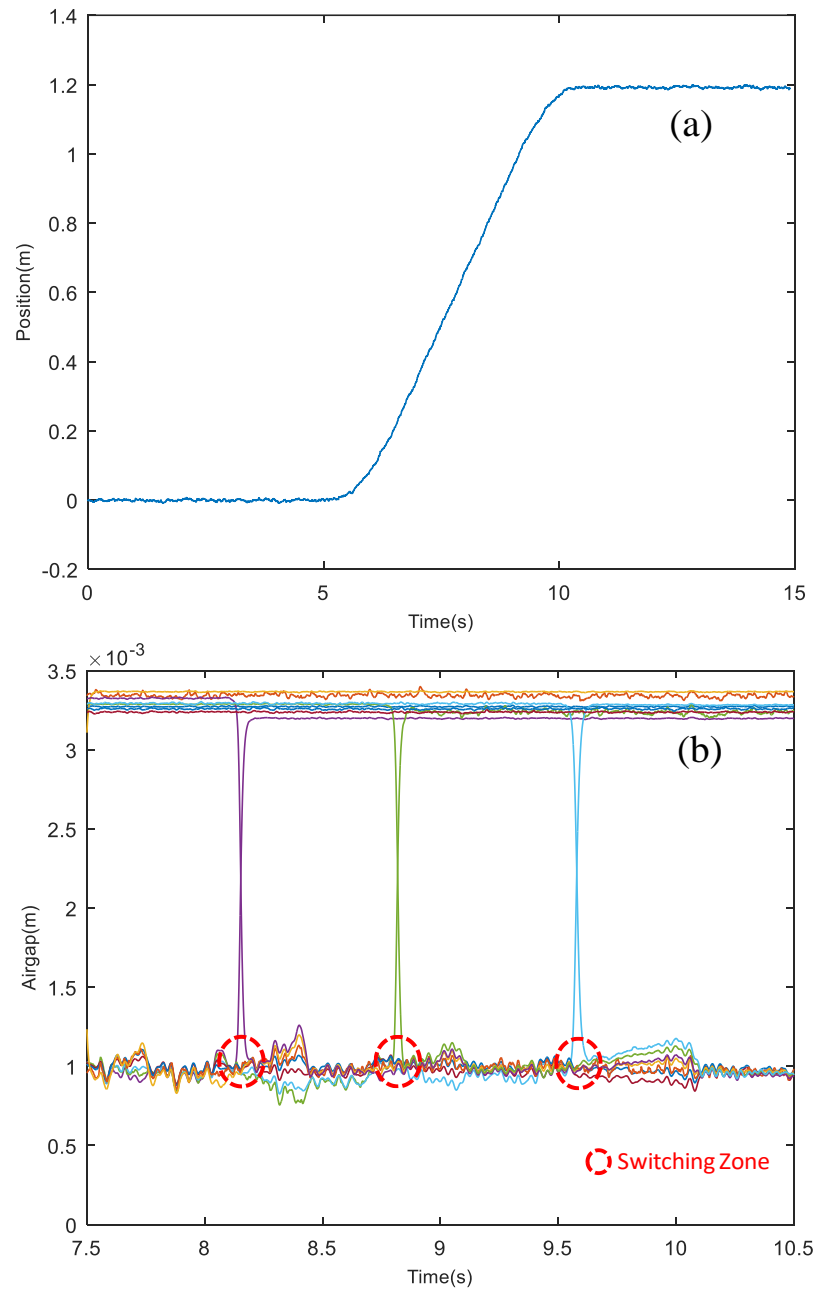


Figure 6.7. The levitation control performance using the proposed control strategies at moving speed of 300 mm/s: (a) Position of the carrier in the propulsion axis and (b) Zoom-in plot of airgap measurement.

6.2.4 Levitation Control Performance in the Deadzone

In practical application, the overall frames can be extended when the modules are connected in series, and each module is located inside a vacuum chamber as shown in Figure 6.8. The deadzone, where the levitation electromagnets are not able to be installed, exists between each module so that the motion of the carrier inevitably fluctuates as the carrier moves to the next module. The range of the deadzone is approximately $1/3$ of the length of the carrier. In this section, the levitation control performance of the carrier's motion in the deadzone is investigated. The stability and robustness using the proposed control strategies which include the levitation controller, roll and pitch controllers and, the section control algorithms are validated.

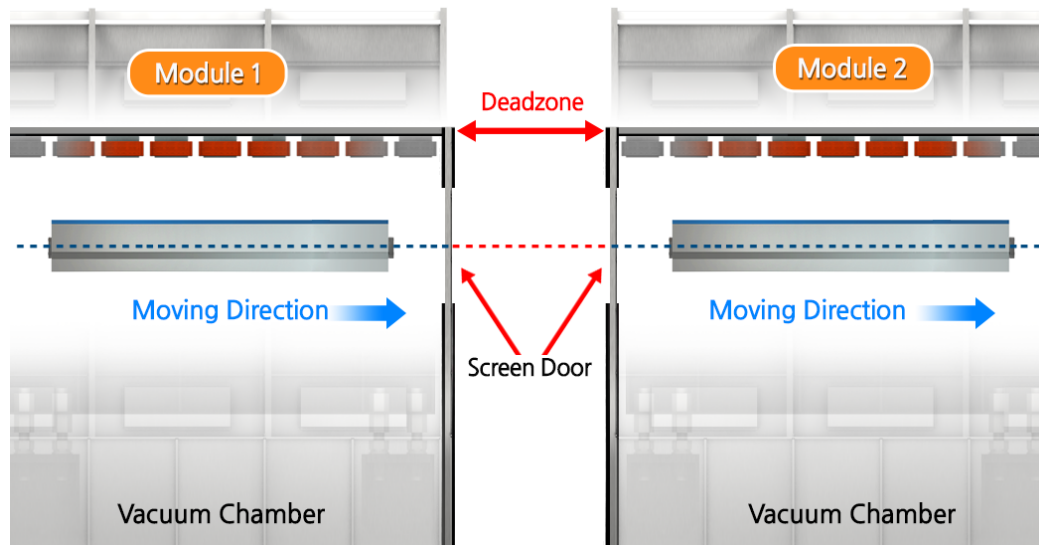


Figure 6.8. Schematic view of the deadzone. Each module can be extended in series and, there is a later gap where the levitation electromagnets are disabled to install owing to the screen door. The range of the deadzone is about $1/3$ of the length of the carrier.

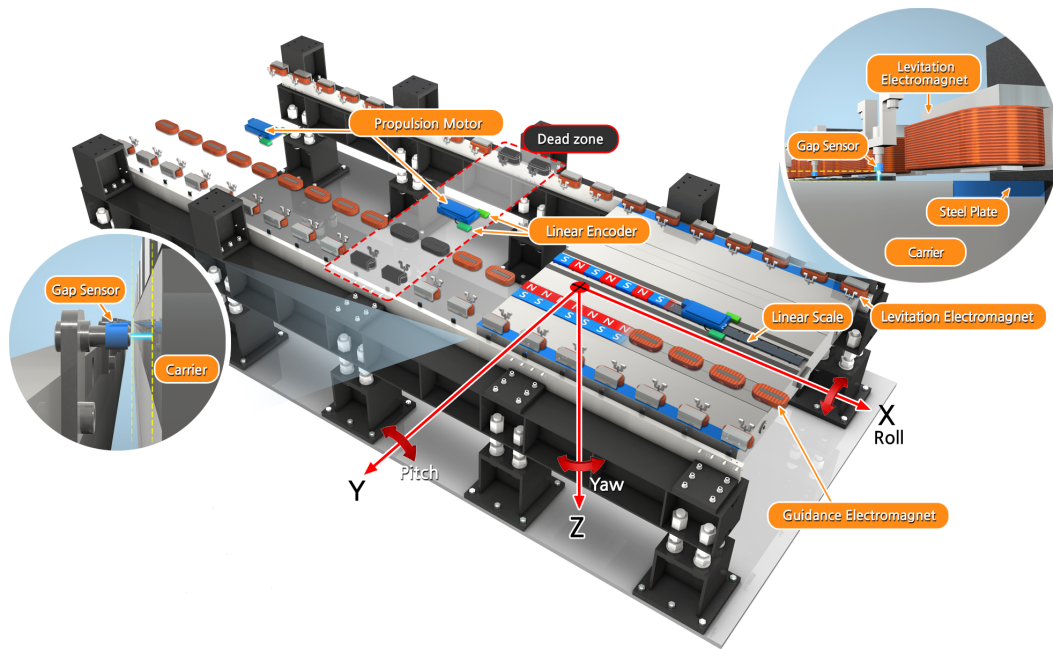


Figure 6.9. Experimental environment setup for the deadzone. To achieve the similar environment of the deadzone, the two pairs of side levitation electromagnets are disconnected, and the carrier passes into this zone supported by the 10-levitation electromagnets only.

The experimental environment of the deadzone set up is shown in Figure 6.9. The two pairs of side levitation electromagnets are disconnected from the current amplifier so that the carrier is levitated with 10-levitation electromagnets only in this zone. The range of the deadzone is about 600 mm along the propulsion axis, and the velocity of the carrier is generated at a low speed of movement to verify the levitation control performance. Having the control strategies for the levitation, roll and pitch motions and control section algorithms, the levitation control performance in the deadzone is validated from the airgap measurements. The change of the bias currents is verified to find how much current is required to maintain the carrier at levitating state without the mechanical contact (the carrier contacts with support frame).

The conventional PID form of the levitation controller is used in the deadzone. As the carrier moves with 30 mm/s of speed level into the deadzone as shown in Figure 6.10(a), the carrier is attached to the levitation electromagnets around 20 secs in Figure 6.10(b). Then, the motion of the carrier maintains the levitation control performance at the desired airgap. However, it cannot move into the deadzone owing to the mechanical contact between the carrier and levitation electromagnets.

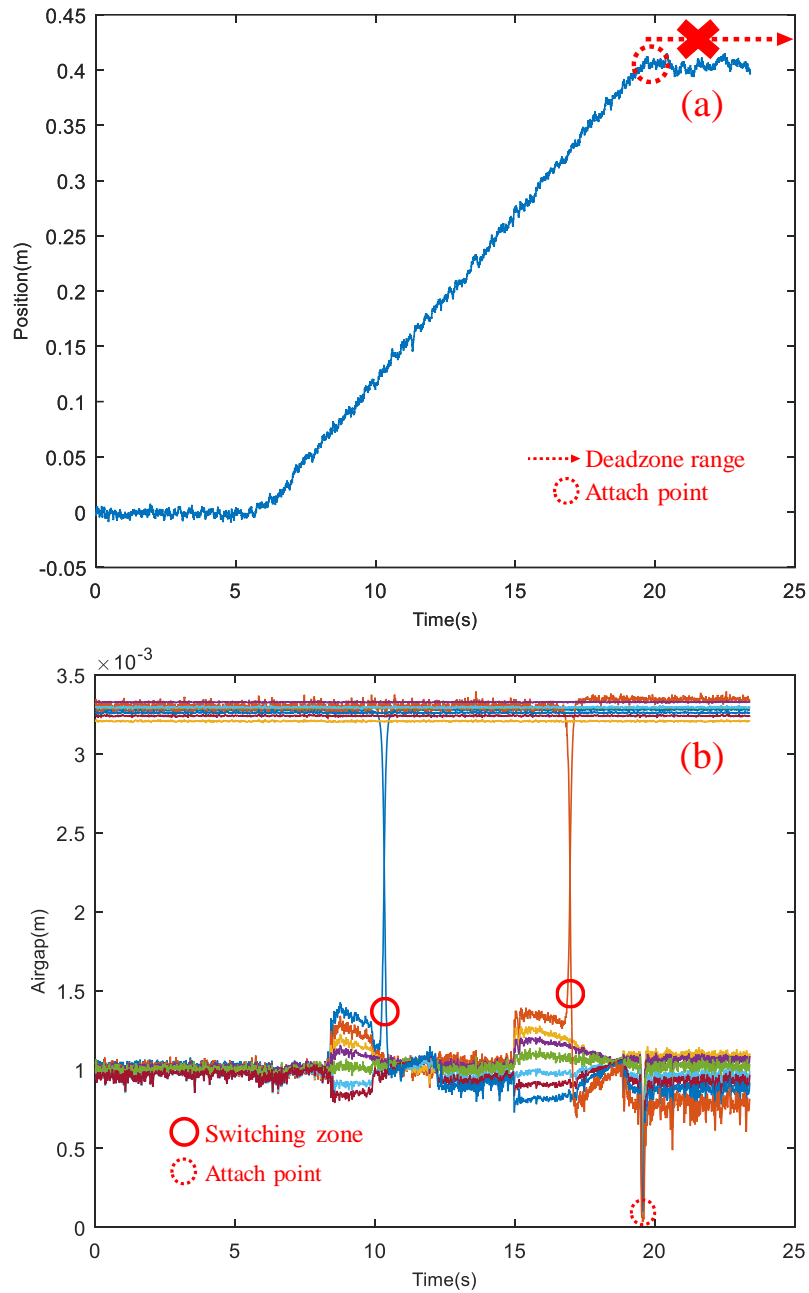


Figure 6.10. Experimental results using the PID controller only: (a) Position of the carrier at 30 mm/s of speed level. (b) The airgap measurement utilizing the conventional PID levitation controller only in the deadzone at 30 mm/s of speed level. The switching zones represent that the carrier moves to the next influential zone. The carrier moves to the first and following switching zones under the desired airgap. As it goes to the deadzone, the carrier fluctuates and attaches to the levitation electromagnets on attach point.

The proposed control strategies are now shown. The carrier operates at the same speed level as 30 mm/s as shown in Figure 6.11(a) and the airgap measurements in the deadzone are obtained to verify the levitation control performance as shown in Figure 6.11(b). The carrier moves into the deadzone after it passes after the second zone of gap sensors and the range of the period in the effective deadzone is from 20 secs to 45 secs. During this period, the peak to peak variations of the airgap measurement is about 850 μm . These measurements slowly converge to the desired airgap without the mechanical contact between the carrier and the levitation electromagnets.

As shown in Fig. 6.12(a) and (b), the roll motion of the carrier is slightly affected by the absence of the levitation electromagnets. However, the pitch angle of the carrier varies from about - 0.007 degree to 0.0038 degrees. Using the proposed control strategies, the fluctuations are slowly reduced and expected to converge to zero as the carrier completely passes into the deadzone.

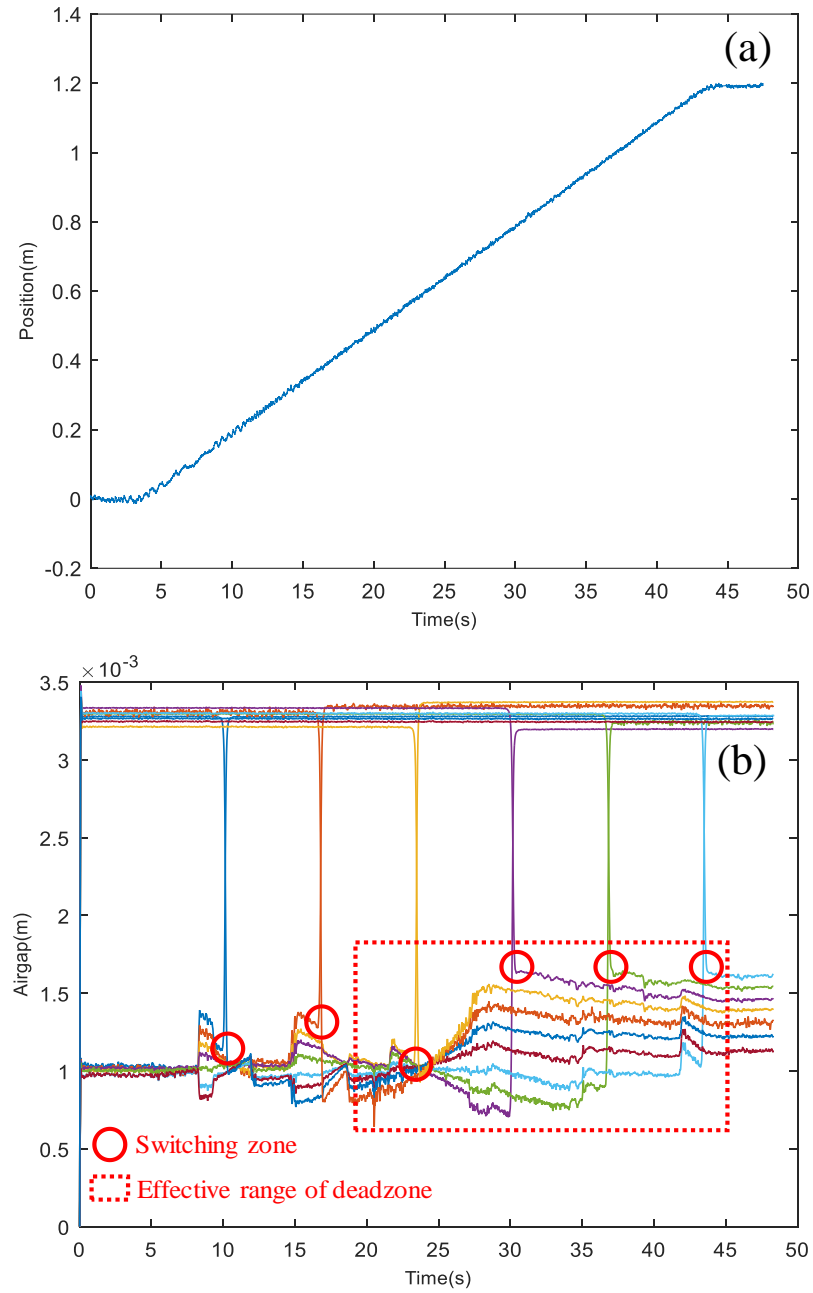


Figure 6.11. Experimental results using the proposed control strategies: (a) Position of the carrier at 30 mm/s of speed level. (b) Airgap measurement utilizing the proposed control strategies in the deadzone at 30 mm/s of speed level.

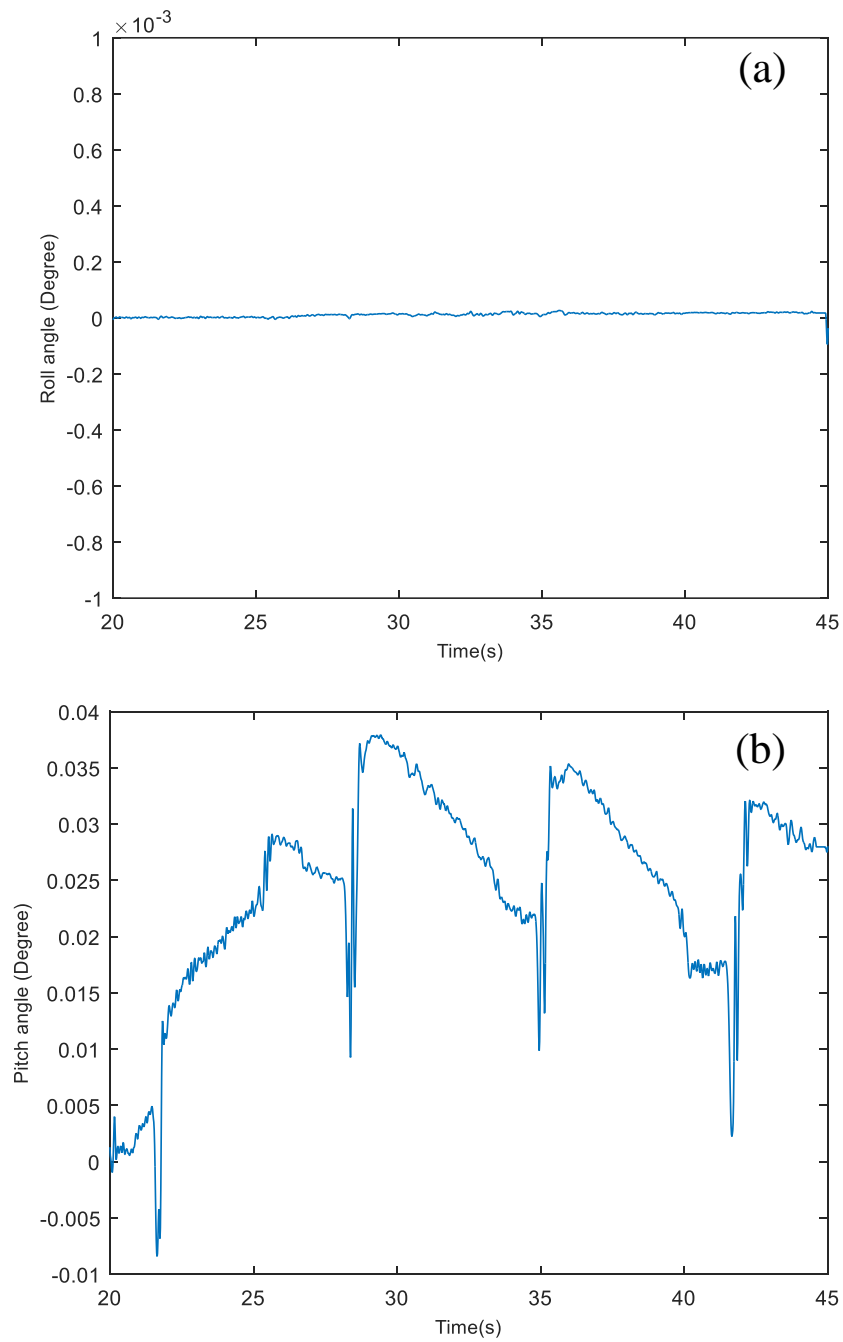


Figure 6.12. (a) Zoom in plot of the roll angle of the carrier in the deadzone at 30 mm/s of speed level. (b) Zoom in plot of the pitch angle of the carrier in the deadzone at 30 mm/s of speed level.

In consideration of the pitching moment about lateral-axis in the deadzone as shown in Figure 6.13, there are four variations which correspond to the pitch angle of the carrier. As the carrier rotates owing to the absence of the levitation electromagnets, the pitching moment has an opposite direction to minimize the pitch motion of the carrier. As the carrier enters into the deadzone, peak to peak variation of the pitching moment is about 277 Nm. This moment increases as the carrier moves into the deadzone and the peak to peak variation of the pitching moment at 42 secs is about 433 Nm. From an analysis of the pitching moment, it is clear that the pitch controller in the proposed control strategies plays a critical role in reducing the pitch motion of the carrier in the deadzone.

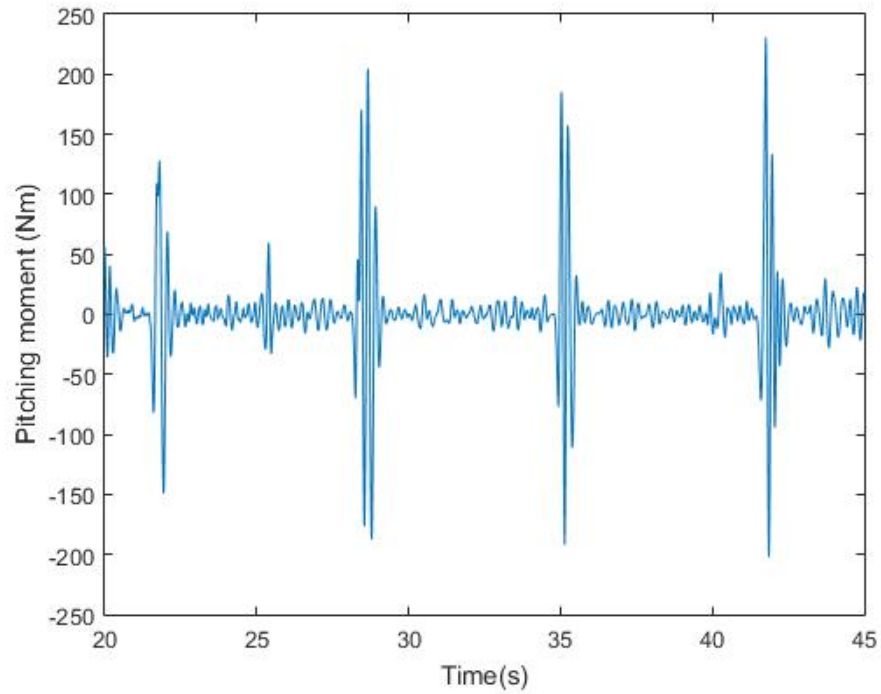


Figure 6.13. Zoom in view of the pitching moment in the deadzone.

Based on the section control algorithms, the bias currents that flow into the levitation electromagnets at the edge of the carrier are about 0.8 A and others are about 1.4 A before the carrier moves to the deadzone as shown in Figure 6.14. As carrier passes into the deadzone, above 2 A of bias currents are necessary to activate the levitation electromagnets to maintain good levitation control performance in the deadzone.

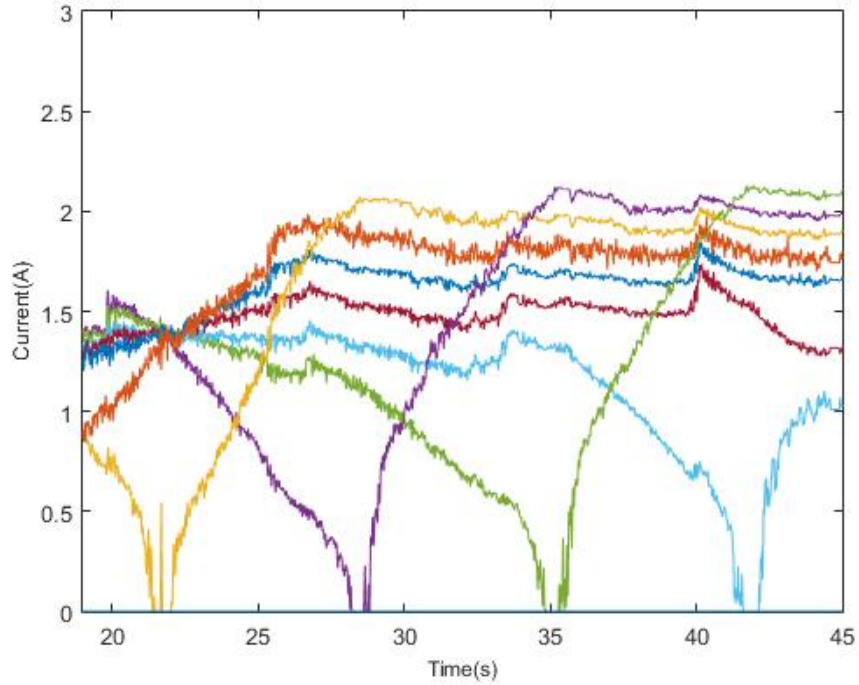


Figure 6.14. Zoom in plot of the bias currents in the deadzone. The bias currents initially maintain about 0.8 A and 1.4 A based on the section control algorithms and these are increased to about 2 A owing to the absence of the levitation electromagnets in the deadzone.

7. SUMMARY AND FUTURE DIRECTION

7.1 Summary and Conclusion

In this paper, a high precision magnetic levitation transport system for carrying OLED displays is proposed. To implement the levitation control of our system, several methodologies were developed as follows:

First, we developed the algorithm to estimate sensor installation error for gap sensors. Sensor installation error in the magnetic levitation transport system causes fluctuations of the carrier to occur which has an adverse effect on the transport of OLED displays. To estimate sensor installation error, we obtained fluctuation periods of raw measurement from the gap sensor at the highest speed of carrier (500 mm/s). Then, a single-sided amplitude spectrum of fluctuations in the frequency domain was obtained using a FFT analysis. The amplitudes with respect to the change in sensor offset were collected and a linear equation between amplitude and the sensor offsets was determined. An iterative method was used to estimate the parameters and to find the accurate sensor offset. After the process of verifying our methodology, we calibrated the sensor offset from measurement and showed successful performance using our algorithms.

Second, a multi-degree of freedom dynamic model was used to design the levitation, roll and pitch controller. The levitation controller, a cascade control strategy, consisted of the current controller (inner-loop) and the airgap controller (outer-loop). The current controller used PI control, which allowed the inductance effect from the levitation electromagnets to be eliminated. The bandwidth of the current controller was designed to be at least 10 times larger than that of the airgap controller so that a fast response of the inner loop in the levitation control system could be obtained. The airgap controller was designed as a PID controller to achieve the desired airgap

between the carrier and the levitation electromagnets. Using frequency response analysis and the Nyquist criterion, the level of relative stability is satisfied. To improve the stability and robustness of the levitation control performance, dynamic models and controllers design for the roll and pitch motions are developed. From a state space representation of the roll and pitch motion of the carrier, controllability and observability tests are verified as controllable and observable. For the roll and pitch controller, a combined optimal state feedback controller (LQR)-observer compensator was utilized, and it achieved a good levitation control performance in the presence of a large load disturbance and sensor installation error.

To minimize the mechanical resonance of the carrier and noise from the gap sensors, a second order notch filter and, a first order low pass filter were designed using an impact test and data signal processing, respectively. A section control algorithm was developed to minimize the sudden change of the levitation forces as the carrier moves along the propulsion axis. Based on the specifications such as sum of the levitation forces should be equal to the weight of the carrier and sum of the moment along the propulsion axis is equal to zero, a mathematical strategy of the section control algorithm was established, and it was verified with simulation.

Based on the theoretical analysis and simulation, the levitation control performance of a high precision magnetic levitation transport system was experimentally validated. Based on the experimental setup using DS1104 R&D board of the dSPACE and Junus units, fast response of the applied current loop was generated, and the real-time output of systems from the levitation control structure was verified.

From the experimental tests, good levitation control performances of the carrier were verified using the proposed control strategies. The peak to peak variation of the carrier's motion at a standstill was around $50\text{ }\mu\text{m}$. Compared to the conventional PID form of the levitation controller only, the peak to peak variations of the carrier's motion were attenuated to around $50\text{ }\mu\text{m}$ at a low speed of movement (30 mm/s) and $270\text{ }\mu\text{m}$ at a high speed of movement (300 mm/s), respectively. Moreover, the conventional PID form of the controller did not guarantee the robustness and stability

of the system in the deadzone where two pairs of side levitation electromagnets were disabled; the carrier was attached to the levitation electromagnets as it moved along propulsion axis so that there was a mechanical contact. Using the proposed control strategies, the carrier could pass into the deadzone without mechanical contact.

7.2 Future Work

Based on our current methodologies, it can extend the work towards several promising and challenging research topics. To minimize uncertain factors of the system such as modeling error and external disturbance from the linear motor, advanced control strategies could be utilized such as Linear Matrix Inequalities (LMIs) based optimal state-feedback controller-observer compensator or adaptive controller. Then, the levitation control performance of the carrier using these control strategies will compare to those using the currently proposed control strategies.

Another challenging issue is that the levitation control performance of the carrier maintains a desired airgap of 1 mm. However, the optimal airgap with respect to the applied current is not established. Therefore, it is future work to find the optimal airgap with respect to the minimal applied current, which is a cost-effective methodology to optimize energy efficiency in the operation of the magnetic levitation transport system.

Moreover, the airgap measurements are slowly converged to the desired airgap even if there is no mechanical contact between the carrier and the levitation electromagnets in the deadzone. Therefore, it is the future work to achieve a rapid convergence of the desired airgap as the carrier passes the deadzone and to demonstrate the implementation of the levitation control performance of the carrier utilizing the novel control strategies.

REFERENCES

REFERENCES

- [1] Park, J. S., Kim, J. S., & Lee, J. K. (2001). Robust control of maglev vehicles with multimagnets using separate control techniques. *KSME international journal*, 15(9), 1240-1247.
- [2] Seo, S. I., Lee, M. K., Kim, S. J., & Kim, N. (2011). Robust optimum design of a bearingless rotation motor using the Kriging model. *International Journal of Precision Engineering and Manufacturing*, 12(6), 1043-1050.
- [3] Park, K., Choi, K. B., Kim, S. H., & Kwak, Y. K. (1995). Design of magnetically suspended frictionless manipulator. *Journal of Mechanical Science and Technology*, 9(3), 323-335.
- [4] Han, H.S., Kim, D.S. (2016). Magnetic levitation: maglev technology and applications, *Springer*, New York, USA.
- [5] Ha, C. W., Kim, C. H., & Lim, J. (2017). Development of high accuracy of magnetic levitation transport system for OLED evaporation process. *In Advanced Intelligent Mechatronics (AIM), 2017 IEEE International Conference on* (pp. 1334-1339). IEEE.
- [6] Earnshaw, S. (1842). On the nature of the molecular forces which regulate the constitution of the luminiferous ether. *Trans. Camb. Phil. Soc.*, 7, 97-112.
- [7] Kemper, H. (1934). *German Patent* No.643316.
- [8] Yamamura, S. (1976). Magnetic levitation technology of tracked vehicles present status and prospects. *IEEE Transactions on Magnetism*, 12(6), 874-878.
- [9] Sinha, P. (1984). Design of a magnetically levitated vehicle. *IEEE Transactions on Magnetism*, 20(5), 1672-1674.
- [10] Eastham, A. R., & Hayes, W. F. (1988). Maglev systems development status. *IEEE Aerospace and Electronic Systems Magazine*, 3(1), 21-30.
- [11] Lee, H. W., Kim, K. C., & Lee, J. (2006). Review of maglev train technologies. *IEEE transactions on magnetism*, 42(7), 1917-1925.
- [12] Dai, H. (2005). Dynamic behavior of maglev vehicle/guideway system with control. *PhD, Case Western Reserve University*.
- [13] Wegerer, K., Ellmann, S., Becker, P., & Hahn, W. Requirements, design and characteristics of the Maglev vehicle transrapid 08. *In Maglev* (Vol. 98, pp. 202-208).
- [14] Xiangming, W. (2004). Achievements of Shanghai maglev demonstration operation line and the maglev development strategy. *In 18th International Conference on Magnetically Levitated Systems and Linear Driver*, ShangHai, China.

- [15] Tum, M., Huhn, G., & Harbeke, C. (2006). Design and Development of the Transrapid TR09. *In The 19th International Conference on Magnetically Levitated Systems and Linear Drives*, Dresden, Germany (pp. 13-15).
- [16] Wolters, C. (2008). Latest generation maglev vehicle TR09. *In The 20th International Conference on Magnetically Levitated Systems and Linear Drives* (No. 123).
- [17] Ono, M., Koga, S., & Ohtsuki, H. (2002). Japan's superconducting maglev train. *IEEE Instrumentation & Measurement Magazine*, 5(1), 9-15.
- [18] Kim, M., Jeong, J. H., Lim, J., Kim, C. H., & Won, M. C. (2017). Design and control of levitation and guidance systems for a semi-high-speed maglev train. *J. Electr. Eng. Technol.*, 12(1), 117-125.
- [19] Shin, B. C., Kim, W. J., Park, D. Y., Baik, S. H., Beak, J. G., & Kang, H. S. (2011). Recent Progress of Urban Maglev Program in Korea. *In the 21st International Conference on Magnetically Levitated Systems and Linear Drives*.
- [20] Park, D. Y., Shin, B. C., & Han, H. (2009). Korea's urban maglev program. *Proceedings of the IEEE*, 97(11), 1886-1891.
- [21] Lim, J., Kim, C. H., Han, J. B., & Han, H. S. (2015). Design of an electromagnet with low detent force and its control for a maglev super-speed vehicle. *J. Electr. Eng. Technol.*, 10(4), 1668-1674.
- [22] Kim, C. H., Lee, J. M., Han, H. S., & Lee, C. W. (2011). Development of a maglev LCD glass conveyor. *Transactions of the KSME A*, 47(4), 581-587.
- [23] Kim, K. J., Han, H. S., Kim, C. H., & Lee, C. W. (2011). Dynamic Analysis of the Maglev Conveyor for LCD Glass Cassette. *The 21st International Conference on Magnetically Levitated Systems and Linear Drives*
- [24] Li, S. E., Park, J. W., Lim, J. W., & Ahn, C. (2015). Design and control of a passive magnetic levitation carrier system. *International Journal of Precision Engineering and Manufacturing*, 16(4), 693-700.
- [25] Park, J. W., Kim, C. H., Park, D. Y., & Ahn, C. (2014). Controller design with high fidelity model for a passive maglev tray system. *International journal of precision engineering and manufacturing*, 15(8), 1521-1528.
- [26] Lee, Y., Kim, C. H., Ha, C. W., Park, D. Y., Yang, S. J., & Lim, J. (2016). Passive Maglev Carrier Control with Consideration of Pitch Motion. *Transactions of the Korean Society of Mechanical Engineers A*, 40(2), 213-220.
- [27] Sinha, P. K. (1987). Electromagnetic suspension dynamics & control.
- [28] Bentley JP. Principles of measurement systems. Pearson Education India;1988.
- [29] Kim, J., King, G. B., & Kim, C. H. (2018). Development of Algorithm to Estimate Sensor Offset in Maglev Tray System. *International Journal of Precision Engineering and Manufacturing*, 19(3), 349-358.
- [30] Van Loan, C. (1992). Computational frameworks for the fast Fourier transform (Vol. 10). Siam.

- [31] Cooley, J. W., & Tukey, J. W. (1965). An algorithm for the machine calculation of complex Fourier series. *Mathematics of computation*, 19(90), 297-301.
- [32] Cochran, W. T., Cooley, J. W., Favin, D. L., Helms, H. D., Kaenel, R. A., Lang, W. W., ... & Welch, P. D. (1967). What is the fast Fourier transform?. *Proceedings of the IEEE*, 55(10), 1664-1674.
- [33] Cerna, M., & Harvey, A. F. (2000). The fundamentals of FFT-based signal analysis and measurement. *National Instruments*, Junho, 54.
- [34] Smith, S. W. (1997). The scientist and engineer's guide to digital signal processing.
- [35] Rutishauser, H. (1966). The Jacobi method for real symmetric matrices. *Numerische Mathematik*, 9(1), 1-10.
- [36] Kim, J., King, G. B., Kim, C. H., & Ha, C. W. (2018). Modeling and designing levitation, roll and pitch controller for high accuracy maglev tray system. *Mechatronics*, 53, 181-191.
- [37] Zak, S. H. (2003). Systems and control (Vol. 198). *New York: Oxford University Press*.
- [38] Kim, J., King, G. B., Ha, C. W., & Kim, C. H. An Experimental Implementation of Levitation Control for a High Accuracy Maglev Transport System. Under review.
- [39] Lee, K. C. (2014). Section control of the electromagnetic levitation conveyor (EMLC) for a FPD glass carrying robot. *PhD, Pusan National University*.
- [40] Kim, J., King, G. B., Kim, C. H., & Ha, C. W. Deadzone Compensation of A High Accuracy Maglev Transportation for Carrying OLED Displays. Under review.

APPENDICES

A. LINEARIZED EQUATION OF THE LEVITATION FORCE BY EACH LEVITATION ELECTROMAGNET

The levitation force and the voltage equation exerted by each electromagnet which are described by [27]

$$f_k(t) = f(i_k(t), c_k(t)) = \frac{\mu_0 N^2 A}{4} \left(\frac{i_k(t)}{c_k(t)} \right)^2, k = 1, 2, 3 \dots 2n \quad (\text{A.1})$$

$$v_k(t) = R \cdot i_k(t) + \frac{d(L_k(t) \cdot i_k(t))}{dt}, k = 1, 2, 3 \dots 2n \quad (\text{A.2})$$

The 14-activate levitation electromagnets are equally distributed to lift the carrier so that each activate-levitation electromagnet loads 1/14 of the carrier's total weight. If (i_0, c_0) denotes the equilibrium point then, The vertical dynamics of each levitation force is derived without the load disturbance as

$$m_e \ddot{c}_k(t) = -f_k(t) + m_e g \quad (\text{A.3})$$

where, m_e is 1/14 of the carrier's total mass (m), $c_k(t) = c_0 + \Delta c_k(t)$ and $i_k(t) = i_0 + \Delta i_k(t)$.

Having a small perturbation linear equation, the vertical dynamics of each levitation force can be re-written as

$$\begin{aligned}
m_e \Delta \ddot{c}_k(t) &= -\frac{\mu_0 N^2 A}{4} \left(\frac{i_0 + \Delta i_k(t)}{c_0 + \Delta c_k(t)} \right)^2 + m_e g \\
&\simeq -\frac{\mu_0 N^2 A}{4} \left(\frac{i_0}{c_0} \right)^2 \left(\frac{1 + \frac{\Delta i_k(t)}{i_0}}{1 + \frac{\Delta c_k(t)}{c_0}} \right)^2 + m_e g \\
&= -\frac{\mu_0 N^2 A}{4} \left(\frac{i_0}{c_0} \right)^2 \left(\frac{(1 + \frac{\Delta i_k(t)}{i_0})(1 - \frac{\Delta c_k(t)}{c_0})}{(1 + \frac{\Delta c_k(t)}{c_0})(1 - \frac{\Delta c_k(t)}{c_0})} \right)^2 + m_e g \\
&= -\frac{\mu_0 N^2 A}{4} \left(\frac{i_0}{c_0} \right)^2 \left(\frac{1 - \frac{\Delta c_k(t)}{c_0} + \frac{\Delta i_k(t)}{i_0} - \frac{\Delta c_k(t) \Delta i_k(t)}{c_0 i_0}}{1 - (\frac{\Delta c_k(t)}{c_0})^2} \right)^2 + m_e g
\end{aligned} \tag{A.4}$$

The second-order effects of above equation are negligible. Therefore, the small perturbation linear equation of each levitation force is

$$\begin{aligned}
m_e \Delta \ddot{c}_k(t) &= -\frac{\mu_0 N^2 A}{4} \left(\frac{i_0}{c_0} \right)^2 \left(1 - \frac{\Delta c_k(t)}{c_0} + \frac{\Delta i_k(t)}{i_0} \right)^2 + m_e g \\
&\simeq -\frac{\mu_0 N^2 A}{4} \left(\frac{i_0}{c_0} \right)^2 + \frac{\mu_0 N^2 A i_0^2}{2 c_0^3} \Delta c_k(t) - \frac{\mu_0 N^2 A i_0^2}{2 c_0^2} \Delta i_k(t) + m_e g
\end{aligned} \tag{A.5}$$

The equilibrium point and the vertical dynamics are used to find $m_e g$ as

$$\begin{aligned}
m_e \ddot{c}_k(t) &= -f(i_0, c_0)_k + m_e g = 0 \\
f(i_0, c_0)_k &= m_e g = \frac{\mu_0 N^2 A}{4} \left(\frac{i_0}{c_0} \right)^2
\end{aligned} \tag{A.6}$$

From (A.6) to (A.5),

$$\begin{aligned}
m_e \Delta \ddot{c}_k(t) &= \Delta f_k(t) = \frac{\mu_0 N^2 A i_0^2}{2 c_0^3} \Delta c_k(t) - \frac{\mu_0 N^2 A i_0^2}{2 c_0^2} \Delta i_k(t) \\
&= K_c \Delta c_k(t) - K_i \Delta i_k(t)
\end{aligned} \tag{A.7}$$

where, $K_i = \frac{\mu_0 N^2 A i_0}{2c_0^2}$, and $K_c = \frac{\mu_0 N^2 A i_0^2}{2c_0^3}$.

The voltage equation can be linearized using small perturbation with the equilibrium point and it is derived as

$$\Delta \dot{i}_k(t) = \frac{K_c}{K_i} \Delta \dot{c}_k(t) - \frac{R}{L_0} \Delta i_k(t) + \frac{1}{L_0} \Delta v_k(t) \quad (\text{A.8})$$

B. DERIVATION OF THE PITCHING MOTION OF THE CARRIER WITH AIRGAP APPROXIMATION

According to the proposed mathematical approximation between the pitch angle and airgaps with the zones of activate-levitation electromagnets as shown in equation 4.6, it is noticed that $\Delta c_{k,r,l}(t)$ and $\Delta x_k(t)$ can be approximated based on relatively small value of the pitch angle as

$$\Delta c_{k,r,l}(t) = \frac{kl}{n} \sin(\theta(t)) \simeq \frac{kl}{n} \theta(t) \quad (\text{B.1})$$

$$\Delta x_k(t) = \frac{kl}{n} \cos(\theta(t)) \simeq \frac{kl}{n}$$

where, n is a number of activate-levitation electromagnets at each side along the propulsion axis.

Using (B.1), the linearized dynamic equation of the pitch motion (Equation 4.6) is derived as

$$\begin{aligned} I_{yy} \ddot{\theta}(t) &= K_c \sum_{k=1}^n \left(\frac{k}{n}\right)^2 l^2 \theta(t) - K_i \sum_{k=1}^n \left(\frac{kl}{n}\right) \Delta i_{k,r,l}(t) \\ &= K_c l^2 \theta(t) \sum_{k=1}^n \left(\frac{k}{n}\right)^2 - K_i l \sum_{k=1}^n \left(\frac{k}{n}\right) \Delta i_{k,r,l}(t) \\ &= K_c l^2 \theta(t) \left(\frac{1^2 + 2^2 + 3^2 \dots n^2}{n^2}\right) - \frac{K_i l}{n} \sum_{k=1}^n k \Delta i_{k,r,l}(t) \\ &= K_c l^2 \theta(t) \left(\frac{1/6 n(n+1)(2n+1)}{n^2}\right) - \frac{K_i l}{n} \sum_{k=1}^n k \Delta i_{k,r,l}(t) \end{aligned} \quad (\text{B.2})$$

Having $n = 7$ in our case, the linearized dynamic equation of the pitch motion is re-written as

$$I_{yy}\ddot{\theta}(t) = \frac{20}{7}K_cl^2\theta(t) - \frac{1}{7}K_il\sum_{k=1}^7k\Delta i_{k,r,l}(t) \quad (\text{B.3})$$

VITA

VITA

Jaeyoung Kim was born in Daejeon, Republic of Korea, in 1989. He received his B.S and M.S. in the school of Mechanical Engineering at Purdue University, West Lafayette, IN, USA, in 2014 and 2015, respectively. He is a student member of IEEE and a member of the IEEE Robotics and Automation Society. He has researched about motion controls and sensor algorithms on magnetic levitation transport system at Purdue University. He is currently pursuing the Ph.D. degree in the school of Mechanical Engineering at Purdue University under Professor Galen B. King.

LIST OF PUBLICATIONS

1. **Kim, J.**, King, G. B., Kim, C. H., & Ha, C. W. Deadzone Compensation of A High Accuracy Maglev Transportation for Carrying OLED Displays. Under review.
2. **Kim, J.**, King, G. B., Ha, C. W., & Kim, C. H. An Experimental Implementation of Levitation Control for a High Accuracy Maglev Transport System. Under review.
3. **Kim, J.**, King, G. B., Kim, C. H., & Ha, C. W. (2018). Modeling and designing levitation, roll and pitch controller for high accuracy maglev tray system. *Mechatronics*, 53, 181-191.
4. **Kim, J.**, King, G. B., & Kim, C. H. (2018). Development of Algorithm to Estimate Sensor Offset in Maglev Tray System. *International Journal of Precision Engineering and Manufacturing*, 19(3), 349-358.
5. **Kim, J.**, Cui, Y., & Ariyur, K. B. (2017). Using topography to aid smart phones geolocation. *Wireless Networks*, 1-14.
6. **Kim, J.**, Ariyur, K., Cui, Y., Branch, B. D., & Umo, J. E. (2014). Autonomous Indoor Localization for Fire Safety and Resource Location via Field Mapping Techniques. *Libraries Faculty and Staff Presentations*. Paper 69.
7. Umo, J. E., Cui, Y., Ariyur, K., Branch, B. D., & **Kim, J.** (2014). Autonomous Indoor Localization for Fire Safety and Resource Location via Field Mapping Techniques (Android Version). *Libraries Faculty and Staff Presentations*. Paper 76.